DEFORMATION ANALYSIS AT THE NORTHEASTERN PART OF SEMERA TOWN, CENTERAL AFAR, USING InSAR AND GPS

BY:

TESFAYE TEMTIME TESSEMA

A thesis submitted to the School of Graduate Studies of the Addis Ababa University in partial fulfillment of the requirements for the degree of Masters of Science in Civil Engineering under Geodesy

Addis Ababa, Ethiopia

July, 2013

Addis Ababa University

Institute of Technology

Department of Civil and Environmental Engineering

The undersigned here by certify that they have read and recommend to the school of technology for acceptance a thesis entitled "Deformation Analysis at Northeastern part of Semera Town, Central Afar Using InSAR and GPS" by Tesfaye Temtime Tessema in partial fulfillment of the requirements for the degree of Master of Science.

Date: July, 2013

Advisor:

1. ______________________________ ________________ ______________

Signature Date

2. ______________________________ ________________ ______________

Signature Date

Examiner(s):

1. ______________________________ ________________ ______________

2. ______________________________ ________________ ______________

3. ______________________________ ________________ ______________

Signature Date

Acknowledgment

My Master of Science in Geodesy is sponsored by EduLink of EU under University of Edinburgh,UK. I thank the principal investigator of the project Dr. Roger Hipkin and the coordinators. I thank School of Civil and Environmental Engineering, AAiT and Institute of Geophysics Space Science and Astronomy (IGSSA) of AAU. I thank also my employer Geological Survey of Ethiopia (GSE) for the support to attend this program.

Above all, I would like to thank God help me to reach at this stage.

It has been a privilege to begin my research career with Dr. Elias Lewi as my supervisor. I would like to thank him for sharing his considerable expertise and experience; and providing me with such good advice and support over the years. I would also like to thank Dr. Juliet Biggs as my supervisor in InSAR part of my thesis work.

I would like to thank Amy Parker, a Phd candidate at University of Bristol, who helped me in InSAR data processing and kind support in my stay in Bristol.

I would like to thank my wife Yewbishet Tsegaye Temtime for her encouragement and great support.

Last but not list, I would like to thank IGSSA research and administration staffs and my entire classmate who made my stay at the AAU pleasant and worthwhile.

Abstract

This study is conducted to analyze the deformation pattern at a locality in the central part of Afar, northeast of Semera town, within the triple junction that is formed by the Arabian, Nubian and Somalian diverging plates. The study area is bordered by Manda Harraro rift in the northwest and Tendaho rift in the south. The region is one of the tectonically active areas in the world, where the episode of plate movement resulted in seafloor spreading that causes the earth's surface to deform in the form of surface cracking, sliding and faulting. Presently this dynamic process of earth's deformation in space and time can be accurately detected by satellite space geodetic observations.

This study used Global Positioning System (GPS) and Interferometric Synthetic Aperture Radar (InSAR) to study earth surface deformation. InSAR data from Envisat, image mode, with track 028 ascending and track 278 descending is used to detect surface deformation over the study area. To constrain the InSAR observations, continuously recorded GPS data obtained from DASM (2007-2012) and DASA (2008-2009) are used to investigate possible surface deformation changes in the area.

The three dimensional position coordinates acquired from the DASM and DASA GPS stations over their period of observations have suggested a ground surface deformation rate of 48.5±0.2mm/yr North, 39.5±0.2mm/yr East and -9.5±0.7mm/yr Up; and 27.8±0.4mm/yr North, 43.9±0.5mm/yr East and -21.8±1.4mm/yr Up for DASM and DASA GPS stations, respectively in an absolute sense. The Up component of DASM shows two characteristics, 2.8 mm/yr up to doy 150, 2008 and -25mm/yr afterwards. The DASA shows also -10mm/yr up to doy 147, 2008 and -29mm/yr afterwards. The InSAR time-series shows -44mm/yr Line of Sight (LOS) rate in both track. The correlation between the DASM GPS and track 028 is 0.75 and it has a correlation of 0.79 with track 278. Generally, the result from this investigation suggested that there is an active subsidence in the area which needs further attention.

Keywords: Deformation, InSAR, GPS, LOS

Table of Content

List of Figures

List of Tables

List of Acronyms

ASAR- Advanced Synthetic Aperture Radar

C/A-CODE – Coarse Acquisition code

CGPS –Continuous GPS

CIO –Conventional International Origin

CTRS-Conventional Terrestrial Reference System

DEM- Digital Elevation Model

ECA-European Space Agency

Envisat- Environmental Satellite

ECEF –Earth Center Earth Fixed Frame

EOP –Earth Orientation Parameters

FFT- Fast Furrier Transform

GAMIT-GPS ANALYSIS at MIT

GLOBK – Global kalman filter

GPS –Global positioning system

GPST- Global Positioning System Time

GNSS – Global navigation and satellite system

InSAR- Interferomeric Synthetic Aperture radar

IERS – International Earth Rotation Services

IGS –International GNSS Service

ITRF –International Terrestrial Reference Frame

ITRS –International Terrestrial Reference System

LOS – Line of Sight

Ma-Million ago

My-million years

MST- Minimum Spanning Tree

P-CODE – Precision CODE

PU- Phase Unwrapping

PI-RATE – Poly Interferometric Rate And Time-series Estimator

ROI-PAC- Repeat Orbit Interferometry-Package

RINEX –Receiver Independent Exchange format

SAR- Synthetic Aperture Radar

SLC- Single Look complex

SNR- Signal to Noise Ratio

SVD- Single Value Decomposition

UT –Universal Time

UT1 – Universal Time corrected due to polar motion

UTC –Universal Time coordinate

VCM- Variance Covariance Matrix

Chapter One

1. Background

1.1. Introduction

This study is carried out to investigate the deformation measurement in the Central Afar, in the north eastern part of Ethiopia. The specific location is as indicated in Figure 1-1. Deformation is a change in location or a movement through time. Deformation can be uplift (i.e. when a place move up from previous location), subsidence (i.e. when a ground moves down relative to the previous position). Thus, this study addresses which kind of deformation is happening in the study area.

The tectonically active Afar Depression is one of the rare areas where one can study the transition from continental rift to sea floor spreading on dry land. The study area, Central Afar, include towns such as Logia, Dubti, and Semera the capital city of the Regional State of Afar. These towns are located within a triple junction formed by three rift systems which divide the three diverging plates namely: Nubian, Arabian and Somalian plates. The towns are homes for large population and many capital intensive infrastructure developments are underway in the area. Thus, understanding the sub-surface activity (magmato-tectonics) in the area is crucial for geohazard mitigation and plans the development activity. This area is geologically well investigated by many researchers among which the general geology by Abbate, et al., (1995) and structural geology by Acocella, et al., (2008), can be cited. The area comprises the Manda Hararo Rift (MHR) and Tendaho Graben (TG). In addition to the studies for tectonic activities, the Tendaho Graben is also intensively studied for geothermal production (Battistelli, et al., 2002). The 2005 seismo-tectonic event at the Dabahu-Manda-Hararo graben is one of the major events in the area that showed the tectonic activity of the Central Afar area.

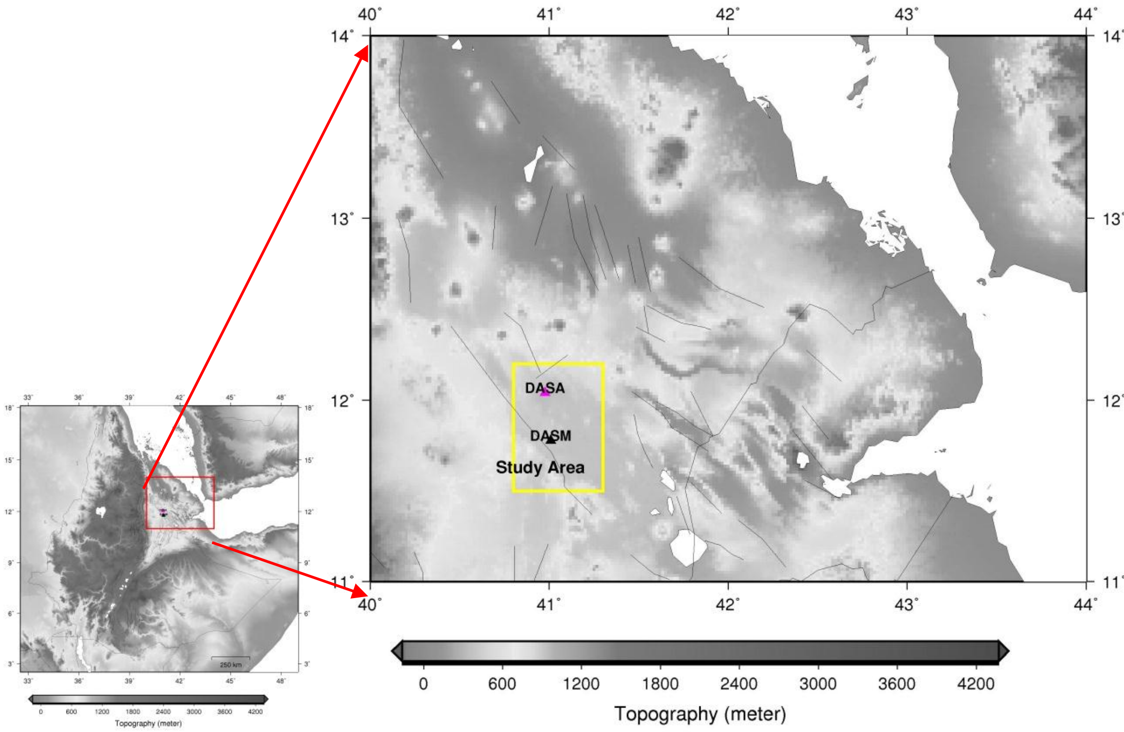

Figure 1-1 Location map of the area (DASA is GPS station at Saha and DASM is at Semera, the rectangle shows the specific study area.)

1.2. Geology and Tectonic setting of the Study area

The study area, in Central Afar, is located within the triple junction that divides the Nubian, Arabian and Somalian diverging plates. This area is tectonically active and structurally complex. This is especially manifested during the major rifting episode in 2005, associated with the emplacement of a dike 60 km long and up to 8 m wide at the Dabahu-Manda-Hararo (DMHR) rift (Wright et. al., 2006). During this event dike intrusion was accompanied by seismic activity. The 2005 episode shows the importance of catastrophic magma emplacement in the development of the rift (Wright, et al., 2006; Ayele, et al., 2007). To the south, DMHR grades into the northern Tendaho graben(TG). (Acocella, et al., 2008)

The main focus of this study is on the 'Central Afar' region south of the DMHR. Thus, the following section will be devoted to briefly explain the major rift systems (Dabbahu-Manda Hararo and the Tendaho graben). For the sake of completeness general view of the Afar triple junction is described briefly.

1.2.1.The Afar Triangle

The Afar Triangle (Figure 1-2) is an area of active extensional tectonics and basaltic magmatism from which the Gulf of Aden, the Red Sea and the Ethiopian rift system radiate. Normal faults and open fissures are the principal elements of the Afar tectonics. However, strike slip faults are also recognizable in the area. These faults are strike parallel to, or at small angle with, the rifting axis. (Abbate, et al., 1995)

In general, Afar is narrow intercontinental rifts. It is most likely to be a result of plume heads rising from deep within the mantle, probably from the thermal boundary layer at the core–mantle boundary. The Afar hotspot first appeared approximately 40 Ma ago with the outpouring of flood basalts in the Ethiopian highlands, and igneous activity in the Yemen, precursors of rifting and spreading in the Red Sea and Gulf of Aden (Kearey, et al., 2009).

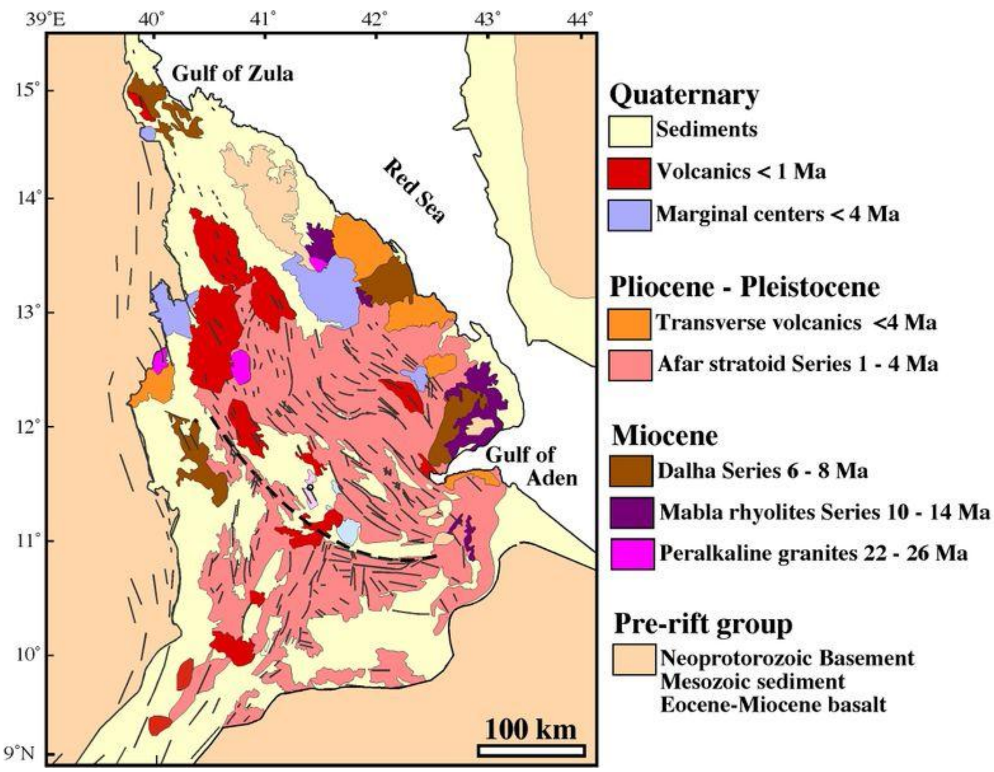

Figure 1-2 Simplified Geology of the Afar Triangle (Beyene, et al., 2005)

Continental rifts are regions of extensional deformation where the entire thickness of the lithosphere has deformed under the influence of deviatoric tension. The rift segment in Afar is characterized by voluminous magmatism and the eruption of continental flood basalts. Southwest of the Afar triple-junction, the Nubian and Somalian Plates are moving apart at a rate of approximately 6-7mm/yr (Fernandes, 2004). This divergent plate motion results in extensional deformation that is localized into a series of discrete rift segment of variable age, including the Western Rift, the Eastern Rift, the Main Ethiopian Rift, and the Afar Depression. (Kearey, et al., 2009)

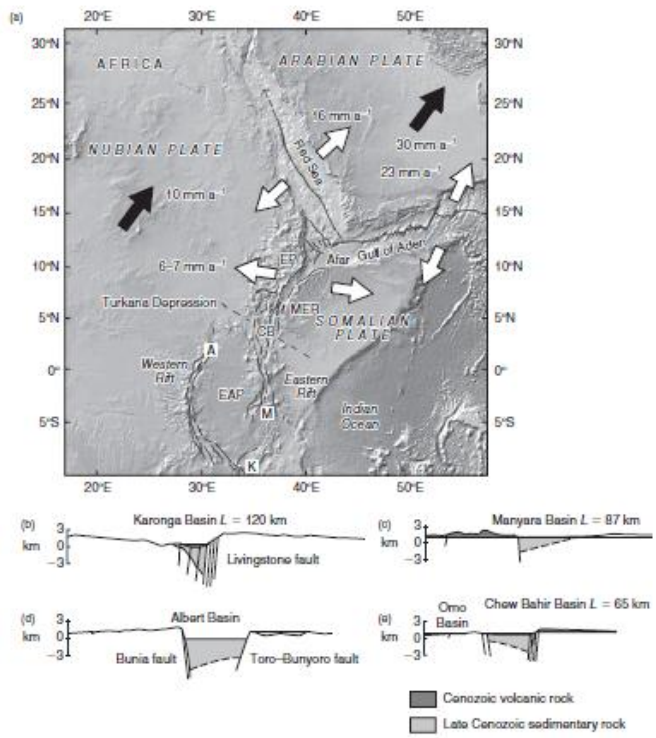

Figure 1-3 (a) Shaded relief map and geodynamic setting of the East African Rift system constructed using digital topography data. White arrows indicate relative plate velocities, Black arrows indicate absolute plate motion in a geodetic, no-net-rotation (NNR) framework. (b-e) Cross-sections showing fault and half-graben morphology. K, karanga basin; A, Albert basin; CB, Chew Bahir basin; EAP, East African Plateau; EP, Ethiopian Plateau; MER, Main Ethiopian rift; I, the length of the border fault (Kearey, et al., 2009)

The rift segments in the Afar Depression illustrate that, as extension increases and the thickness of the lithosphere decreases, the asthenosphere rises and decompresses, and more melt is generated. Eventually all the border faults in the rift are abandoned as magmatism accommodates the extension (Figure 1-3.c). At this stage the rift functions as a slow-spreading mid ocean ridge that is bordered on both sides by thinned continental lithosphere (Wolfenden, 2005). As the melt supply increases and/or strain rate increases, new oceanic lithosphere forms in the magmatic segments and the crust and mantle lithosphere subside below sea level (d'Acremont, 2005).

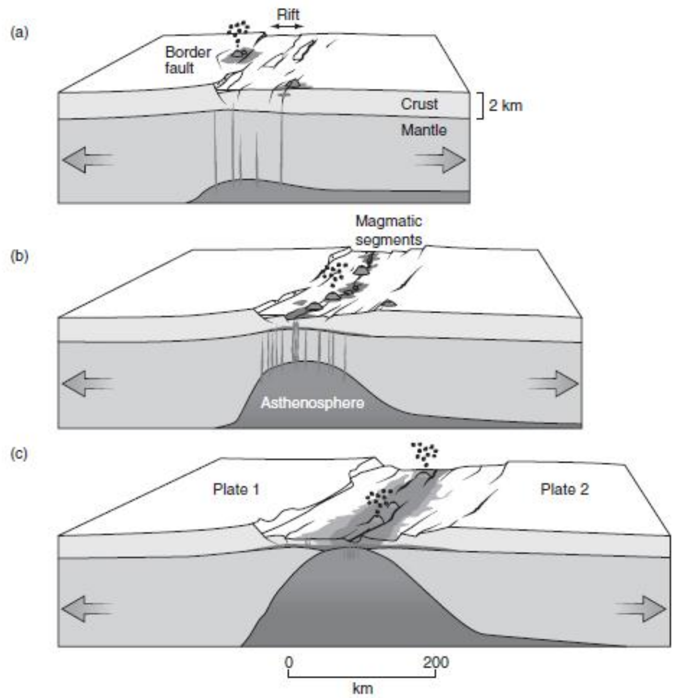

Figure 1-4 Three-stage model for continental break-up loading to the formation of a volcanic passive margin (Kearey, et al., 2009)and the reference described there.

Seismic reflection studies indicate that the southern rifted margin is about twice as wide as the northern one and displays thicker post-rift deposits and greater amounts of subsidence. As rifting gave way to sea floor spreading in this area, deformation localized in a 40-km-wide transition zone where magma intruded into very thin continental crust and, possibly, in the case of the northern side, exhumed mantle (Kearey, et al., 2009).

1.2.2.Central Afar

Central Afar includes the NW-SE trending Tendaho Graben (TG), the largest basin of Central Afar, and the younger (Acocella, et al., 2008) and active NW-SE trending Manda Hararo Rift (MHR). TG marks the northern limit of the MER structures. (Acton, et al., 2000) TG is several tens of km wide and a few hundred kilometres long and hosts eruptive fissures and central volcanoes. Its bedrock mainly comprises Stratoid deposits, which generally young toward the central part of the graben (Kidane, et al., 2003).

Tectonic and volcanic activity within TG developed mostly between ~1.8 and ~0.6 Ma, with a stretching factor of ~1.1, an extension rate ~3.6 mm/yr and the fissural eruption of part (~7000 km^3/Ma) of the Afar Stratoid sequence (mainly basaltic lava flows and ignimbrites). MHR, before terminating southward, has a stretching factor ~1.04 and an extension rate ~1.2 mm/yr, and is associated with the emission of ~ 600 m^3/Ma of basalt in the last ~0.2 Ma. These data suggest that after the exceptional amount of magma erupted between ~1.8 and ~0.6 Ma, magmatic and tectonic activity significantly decreased along the southern part of the Red Sea propagator in the last ~0.2 Ma. This decrease coincides with the on-land development and migration of the more active (inferred extension rate in the order of ~10 mm/yr, as proposed in previous studies) Aden propagator, suggesting that spreading in Central Afar mainly occurred along one active propagator at any one time (Acocella, et al., 2008).

1.2.2.1. Tendaho Rift/Graben

The NW-trending Tendaho Rift is a southern portion of the Erta Ale- Hararo Manda rift system, which extends the active tectonics of the Red Sea to the south (Abbate, et al., 1995). Tendaho Grabben (TG) is ~200 km long and its width varies from ~30 km near its northern and southern tips to >50 km in its center. TG interrupts the continuity of MER, as suggested by the abrupt termination of the structures forming the latter (Acocella, et al., 2008).

Tendaho Rift does not merely swerve into the Ethiopian Rift, but is prolonged east of the latter by the Goba Ad structure. This is a half-graben of limited length devoid of recent magmatic activity which shrinks and dies out east-ward (Abbate, et al., 1995).

The flanks of the Tendaho Rift are in the Afar Stratoid Series; the rift is filled with lacustrine and alluvial deposits and with post-Stratoid basalt flows. This filling is topped by recent volcanoes, among which the historically active Kurub and the Dama Ali.

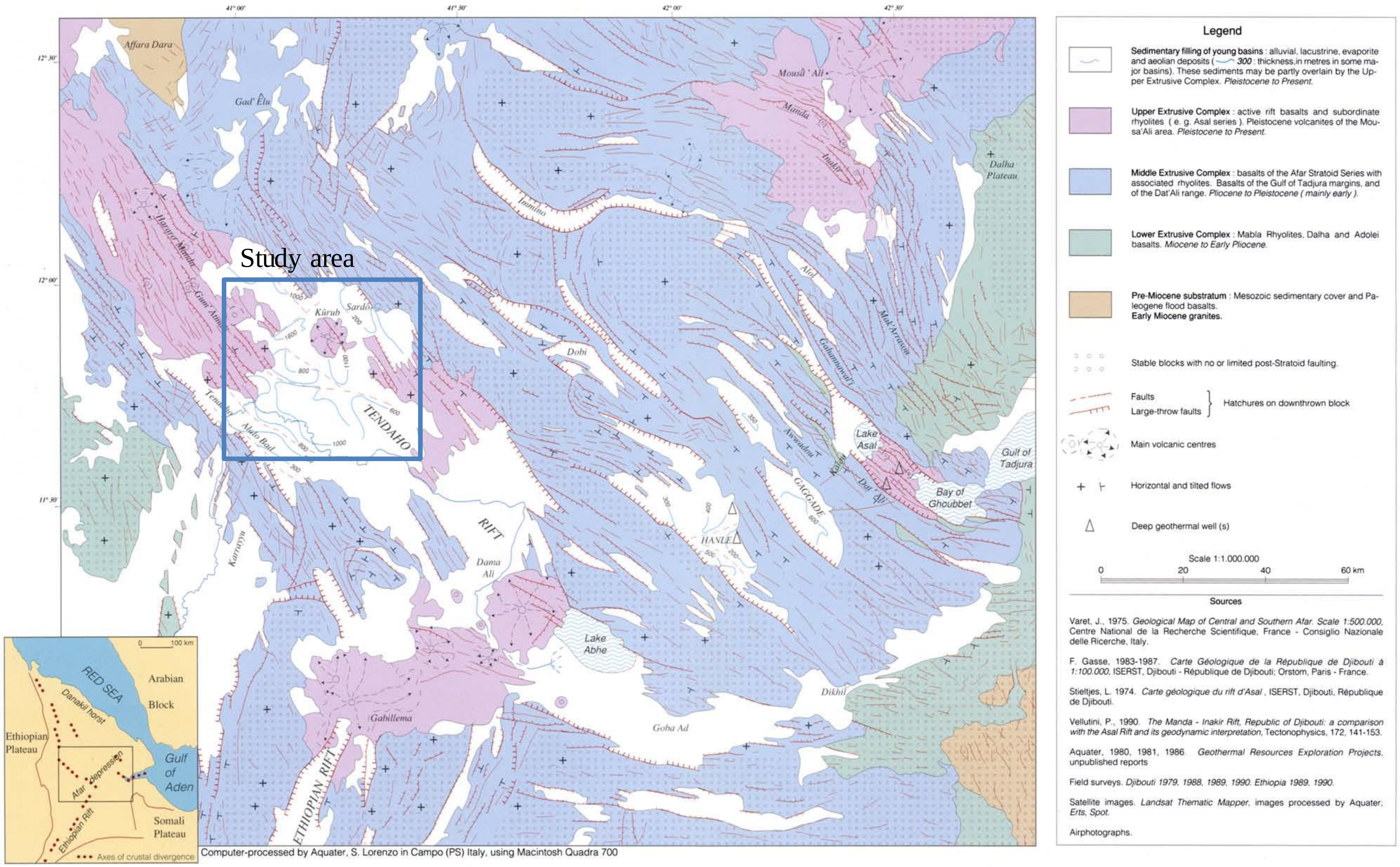

Figure 1-5 Map of the Geological Structures of the Central Afar Region[1] (Abbate, et al., 1995)

---

[1] L. Zan, Aquater S.p.A., S. Lorenzo in Campo (PS) Italy
E. Abbate, P. Passerini, Dipartimento di Soienze della Terra, Universitat di Firenze, Florence Italy

Hydrothermal vents are common at Alalo Bad and near Dubti (northeast of Tendaho) (Abbate, et al., 1995). The bounding faults of the TG are the Logia fault on the west and the Gamare fault on the east (Acton, et al., 2000).

The difference in height between the rift floor and its shoulders is few hundreds of meters, but geoelectric prospecting between Tendaho and Serdo indicates a sedimentary filling locally thicker than 1600 m. The real thickness of the sediments may be locally greater, since near Dubti a geothermal well drilled down to 2100 m in 1994 found 1500 m of sediments against only 1000 indicated by geoelectric prospecting (Abbate, et al., 1995).

The wavelength of the faulted blocks, interestingly, is approximately the same in the thick basalts of the Afar Stratoid Series at the rift borders, and in the recent basalts alternating with abundant sedimentary levels in the inner floor of the rift. Their tectonic style is thus poorly sensitive to the superficial lithologies and presumably rooted at depth beneath the rift. This pattern of closely spaced, small-throw faults suggests the existence of a relatively thin brittle lid, underlain by a shallow soft layer with down- ward increasing density which damps the vertical offsets. This applies to many sections of the Afar Triangle with similar tectonic style. Such kind of rift structure can be accounted for by extension (Abbate, et al., 1995).

The overall architecture of TG is characterized by (Acocella, et al., 2008) the following features:

- The NE and SW shoulders consist of subhorizontal Stratoid layers, often dissected by NW-SE trending faults.
- At the NE and SW graben margins, marked by the highest visible scarps, the subhorizontal Stratoid layers end, forming inward dipping Stratoid blocks arranged in a domino configuration inside the margins. The dominos, usually ~1 km wide, are bordered by NW-SE trending faults which dip away from the graben axis; the displacement of these faults decreases toward the graben axis, in a similar fashion to the amount of tilt of the blocks that they bound (between $30^{o}$and 5^{o}).

- Stratoids in the inner portion of TG are deformed into a broad NW-SE trending syncline-like structure, formed by the tilted blocks separated by the NE-SW trending faults.

1.2.2.2. Manda Hararo Rift/graben

The Manda Hararo Rift (MHR) constitutes the currently active axial zone of the Tendaho Graben. The part of MHR studied here is located along the southern termination of the basaltic plateau surrounded by sedimentary and subordinate volcanic deposits. While the plateau is highly fractured, with fault scarps reaching several meters of vertical displacement, the surrounding deposits do not appear to be faulted or fractured (Acocella, et al., 2008).

The Dabbahu magmatic segment is about 60km long and 15km wide. At the northern end of the segment are the major silicic strato-volcano Dabbahu and the smaller Gab'ho volcano and in the south is the Ado'Ale silicic central volcanic complex (Rowland, et al., 2007).

Dabbahu volcano is 1350m above sea level and about 10km diameter. To the northwest is a linear vent zone with smaller volcanoes and cinder cones and to the south is a well developed axial graben which decreases in size towards Ado'Ale. The Ado'Ale volcanic complex covers a wide area of the central Dabbahu magmatic segment and is over 750m above sea level. To the south of Ado'Ale the elevation of the rift zone drops beneath the regional level (Rowland, et al., 2007).

The faults at the MHR often form opposite-facing scarps, between ~1 to ~10 m high arranged in graben-like structures. Extension fractures, up to a few hundreds of meter long and a few meters wide, are usually found in these grabens. The overall architecture of the foot-wall (flat layers) and hanging-wall (domino decreasing with distance) of the normal fault separating the eastern and western plateau is remarkably similar to that observed at the borders of TG. The mean dip of the faults at the axial zone is estimated to be 80^o. Bookshelf faulting accommodates extension along the TG and MHR (Acocella, et al., 2008).

The location of the youngest Stratoid deposits, in the NE part of TG broadly coincides with the axis of Tendaho Rift, defined by the attitude of the same deposits. Moreover, the rift axis is also coincident with the younger (<0.22 Ma) volcanic deposits of Kurub, Manda Gargori and Dama Ale. This suggests a spatial relationship between the inferred area of emission of the Stratoids, a part of the more recent volcanism and the structure of TG. It is speculated that the rift axis of TG may be the surface expression of a subsided area related to a previous phase of magma withdrawal. The Tendaho rift axis may have been the focus of subsidence, spreading and volcanism from ~1.8 to ~0.6 Ma. From ~0.2 Ma, volcanic activity was restricted to selected spots (Kurub, Manda Gargori and Dama Ale; figure 1-6), while the new focus of spreading, with moderate extension rates and eruptive volumes, migrated to MHR. In this setting, the Kurub, Manda Gargori and Dama Ale volcanic system is interpreted to result from the gradual termination of the former Tendaho Rift, rather than being the southern continuation of the Manda Hararo Rift. Therefore it appears that 2 main offset and non-overlapping spreading axes have been active, in part simultaneously, within TG in the last ~1.8 Ma, in a context of decreasing volcanic and tectonic activity (Acocella, et al., 2008).

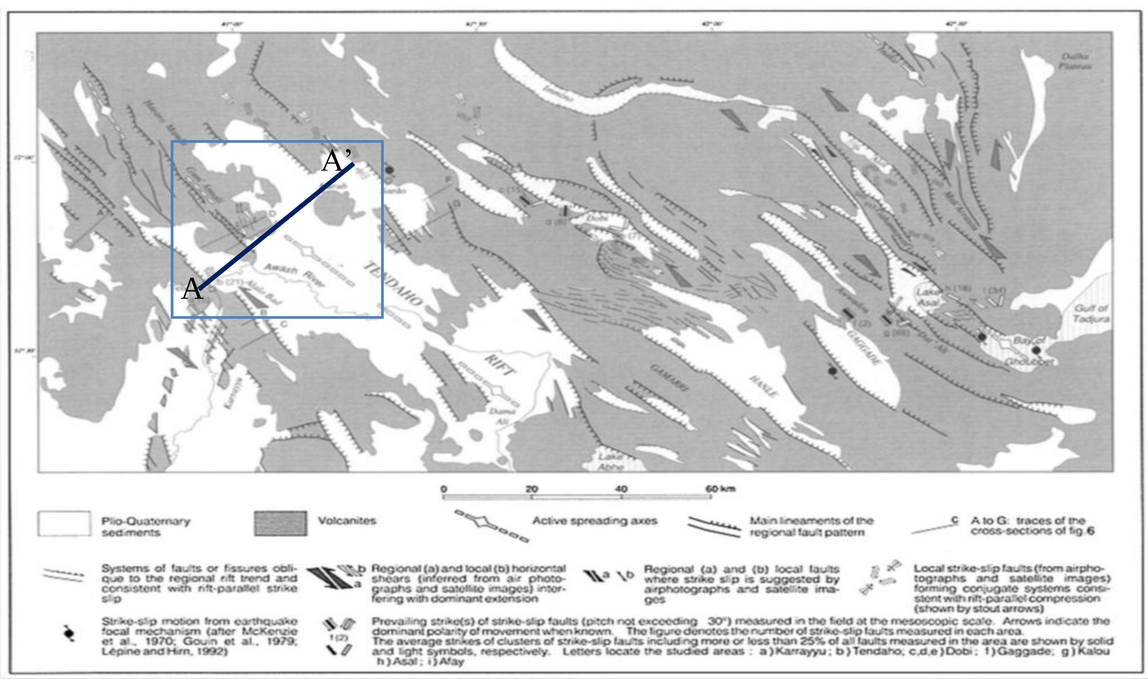

Figure 1-6: Structural scheme of the strike-slip movements of the Central Afar (Abbate, et al., 1995) the box shows study area. The line AA' is the profile for model of geological crosection and gravity and magnetics (Bridges, et al., 2012)

1.3. Objectives

1.3.1. Main Objective

The main objective of this study is to determine the deformation in the study area using Interferometric Synthetic Aperture Radar (InSAR) and Global Positioning System (GPS) time series.

1.3.2. Specific objectives

The specific objectives are:

- Measuring deformation using InSAR
- Measuring deformation using GPS
- Comparing the GPS and InSAR timeseries to determine the rate of deformation

1.4. Overview of the Thesis

This thesis looks at the application of GPS and InSAR for deformation analysis in Central Afar. Each chapter deals with the fundamental theories and principles as well as the data used in the analysis of the deformation. It can be described as follow:

Chapter 2: covers the basics of GPS theory, coordinate systems, reference frames, time systems and orbital parameters to describe the satellite orbits. It also describes the GPS signal and list the errors associated with measurement and respective mitigation.

Chapter 3: lists the international and local data source for GPS data processing and describe the work flow how to process GPS data using GAMIT/GLOBK software.

Chapter 4: describes the result of the GPS processing. The result inferring the timeseries of the GPS stations is also discussed.

Chapter 5: covers the basics of InSAR. It also lists the Envisata data used in this thesis. There is a quantitative description of conditions for InSAR in Central Afar, with in the triple junction with sections, source of errors in InSAR data analysis, namely, orbital errors, atmospheric errors and unwrapping, coherence, and the deformation signal.

Chapter 6: describes the results for the two tracks used in this study: track 028 which is ascending and track 278 which is descending. The result from InSAR processing is also discussed. In addition, it addresses the comparison between the results from GPS measurement with InSAR measurement changing the 3D GPS topocentric time-series into satellite line of site (LOS). Finally, it describes the overall discussion.

Chapter 7 is the last chapter in this thesis which describes the conclusions drawn from the study and the recommendation suggested.

Chapter Two

Method I

2. Theory of GPS

2.1. Introduction

2.1.1. GPS

GPS is a Global Positioning System based on satellite technology. The fundamental technique of GPS is to measure the ranges between the receiver and a few simultaneously observed satellites. The positions of the satellites are forecasted and broadcasted along with the GPS signal to the user. Through several known satellite positions and the measured distances between the receiver and the satellites, the position of the receiver can be determined. The position change, which can be also determined, is then the velocity of the receiver (ParkinsonBW, 1996).

The GPS satellites are monitored by five base stations. The main base station is in Colorado Springs, Colorado and the other four are located on Ascension Island (Atlantic Ocean), Diego Garcia (Indian Ocean), Kwajalein and Hawaii (both Pacific Ocean). All stations are equipped with precise cesium clocks and receivers to determine the broadcast ephemerides and to model the satellite clocks. Transmitted to the satellites are ephemerides and clock adjustments. The satellites in turn use these updates in the signals that they send to GPS receivers.

The orbits of the GPS satellites are available through the broadcast of the information with other information or from other sources such as the International GNSS Service (IGS). IGS orbits are precise ephemerides after post-processing or quasi-real time processing. All GPS receivers have an almanac programmed into their computer, which tells them where each satellite is at any given moment.

Figure 2-1 Position of the Master control station and the Monitor stations (NASA-Earthmap, 2013)

The almanac is a data file that contains information of orbits and clock corrections of all satellites. It is transmitted by a GPS satellite to a GPS receiver, where it facilitates rapid satellite vehicle acquisition within GPS receivers. The GPS receivers detect, decode and process the signals received from the satellites to create the data of code, phase and Doppler observables. The data may be available in real time or saved for downloading (Guochang Xu, 2007).

Nowadays, in addition to GPS, there are more satellite constellations which are run by different countries. However, all have nearly the same positioning and navigating principles. Among them, Galileo is for the EU, GLONASS is a Russian and Compass is a Chinese. A global navigation satellite system of the future is a combined Global Navigation Satellite System (GNSS) by using the GPS, GLONASS, Galileo and others systems together (Guochang Xu, 2007).

2.1.2.GPS Segments

GNSS has three main segments, namely: Space Segment, Control Segment and User Segment. The combinations of these three segments give precise coordinate. Each one has its own tasks.

2.1.5.1. Space Segment

The Space Segment, which includes the constellation of ~30 GPS satellites that transmit the signals from space down to the user, including information that can be used to compute the receiver's position.

Figure 2-2 Space Segment constellation (M. Hern´andez-Pajares, 2008)

2.1.5.2. Control Segment

The Control Segment (in the US Department of Defense) which is responsible for the monitoring and operation of the Space Segment, including the uploading of information that can predict the GPS satellite orbits and clock errors into the near future, which the Space Segment can then transmit down to the user. Control Station can be divided into Master Control station and Monitoring Stations (Hofmann-Wellenhof, et al., 2008).

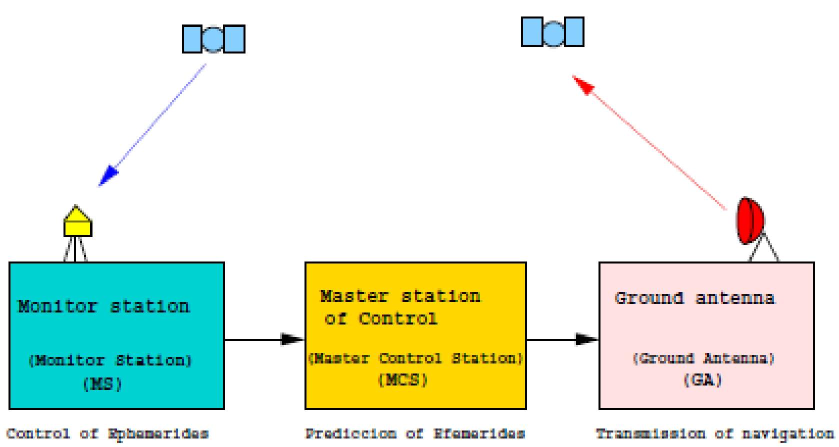

Figure 2-3 Control Segment diagram (Seeber, 2003)

2.1.5.3. User Segment

The User Segment, which includes the user's GPS hardware (receivers and antennas) and GPS data-processing software for various applications, including surveying, navigation, and timing applications.

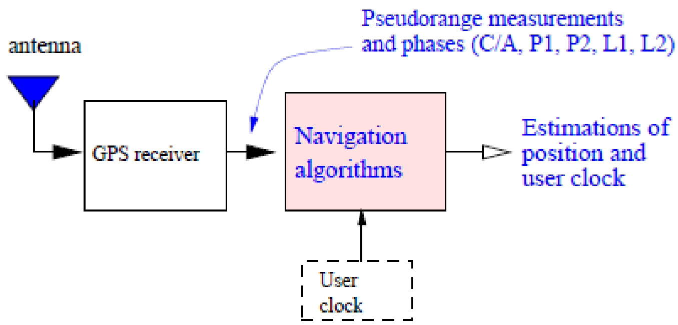

Figure 2-4 Basic scheme of a GPS reciever (M. Hern´andez-Pajares, 2008)

2.2. Coordinate and Time System

In order to describe the GPS observation as a function of the GPS satellite orbit and the measuring station location, suitable coordinate and time systems have to be defined. Most of the subsections hereafter are used to define these spatial and temporal references implemented in the software that is used to process the GPS data in this work.

2.2.1.Geocentric Earth-Fixed Coordinate Systems

It is convenient to use the Earth-Centered Earth-Fixed (ECEF) coordinate system to describe the location of a station on the Earth's surface. The ECEF coordinate system is a right-handed Cartesian system (x, y, z). Its origin and the Earth's center of mass coincide, while its z-axis and the mean rotational axis (mean pole) of the Earth coincide; the x-axis is pointing to the mean Greenwich meridian, while the y-axis is directed to complete a right-handed system (figure 2.5). Then the xy-plane is called mean equatorial plane, and the xz-plane is called mean zero-meridian.

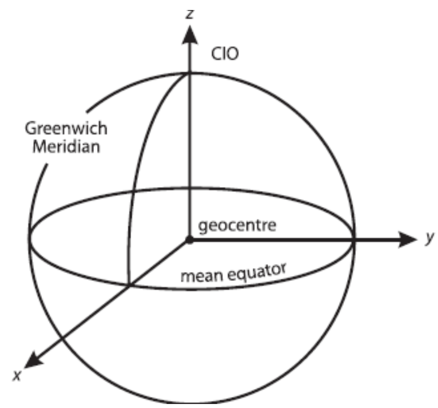

Figure 2-5 Earth-Centered Earth-Fixed Coordinate system (Guochang Xu, 2007)

2.2.2.Coordinate System Transformations

Any Cartesian coordinate system can be transformed to another Cartesian coordinate system through three successive rotations if their origins are the same and if they are both right-handed or left-handed coordinate systems.

For two Cartesian coordinate systems with different origins and different length units, the general transformation can be given in vector (matrix) form as:

$$\boldsymbol{X_n = X_0 + \mu R X_{old}},\ or \begin{pmatrix} x_n \\ y_n \\ z_n \end{pmatrix} = \begin{pmatrix} x_0 \\ y_0 \\ z_0 \end{pmatrix} + \mu R \begin{pmatrix} x_{old} \\ y_{old} \\ z_{old} \end{pmatrix} \quad \ldots\ldots\ldots\ldots\ldots\ldots\ldots\ldots \ (2.1)$$

Where, $\boldsymbol{\mu}$ is the scale factor (or the ratio of the two length units), and R is a transformation matrix that can be formed by three suitably succeeded rotations. $\mathbf{X_n}$ and $\mathbf{X_{old}}$ denote the new and old coordinates, respectively; $\mathbf{X}_0$ denotes the translation vector and is the coordinate vector of the origin of the old coordinate system in the new one.

2.2.3.Local coordinate system (Topocentric)

The local left-handed Cartesian coordinate system (x', y', z') can be defined by placing the origin to the local point $P_1(x_1, y_1, z_1)$, whose z'-axis is pointed to the vertical, x'-axis is directed to the north, and y' is pointed to the east (figure 2-6). The x'y'-plane is called the horizontal plane; the vertical is defined perpendicular to the ellipsoid. Such a coordinate system is also called a local horizontal coordinate system. For any point P_2, whose coordinates in the global and local coordinate system are (x_2, y_2, z_2) and (x', y', z'), respectively, one has relations:

$$\begin{pmatrix} x' \\ y' \\ z' \end{pmatrix} = d \begin{pmatrix} cosAsinZ \\ sinAsinZ \\ cosZ \end{pmatrix}, and \begin{pmatrix} d = \sqrt{x'^2 + y'^2 + z'^2} \\ tanA = {y'}/{x'} \\ cosZ = {z'}/{d} \end{pmatrix}, \quad \ldots\ldots\ldots\ldots..(2.2)$$

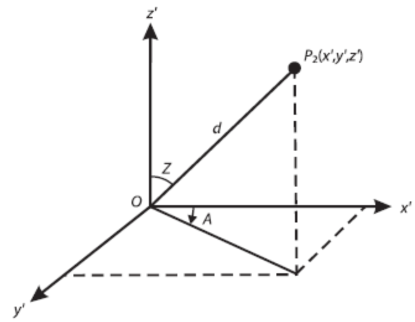

Figure 2-6Astronomical Coordinate System (Guochang Xu, 2007)

Where, A is the azimuth, Z is the zenith distance and d is the radius of the P_2 in the local system. A is measured from the north clockwise; Z is the angle between the vertical and the radius d. The local coordinate system (x', y', z') can indeed be obtained by two succeeded rotations of the global coordinate system (x, y, z) by $R_2(90° - \varphi)R_3(\lambda)$ and then by changing the x-axis to a right-handed system. In other words, the global system has to be rotated around the z-axis with angle λ, then around the y-axis with angle (90° –φ), and then change the sign of the x-axis. The total transformation matrix R is then

$$R = \begin{pmatrix} -sin\varphi cos\lambda & -sin\varphi sin\lambda & cos\varphi \\ -sin\lambda & cos\lambda & 0 \\ cos\varphi cos\lambda & cos\varphi sin\lambda & sin\varphi \end{pmatrix}, \ldots\ldots\ldots (2.3)$$

And there are: $X_{local}=RX_{global}$ and $X_{global}=R^TX_{local}$, …………. (2.4)

Where Xl_{ocal} and X_{global} are the same vector represented in local and global coordinate systems. (φ,λ) are the geodetic latitude and longitude of the local point (Guochang Xu, 2007).

2.2.4.Earth-Centered Inertial Coordinate System

To describe the motion of the GPS satellites, an inertial coordinate system has to be defined which follows the Newtonian mechanics. For this purpose, the Conventional Celestial Reference Frame (CRF) is suitable. The xy-plane of the CRF is the plane of the Earth's equator; the coordinates are celestial longitude, measured eastward along the equator from the vernal equinox, and celestial latitude. The vernal equinox is a crossover point of the ecliptic and the equator. So the right-handed Earth-centered inertial (ECI) system uses the Earth center as the origin, CIO (Conventional International Origin) as the z-axis, and its x-axis is directed to the equinox of J2000.0 (Julian Date of 12h 1st January 2000). Such a coordinate system is also called equatorial coordinates of date (Guochang Xu, 2007).

Figure 2.7 illustrates the motion of the Earth's pole with respect to the ecliptic pole. We can transform the ECI system with a geometric way to the ECEF system. Such a transformation process can be written as

$$\boldsymbol{X_{ECEF}} = \boldsymbol{R_M R_S R_N R_P X_{ECI}}\ , \quad \ldots\ldots\ldots\ldots\ldots\ldots \quad (2.5)$$

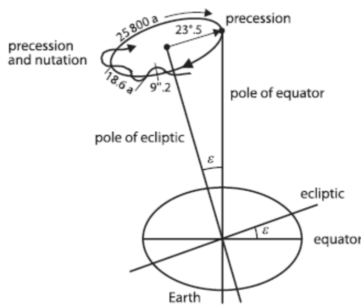

Figure 2-7 Precession and Nutation (Hofmann-Wellenhof, et al., 2008)

Where R_P is the precession matrix, R_N is the nutation matrix, R_S is the Earth rotation matrix, R_M is the polar motion matrix, X is the coordinate vector, and indices ECEF and ECI denote the related coordinate systems (Guochang Xu, 2007).

2.2.5.Precession

The precession matrix consists of three succeeded rotational matrices, i.e., (Hofmann-Wellenhof, et al., 2008) $R_P=R_3(-z)R_2(\theta)R_3(-\zeta)$

$$= \begin{pmatrix} cosz cos\theta cos\zeta - sinz sin\zeta & -cosz cos\theta sin\zeta - sinz cos\zeta & -cosz sin\theta \\ sinz cos\theta cos\zeta + cosz sin\zeta & -sinz cos\theta sin\zeta + cosz cos\zeta & -sinz sin\theta \\ sin\theta cos\zeta & -sin\theta sin\zeta & cos\theta \end{pmatrix}, \ldots\ldots(2.6)$$

Where z,θ,ζ are precession parameters and $z = 2306.2181T + 1.09468T^2 + 0.018203T^3$, $\theta = 2004.3109T - 0.42665T^2 - 0.041833T^3$, $\zeta = 2306.2181T + 0.30188T^2 + 0.017998T^3$, Where T is the measuring time in Julian centuries (36 525 days) counted from J2000.0. (Guochang Xu, 2007)

2.2.6.Nutation

The nutation matrix consists of three succeeded rotational matrices, i.e., (Hofmann-Wellenhof, et al., 2008)

$$\mathbf{R_N = R_1(-\varepsilon-\Delta\varepsilon)R_3(-\Delta\psi)R_1(\varepsilon)}$$

$$= \begin{pmatrix} cos\Delta\psi & -sin\Delta\psi cos\varepsilon & -sin\Delta\psi sin\varepsilon \\ sin\Delta\psi cos\varepsilon_t & cos\Delta\psi cos\varepsilon_t\, cos\varepsilon + sin\varepsilon_t sin\varepsilon & cos\Delta\psi cos\varepsilon_t\, sin\varepsilon - sin\varepsilon_t cos\varepsilon \\ sin\Delta\psi sin\varepsilon_t & cos\Delta\psi sin\varepsilon_t\, cos\varepsilon + cos\varepsilon_t sin\varepsilon & cos\Delta\psi cos\varepsilon_t\, sin\varepsilon - cos\varepsilon_t cos\varepsilon \end{pmatrix}$$

$$\approx \begin{pmatrix} 1 & -\Delta\psi cos\varepsilon & -\Delta\psi sin\varepsilon \\ \Delta\psi cos\varepsilon_t & 1 & -\Delta\varepsilon \\ \Delta\psi sin\varepsilon_t & \Delta\varepsilon & 1 \end{pmatrix}, \quad \dots\dots\dots\dots\dots\dots\dots\dots\dots\dots \text{(2.7)}$$

Where ε is the mean obliquity of the ecliptic angle of date, Δψ and Δε are nutation angles in longitude and obliquity. The coefficients and the updated formulas and tables can be found in updated IERS conventions (Guochang Xu, 2007).

2.2.7.Earth Rotation

The Earth rotation matrix can be represented as:

$$R_s = R_3(GAST), \dots\dots\dots\dots\dots\dots\dots\dots.. \text{(2.8)}$$

Where GAST is Greenwich Apparent Sidereal Time and

$$GAST = GMST + \Delta\Psi cos\varepsilon + 0.00264 sin\Omega + 0.000063 sin2\Omega, \dots\dots\dots\dots \dots\text{(2.9)}$$

Where, GMST is Greenwich Mean Sidereal Time. Ω is the mean longitude of the ascending nod of the Moon; the second term on the right-hand side is the nutation of the equinox. Furthermore,

$$GMST = GMST_0 + \alpha UT1, \dots\dots\dots\dots\dots \dots\text{(2.10)}$$

$GMST_0 = 6x3600.0 + 41x60.0 + 50.54841 + 8640184.812866T_0 + 0.093104T^2{}_0 - 6.2x10^{-6}T^3{}_0$,

$\alpha = 1.002737909350795 + 5.9006 \times 10^{-11}T_0 - 5.9 \times 10^{-15}T^2{}_0$, where, $GMST_0$ is Greenwich Mean Sideral Time at midnight on the day of interest. α is the rate of change. UT1 is the polar motion corrected Universal Time (Guochang Xu, 2007).

2.2.8.Polar Motion

As shown in Figure 2-8, the polar motion is defined as the angles between the pole of date and the CIO pole.

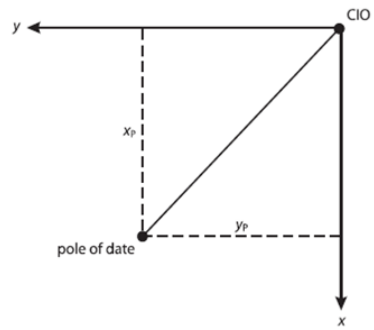

Figure 2-8 Polar Motion (Hofmann-Wellenhof, et al., 2008)

The polar motion coordinate system is defined by xy-plane coordinates, whose x-axis is pointed to the south and is coincided to the mean Greenwich meridian, and whose y-axis is pointed to the west. x_p and y_p are the angles of the pole of date, so the rotation matrix of polar motion can be represented as:

$$R_M = R_2(-x_p)R_1(-y_p) = \begin{pmatrix} cosx_p & sinx_p siny_p & sinx_p cosy_p \\ 0 & cosy_p & siny_p \\ -sinx_p & cosx_p siny_p & cosx_p cosy_p \end{pmatrix} \quad \text{.............. (2.11)}$$

The IERS determined x_p and y_p can be obtained from the home pages of IERS (Guochang Xu, 2007).

2.2.9. Time Systems

Three time systems are used in satellite geodesy. They are sidereal time, dynamic time, and atomic time. Sideral time is a measure of the Earth's rotation and is defined as the hour angle of the vernal equinox. If the measure is counted from the Greenwich meridian, the sidereal time is called Greenwich Sidereal Time. Universal Time (UT) is the Greenwich hour angle of the apparent Sun, which is orbiting uniformly in the equatorial plane. Because the angular velocity of the Earth's rotation is not a constant, sidereal time is not a uniformly-scaled time. The oscillation of UT is also partly caused by the polar motion of the Earth. The universal time corrected for the polar motion is denoted by UT1.Dynamical time is a uniformly-scaled time used to describe the motion of bodies in a gravitational field. Terrestrial Dynamic Time (TDT) is used in a quasi-inertial coordinate system (such as ECI). Because of the motion of the Earth around the Sun (or say, in the Sun's gravitational field), TDT will have a variation with respect to TDB. However, both the satellite and the Earth are subject to almost the same gravitational perturbations. Atomic

Time is a time system kept by atomic clocks such as International Atomic Time (TAI). It is a uniformly-scaled time used in the ECEF coordinate system. Because of the slowing down of the Earth's rotation with respect to the Sun, Coordinated Universal Time (UTC) is introduced to keep the synchronization of TAI to the solar day (by inserting the leap seconds). GPS Time (GPST) is also an atomic time. The relationships between different time systems UT1 and UTC is given as follows:

$$UT1 = UTC + dUT1, \quad \ldots\ldots\ldots\ldots\ldots\ldots\ldots\ldots\ldots(2.12)$$

where dUT1 can be obtained from IERS, (dUT1 < 0.7 sec), (dUT1 is also broadcasted with the navigation data), n is the number of leap seconds of date and is inserted into UTC on the 1st of January and 1st of July of the years (Guochang Xu, 2007).

2.3. Satellite Orbits

The application of Satellite geodesy depends substantially on knowing the satellite orbits. It is worth noting to know accurately the orbit of the satellite in effect to reduce error in position estimation. Orbital information is either transmitted by the satellite as part of the broad-cast message or can be obtained in the form of precise ephemerides from several sources. Currently, there are good precise orbits are available in near real time; however, the final precise ephemerides are available after ~11 days (Guochang Xu, 2007).

2.3.1.Keplerian Orbit parameters

According to Kepler's laws of orbital motion, each orbit takes the approximate shape of an ellipse, with the Earth's center of mass at the focus of the ellipse (Figure 2-9). For a GPS orbit, the eccentricity (e) of the ellipse is so small (0.02) that it is almost circular. The semi-major axis (a) of the ellipse is approximately 26 600 km, or approximately four times Earth radii. The six orbital planes rise over the equator at an inclination angle of 55^o. The point at which they rise from the Southern to Northern Hemisphere across the equator is called the 'Right Ascension of the ascending node' (Ω). Since the orbital planes are evenly distributed, the angle between the six ascending nodes is 60^o. Each orbital plane nominally contains four satellites, which are generally not spaced evenly around the ellipse. Therefore, the angle of the satellite within its own orbital plane, the 'true anomaly', is only approximately spaced by 90^{o}. The true anomaly is measured from the point of closest approach to the Earth (the perigee).

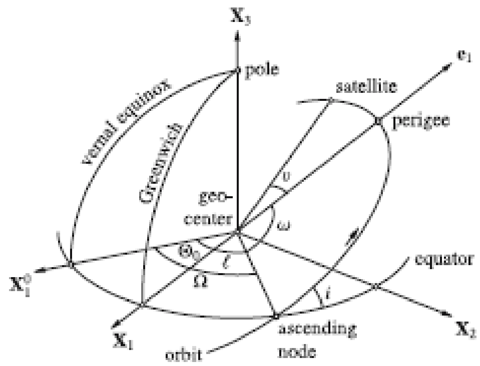

Figure 2-9 Keplerian Orbits (Hofmann-Wellenhof, et al., 2008)

Finally, the argument of perigee specifies the angle between the equator and perigee. Since the orbit is nearly circular, this orbital parameter is not well defined, and alternative parameterization schemes are often used. Taken together (the eccentricity(e), semi-major axis(a), inclination(i), Right Ascension of the ascending node(Ω), the time of perigee passing(τ), and the argument of perigee(ω)), these six parameters define the satellite orbit (according to the Keplerian model).

$$\boldsymbol{r}(t) = \boldsymbol{r}(t; a, e, i, \Omega, \omega, \tau) \text{……………………….(2.13)}$$

These parameters are known as Keplerian elements. Given the Keplerian elements and the current time, it is possible to calculate the coordinates of the satellite. However, GPS satellites do not move in perfect ellipses, so additional parameters are necessary. All the GPS satellites orbits are prograde, which means the satellites move in the direction of Earth’s rotation. Therefore, the relative motion between the satellite and a user on the ground must be less than 4 km/s. Typical values around 1 km/ s can be expected for the relative speed along the line of sight (range rate) (G. Blewitt, 2007).

2.4. GPS Measurements

2.3.1 GPS Signals

Satellite navigation systems, generally, can be grouped as active (receiver needs to emit signal) and passive (receiver do not emits signals) as well as one way (uplink or downlink) and two-way ranging system. The three major GNSS (GPS, GLONASS, Galileo) are passive one-way downlink ranging systems (Guochang Xu, 2007).

Satellite navigation relies on electromagnetic waves, whose characteristics are described by Maxwell's equations. An oscillating electric field causes a magnetic field through magnetic flux. Electric induction is the affiliated inverse effect. Electromagnetic waves can be represented by sinusoidal waves applying the theory of harmonic motion (Figure 2-10). Thus mathematically can be expressed as: $(t) = a \sin 2\pi f t$, where 'a' is amplitude of the signal, 'f' is the fundamental linear frequency; 't' is the time parameter.

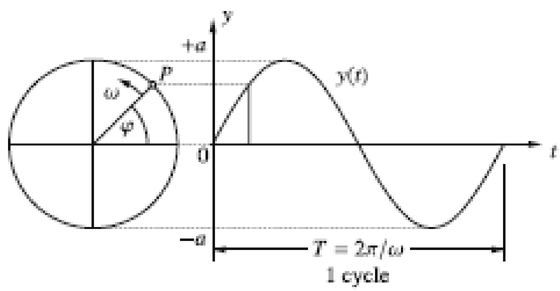

Figure 2-10 Electromagnetic wave propagation (Guochang Xu, 2007)

2.3.2. Carrier Frequency

In all navigation signals and timing processes, the fundamental frequency is f_o =10.23MHz, which is coherently derived from atomic frequency standards (AFS). The carrier frequencies for the GPS navigation signals are L1, L2 and L5 which are listed in table 2-1.

Link	Factor (xfo)	Frequency [MHz]	Wavelength [cm]	Allocated Band width(MHz)
L1	154	1575.42	19.0	24.0
L2	120	1227.60	24.4	24.0
L5	115	1176.45	25.5	24.0

Table 2-1 GPS frequency Band Table

The linear carrier phase combination between L1 and L5 will be especially useful for ionospheric-free combinations. The larger the frequency difference is advantageous to compute ionospheric corrections. It is also useful for ambiguity resolution in phase measurment (Guochang Xu, 2007).

2.3.3. PRN codes and modulation

The carriers are modulated by PRN codes and navigation messages. GPS applies the code division multiple access (CDMA) principle, as a result, the GPS satellites emit different PRN codes. The SV (Satellite Vehicle) numbers commonly coincide with the PRN number (SV01 = PRN01). GPS in its full operation capacity, it has been providing three ranging code signals modulated onto two carrier frequencies.

$$S_{L1}(t) = a_1 c_P(t) d(t) \cos(\omega_1 t) + a_2 c_{C/A}(t) d(t) \sin(\omega_1),$$

$$S_{L2}(t) = a_3 c_P(t) d(t)\, cos(\omega_2 t), \quad \ldots\ldots\ldots\ldots\ldots\ldots\ldots (2.14)$$

Where $c_P(t)$ denotes the precision code, here presented without any encryption signal, $c_{C/A}(t)$ is the Coarse/Acquisition code, and d(t) corresponds to the navigation data message NAV. The Factor $a_i = \sqrt{2P_i}$ represents the power of the signal components and ω_i is the circular frequency of the respective carrier. The C/A- code is modulated only onto the L1 carrier frequency, whereas the P-code is modulated on both the L1 and the L2 frequency. Thereby, the C/A-code is placed in phase quadrature to the P-code and carrier about 3 dB more power than the P-code. The C/A-code defines the standard positioning service (SPS) and the P-code the precise positioning service (PPS), which is classified (Guochang Xu, 2007).

2.3.4. Navigation Messages

The GPS signal is encoded with the ‘Navigation Message’, which can be read by the user’s GPS receiver. The Navigation Message includes orbit parameters (often called the ‘Broadcast Ephemeris’), from which the receiver can compute satellite coordinates (X, Y, Z); furthermore it contains information about the satellite health status, various correction data, messages, and other data messages.

The navigation message is updated and uploaded from the control stations to the SV in regular intervals. In nominal operation, new ephemerides data will be transmitted to the user at least every two hours, whereas the data is valid for three or four hours depending on the navigation message. The broadcast ephemerides for satellites with cesium clocks were accurate to about 5m and for Block II satellites, the accuracy is in the order of about 1m. The Almanac parameters are updated at least once every 6 days (Guochang Xu, 2007).

The algorithm which transforms the orbit parameters into WGS-84 satellite coordinates at any specified time is called the 'Ephemeris Algorithm'. For geodetic purposes, precise orbit information is available over the Internet from civilian organizations such as the IGS in the Earth-fixed reference frame (Guochang Xu, 2007).

2.3.5. Phase and Pseudorange Observations

High-precision geodetic measurements with GPS are performed using the carrier beat phase, the output from a single phase-tracking channel of a GPS receiver. This observable is the difference between the phase of the carrier wave implicit in the signal received from the satellite, and the phase of a local oscillator within the receiver. The phase can be measured with sufficient precision that the instrumental resolution is a millimeter or less in equivalent path length (Herring, et al., 2010).

In order to get the highest relative positioning accuracies, observation from several stations, for several satellite should be achieved at both L1 and L2 frequencies. The dominant source of error in a phase measurement or series of measurements between a single satellite and ground station is the unpredictable behavior of the time and frequency standards ("clocks") serving as reference for the transmitter and receiver. Even though the GPS satellites carry atomic frequency standards, the instability of these standards would still limit positioning to the several meter level were it not for the possibility of eliminating their effect through signal differencing (Herring, et al., 2010).

The pseudo-range GPS measurement, a second type, obtained using the 300-wavelength C/A ("coarse acquisition") code or 30-m-wavelength P ("protected") code transmitted by the satellites. Pseudo-ranges provide the primary GPS observation for navigation but are not precise enough to be used directly in geodetic surveys. They are useful, however, for estimating the offsets of receiver clocks, resolving ambiguities, and repairing cycle slips in phase observations (Herring, et al., 2010).

2.3.6. Differential GPS

Differential GPS (DGPS) is a means to get accurate position solution. By differencing there is a chance to remove the source of errors which affect the accuracy of the GPS measurement. (Herring, et al., 2010)

Single Differencing is differencing between a two ground station (Receivers) simultaneously looking at the same satellites eliminate the effect of bias or instabilities in the satellite clock. This measurement is commonly called the between-stations difference, or single-difference observable. If the stations are closely spaced, differencing between stations also reduces the effects of tropospheric and ionospheric refraction on the propagation of the radio signals. If the ground stations have hydrogen maser oscillators (with stabilities approaching 1 part in 1015 over several hours), then single differences can, in principle, be useful. In practice, however, it is seldom cost effective to use hydrogen masers and single difference observations in GPS surveys. Rather, we form a double difference (Herring, et al., 2010).

Double difference is differencing the between-station differences also between satellites to cancel completely the effects of variations in the station clocks. In this case the observations are just as accurate with low-cost crystal oscillators as with an atomic frequency standard. Since the phase biases of the satellite and receiver oscillators at the initial epoch are eliminated in doubly differenced observations, the doubly differenced range (in phase units) is the measured phase plus an *integer* number of cycles (Herring, et al., 2010).

If the measurement errors, arising from errors in the models for the orbits and propagation medium as well as receiver noise, are small compared to a cycle, there is the possibility of determining the integer values of the biases, thereby obtaining from the initially ambiguous doubly differenced phase an unambiguous measure of doubly differenced range. Resolution of the phase ambiguities improves the uncertainties in relative position measures by about a factor of 1.5 for 24-hr sessions, 3 for 8-hr sessions and more than 5 for short sessions (Herring, et al., 2010).

GAMIT, which will be briefly discussed in section 3.4, incorporates difference-operator algorithms that map the carrier beat phases into singly and doubly differenced phases. These algorithms extract the maximum relative positioning information from the phase data regardless of the number of data outages, and take into account the correlations that are introduced in the differencing process (Herring, et al., 2010).

In order to provide the maximum sensitivity to geometric parameters, the carrier phase must be tracked continuously throughout an observing session. If there is an interruption of the signal, causing a loss of lock in the receiver, the phase will exhibit a discontinuity of an integer number of cycles ("cycle-slip"). This discontinuity may be only a few cycles due to a low signal-to-noise ratio, or it may be thousands of cycles, as can occur when the satellite is obstructed at the receiver site (Herring, et al., 2010).

Initial processing of phase data is often performed using time differences of doubly differenced phase ("triple differences", or "Doppler" observations) in order to obtain a preliminary estimate of station or orbital parameters in the presence of cycle slips. The GAMIT software uses triple differences in editing but not in parameter estimation. Rather, it allows estimation of extra bias parameters whenever the automatic editor has flagged an epoch as a cycle slip that cannot be repaired (Herring, et al., 2010).

Although phase variations of the satellite and receiver oscillators effectively cancel in doubly differenced observations, errors in the *time* of the observations, as recorded by the receiver clocks, do not. However, the pseudo-range measurements, together with reasonable a priori knowledge of the station coordinates and satellite position, can be used to determine the offset of the station clock to within a microsecond, adequate to keep errors in the doubly differenced phase observations below 1 mm (Herring, et al., 2010).

Having saying the above to remove the clock bias both for Satellite and Receiver, cycle slip detection and time, the other source of errors like ionospheric, tropospheric and multipathing will be solved with linear combination of frequencies and with the models (Herring, et al., 2010).

A major source of error in single-frequency GPS measurement is the variable delay introduced by the ionosphere. For day-time observations near solar maximum this effect can exceed several parts per million of the baseline length. Fortunately, the ionospheric delay is dispersive and can usually be reduced to a millimeter or less by forming a particular linear combination (LC, sometimes called L3) of the L1 and L2 phase measurements:

$$\emptyset_{LC} = \frac{f_1^2}{f_1^2 - f_2^2}\emptyset_{L1} - \frac{f_1 f_2}{f_1^2 - f_2^2}\emptyset_{L2} \ldots\ldots\ldots\ldots\ldots\ldots\ldots \quad (2.15)$$

$$\emptyset_{LC} = 2.546\emptyset_{L1} - 1.984\emptyset_{L2} \ldots\ldots\ldots\ldots\ldots\ldots\ldots (2.16)$$

Forming LC, however, magnifies the effect of other error sources. For baselines less than a few kilometers the ionospheric errors largely cancel, and it is preferable to treat L1 and L2 as two independent observables rather than form the linear combination. The station separation at which the ionspheric errors exceed the phase noise depends on many factors (receiver, antenna, multipath environment, latitude, time of day, sunspot activity) and must be determined empirically by analyzing the data with both observable types (Herring, et al., 2010).

Another useful combination is the difference between L2 and L1 with both expressed in distance units:

$$\emptyset_{LG} = \emptyset_{L2} - \frac{f_2}{f_1}\emptyset_{L1} \ldots\ldots\ldots\ldots\ldots\ldots\ldots\ldots (2.17)$$

$$\emptyset_{LG} = \emptyset_{L2} - 0.779\emptyset_{L1} \ldots\ldots\ldots\ldots\ldots\ldots\ldots\ldots (2.18)$$

called "LG" because the L2 phase is scaled by the "gear" ratio (f_2/f_1 =60/70=1227.6/1575.42). In the LG phase all geometrical and other non-dispersive delays (eg., the troposphere) cancel, so that we have a direct measure of the ionospheric variations (Herring, et al., 2010).

If precise(P-code) pseudorange is available for both GPS frequencies, then a "wide-lane" (WL) combination of L1,L2,P1,and P2 can be formed which is free of both ionospheric and geometric effects and is simply the difference in the integer ambiguities for L1 and L2:

$$WL = n_2 - n_2 = \emptyset_{L2} - \emptyset_{L1} + (P1 - P2)\frac{(f1 - f2)}{(f1 + f2)}) \ldots\ldots\ldots (2.19)$$

The WL observable can be used to fix cycle slips in one-way data but should be combined with LG and doubly differenced LC to rule out slips of an equal number of cycles at L1 and L2 (Herring, et al., 2010).

These various combinations of phase and pseudorange observations are used not only in data editing, but also in resolving the phase ambiguities. When the LC observable is used, we determine the L1 and L2 ambiguities by first resolving n_2 - n_1 ("widelane") and then n_1 ("narrow lane"). If precise and unbiased pseudoranges are available, the widelane ambiguities can be resolved for baselines up to thousands of kilometers under any ionosphere conditions (Herring, et al., 2010).

GAMIT gives you the option of selecting the method to be used, either pseudoranges (LC_AUTCLN) or ionospheric constraints (LC_HELP). Once the wide-lane ambiguity for given doubly differenced combination has been resolved, resolving the narrow-lane ambiguity for that combination depends on the level of noise from the receiver, multipathing, and the troposphere, and the accuracy of the models employed for the position and motion of the stations and satellites. It is generally more difficult to resolve these ambiguities for the longest baselines, but for data acquired since 2000 we can usually resolve 80-95% of the ambiguities in a global analysis (Herring, et al., 2010).The details are well explained in GAMIT Manuals (Herring, et al., 2010).

2.5. Factors Affecting GPS measurements

GPS signal is an electromagnetic wave which uses both code and phase measurements. A code measurement is not affected by the media that the signal passes and unambiguous but it is noisy having its own limitation in accuracy. Phase measurement, though, it is ambiguous due to unknown integer multiple of the fundamental frequency, it is more accurate than code measurements. In addition, phase measurement affected by the media that is passing through and characteristics of a noise from electronics in receiver and transmitter as well as clock bias and clock error of both, it is more accurate (Guochang Xu, 2007).

It is worth noting knowing factors which affect the electromagnetic signal that the GPS uses and tries to remove the contribution in the measurement by modeling or removing by some mathematical methods like differential measurement and using more satellite. Bellow, main focus will be, to discuss the effect as well as methods and models to remove factors that affect the GPS measurement. The factors contribute for the GPS measurement generally can be summarized as follows:

$$P_{rec}^{sat} = \rho_{rec}^{sat} + c.(dt_{rec} - dt^{sat}) + rel_{rec}^{sat} + Trop_{rec}^{sat} + Ion_{rec}^{sat} + K_{rec} + K^{sat} + def_{rec}^{sat} + \varepsilon \quad (2.20)$$

Where P_{rec}^{sat} is actual or true range , ρ_{rec}^{sat} is pseudorange, $c.(dt_{rec} - dt^{sat})$ is clock error in satellite and receiver, rel_{rec}^{sat} relativistic effect, $Trop_{rec}^{sat}$ is tropospheric effect , Ion_{rec}^{sat} ionospheric effect $K_{rec} + K^{sat}$ istrumentation(electronics) in both receiver and satellite and def_{rec}^{sat} is deformation(movement of an area thought time) which this work is targeted on and ε is un modeled source of errors such as white noise, computational error etc.

I will start with satellite and receiver clock errors, then Ionospheric and tropospheric delays. Further, multipath and relativistic effects also will be discussed in brief. Readers who need a more detail explanation may refer to sources which are mentioned in references (Guochang Xu, 2007).

2.5.1.Clock Errors

The clocks on the satellites and receivers play a very important role in precise GPS surveying. As a result of the factor c, a small clock error may cause a very large code and phase error. For code measurements, a clock error of δt will cause a path length error of $c\delta t$. Similarly, for phase measurements, a clock error of δt will cause a phase error of ${}^{c\delta t}/_{\lambda}$. Another is factorized with the speed of satellites. And the third is factorized with the working frequency. Therefore, high quality clocks have to be used on the satellites and receivers. Meanwhile, clock errors must be carefully modeled. Generally, a simple polynomial model can be expressed as:

$$\delta t = a_0 + a_1(t_e - t_c) + a_2(t_e - t_c)^2 \ldots\ldots\ldots\ldots\ldots\ldots\ldots \textit{(2.21)}$$

Where, a_0 =satellite clock offset $a_{1=}$ satellite clock drift coefficient

$a_{2=}$ satellite clock frequency drift coefficient, $t_{c=}$ satellite clock reference epoch

$t_{e=}$ Ephemerides reference epoch

The coefficients are listed in the RINEX file of the GPS receiver file that one downloads.

2.5.2.Ionospheric Effect

One of the atmospheric layers which the GPS signal passes through is ionosphere. It extends in various layers from about 50km to 1000km above the earth. This layer is a dispersive medium with respect to the GNSS radio signal. Thus, the ionospheric effect is an important error source in GPS measurement. The ionopsheric delay (for code measurements) or advance (for phase measurements) of the GPS signal can vary from a few meters to more than twenty meters within a day. Generally, it is difficult to model the ionopheric effect due to complicated physical interactions among the geomagnetic field and solar activities (Hofmann-Wellenhof, et al., 2008).

2.5.3.Tropospheric Effect

The lower part of the earth's atmosphere is composed of dry gases and water vapor, which lengthen the propagation path due to refraction. The magnitude of the resulting signal delay depends on the refractive index of the air along the propagation path and typically varies from about 2.5 m in the zenith direction to 10-15 m at low satellite elevation angles. The troposphere is non-dispersive at the GPS frequencies, so that delay is not frequency dependent. In contrast to the ionosphere, tropospheric path delay is consequently the same for code and carrier signal components. Therefore, this delay cannot be measured by utilizing both L1 and L2 pseudorange measurements, and either models and/or differential positioning must be used to reduce the error. The refractive index of the troposphere consists of that due to the dry-gas component and the water vapor component, which respectively contribute about 90% and 10% of the total (Guochang Xu, 2007).

There are models to estimate the tropospheric delay and mapping functions to map the vertical tropospheric delay to slant tropospheric delay of the GPS signals. Among these models, Hopfield, Modified Hopfield and Saastamoinen Model and among the mapping functions Vena Mapping Function (VMF) and the modified version (VMF1) are commonly used. The details of the models can be found in Hofmann Book (Hofmann-Wellenhof, et al., 2008) (Guochang Xu, 2007). The Saastamoinen models and VMF1 Mapping functions are used to remove the tropospheric effect in GAMIT analysis (Herring, et al., 2010).

2.5.4.Multipath Effect

Multipath effect can be described as a satellite-emitted signal arrives at the receiver by more than one path (figure 2-11). Multipath is mainly caused by reflecting surfaces near the receiver and to some extent reflection at the satellite during signal transmission.There is no general model of the multipath effect because of the time- and location-dependent geometric situation. The influence of the multipath, however, can be estimated by using a combination of f_1 and f_2 code and carrier phase measurements. The principle is based on the fact that the troposphere, clock errors, and relativistic effects influence code and carrier phases by the same amount. Purely from geometry it is clear that signals received from low satellite elevations are more susceptible to multipath than signals from high elevations. The details are listed in (Hofmann-Wellenhof, et al., 2008).

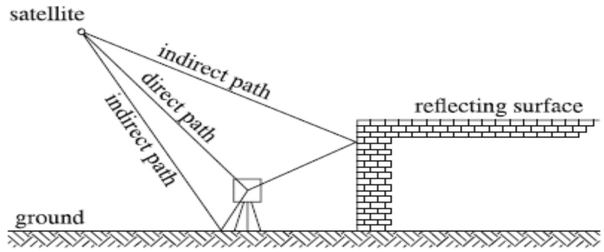

Figure 2-11 Multipath effect (Hofmann-Wellenhof, et al., 2008)

2.5.5. Relativistic Effect

This effect can be explained in terms of the general and special theory relativity of Einstein. This effect is related to coordinate systems and the frequency of the GPS signal.

In most GPS computation and analysis this effect generally is not considered. However, the effect can be explained in terms of frequency, path range, Earth's rotation, orbit eccentricity and satellite acceleration (Guochang Xu, 2007).

2.5.6. Earth Tide and Ocean Loading

2.5.6.1. Earth Tide

The Earth tide is a phenomenon of the deformation of the elastic body of the Earth caused by the gravitational attracting force of the Moon and the Sun. Such a deformation depends not only on the changing of the force, but also on the physical structure and motion of the Earth. The Earth tide effects could reach up to 60 cm world-wide. The tidal parameters can be also determined through global GPS observations. The IERS standards are used as the principle of the Earth tide effect computation (Guochang Xu, 2007).

2.5.6.2 Ocean Loading

The ocean tide is a time varying load on the Earth's surface. The displacement of the Earth's surface due to loading is called the ocean tide loading effect. Computation of the loading displacement depends on which ocean tide model is used. Loading tide effects could reach up to 10 cm at some special coast regions.

2.3.7. Antenna Phase Center Offset

Antenna phase center offset is also one factor that affects GPS measurement. Both Satellite and Receiver Antenna effect should be considered.

2.3.7.1. Satellite Antenna Phase Center Correction

The geometric distance between the satellite (at signal emission time) and the receiver (at signal reception time) is in fact the distance of the phase centers of the two antennas. However, the orbit data, which describes the position of the satellite, is usually referred to the mass center of the satellite. Therefore, a phase center correction (also called mass center correction) has to be applied to the satellite coordinates in precise applications.

2.3.7.2. Receiver Antenna Phase Center Correction

In the case of receiver antenna phase center correction, the dependence of the phase center on the signal direction and frequencies has to be taken into account. Both the phase center offset and variation should be modeled. Generally, the phase center corrections can be obtained through careful calibration. Receiver antenna phase center offset is also antenna type dependent (Guochang Xu, 2007). For a GPS network, antenna phase center corrections are usually predetermined and listed in a table for use. In case of GAMIT software processing antenna phase center corrections are listed in file called “antmod.dat” (Herring, et al., 2010).

2.3.8. Instrumental Biases

The biases are systematic errors, which are different from the frequency-to-frequency and from the code to phase measurements. However, they are constants for given frequency and given observable type as well as given instruments (receiver or GPS satellite).

The separation of the instrumental biases and the ambiguities are possible because the biases of the receiver and satellite are independent from each other, whereas the ambiguity parameters are dependent both on the receiver and the satellite. However, by modeling and solving the problem, the correlation between the parameters has to be carefully studied (Guochang Xu, 2007).

Chapter Three

3. GPS Data Sources and Processing

3.1. Introduction

In this section the data from the IGS stations that are used in the GPS data processing and data emanation from the local stations with in the study area will be discussed. The GPS data used for the analysis is from 2007 to early 2012.

3.2. IGS sites

There are over 350 continuously operating dual-frequency GNSS stations, which provide high-quality data in near real time. These data sets are used by the IGS to generate several data products (such as: satellite ephemerides, Earth rotation parameters, tracking coordinates and velocities, clock information of IGS tracking station and satellites, and etc) which is available via the internet. From this 350 stations, the IGS station used in this study(Figure 3-1) are ADIS, MAL2, MBAR, MAS1, NAMA, NKLG, BHR1, BHR2, SEY1, RAMO, ZAMB, CGGN, SOLA, WTZR, and YIBL.

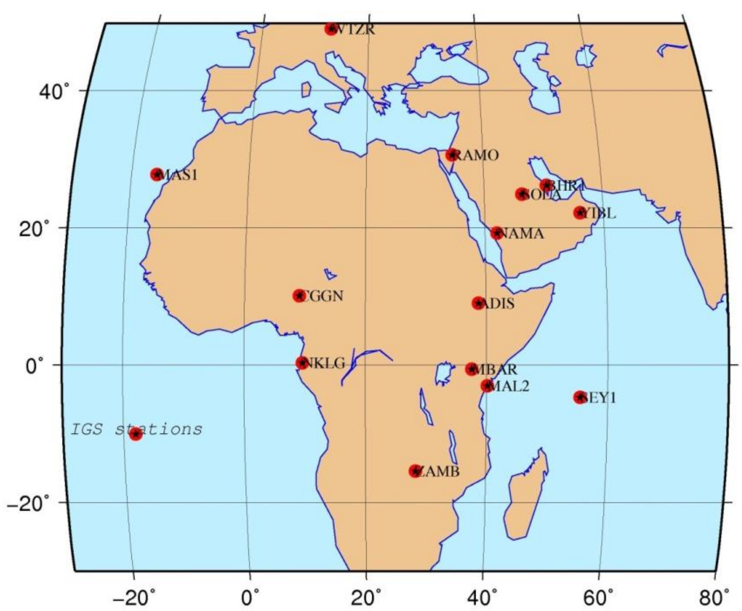

Figure 3-1 IGS stations used in GPS processing

3.3. Local GPS stations

The local stations used in this study are the Continuously Operating Reference Stations (CORS) that are located in Semera and the one at Saha (figure 3-2), with 4 character IDs DASM and DASA respectively. For DASM data is available from 2007 to 2012 and for DASA from early 2008 to the end of 2009. The data is downloaded form the Server of the Institute of Geophysics, Space Science and Astronomy (IGSSA) of Addis Ababa University. It is also available in UNAVCO's homepage.

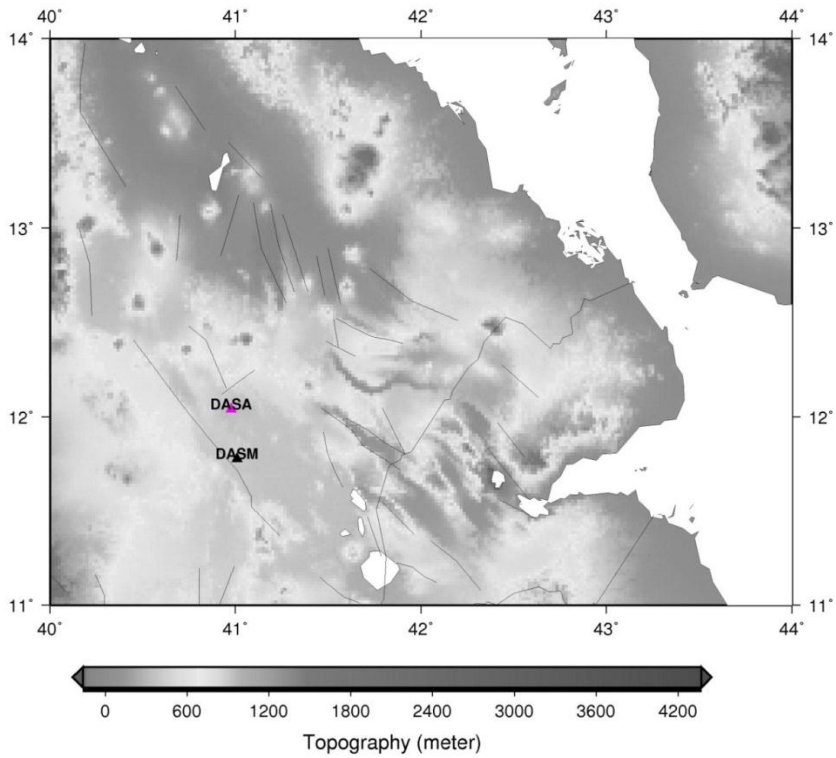

Figure 3-2 Local GPS stations used (DASA campaign and DASM continuous stations)

3.4. Data processing using GAMIT/GLOBK

The GPS processing is done using the GAMIT/GLOBK software from the Massachusetts Institute of Technology (MIT) which is a free scientific software with a license agreement. This software is primarily made available for high level of scientific researches.

The general data analysis procedure is summarized in figure 3.3.

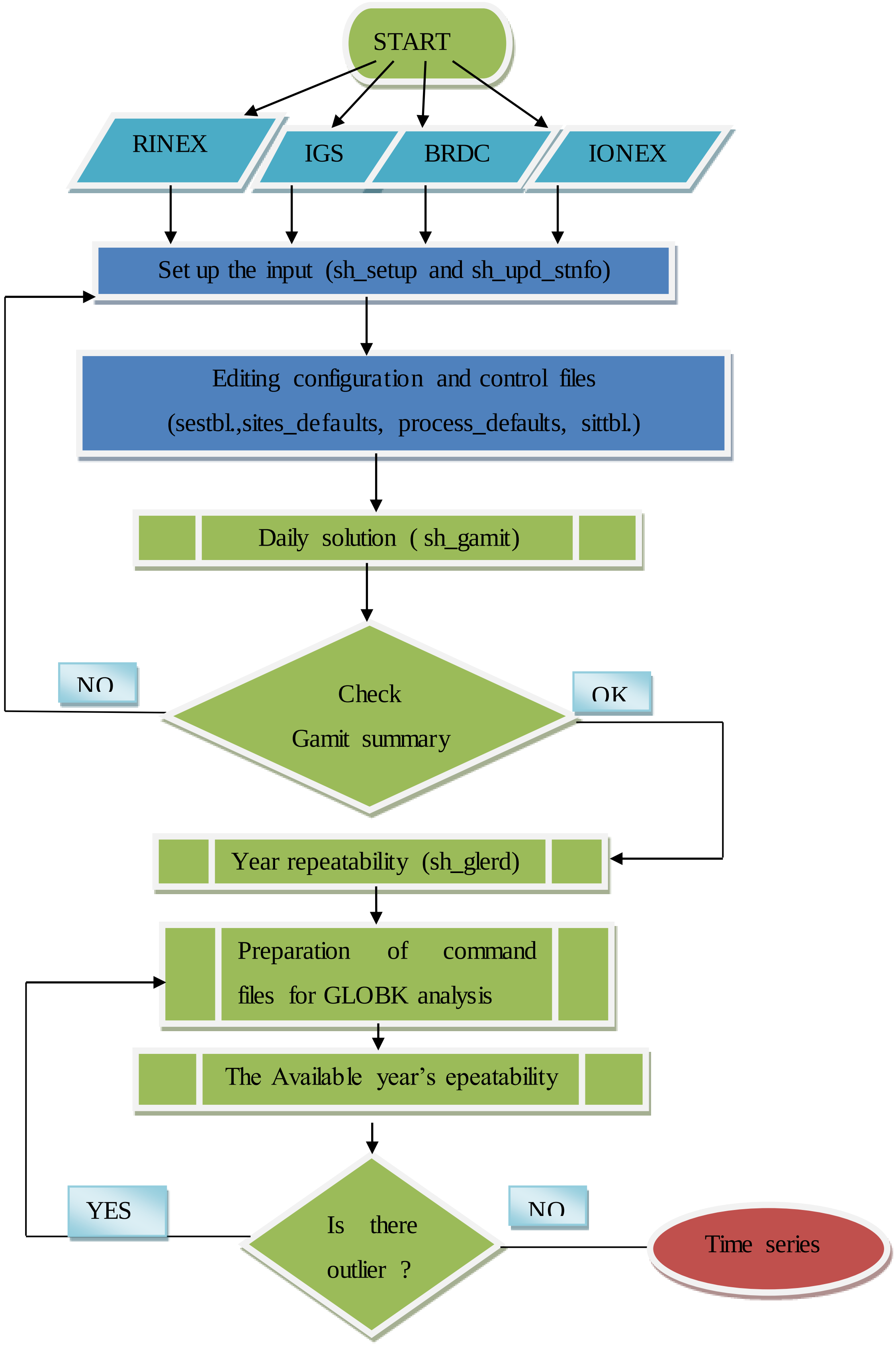

Figure 3-3 Flow chart of GPS data processing scheme.

Chapter Four

4. GPS Result and Discussion

4.1. GPS Result

Both, DASM and DASA time series showed (Figure 4-1 and Figure 4-2) that the east and the north component are moving toward east and north direction respectively following the global absolute motion direction. The deformation speed has changed slightly for DASM since mid of 2008. The up direction time series follows the normal trend from 2007 up to mid 2008. The reversal in the direction of the up coordinate propagation is observed just after the mid 2008 up to the available data early 2012. The time series of both station have been plotted separately due to an unavailability of equal span of time series data (see, figures 4-1 and 4-2). The red line in figures 4-1 and 4-2 indicates the time (mid of 2008) at which the subsidence started to occur in the study area.

The velocities of DASM in an absolute sense in the North, East and Up are 48.5 $\pm$0.2mm/yr, 39.5 $\pm$0.2mm/yr and -9.2 $\pm$0.7mm/yr respectively. The errors associated with the corresponding coordinate time-series measurements of DASM are $\pm$4.7mm, $\pm$4.6mm and $\pm$7.9mm respectively. The velocities of DASA in an absolute sense in the North, East and Up directions are 27.8 $\pm$0.4mm/yr, 43.9 $\pm$0.5mm/yr and -21.5$\pm$1.4mm/yr respectively. The errors associated with the corresponding coordinate time-series measurements of DASA are $\pm$1.6mm, $\pm$2.4mm and $\pm$5.0mm respectively.

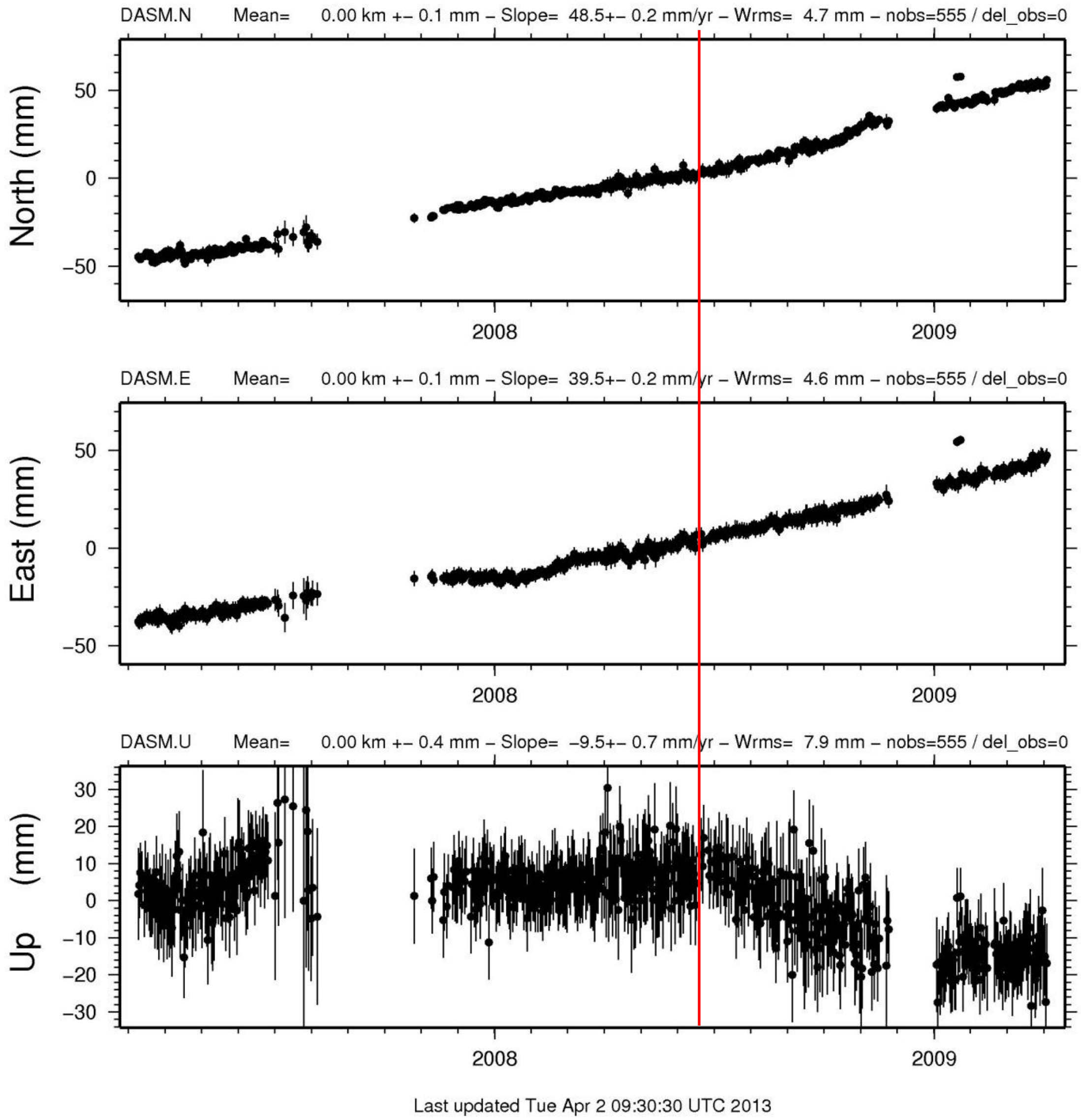

Figure 4-1 DASM timeseries (The vertical Red line shows when the subsidence is starting)

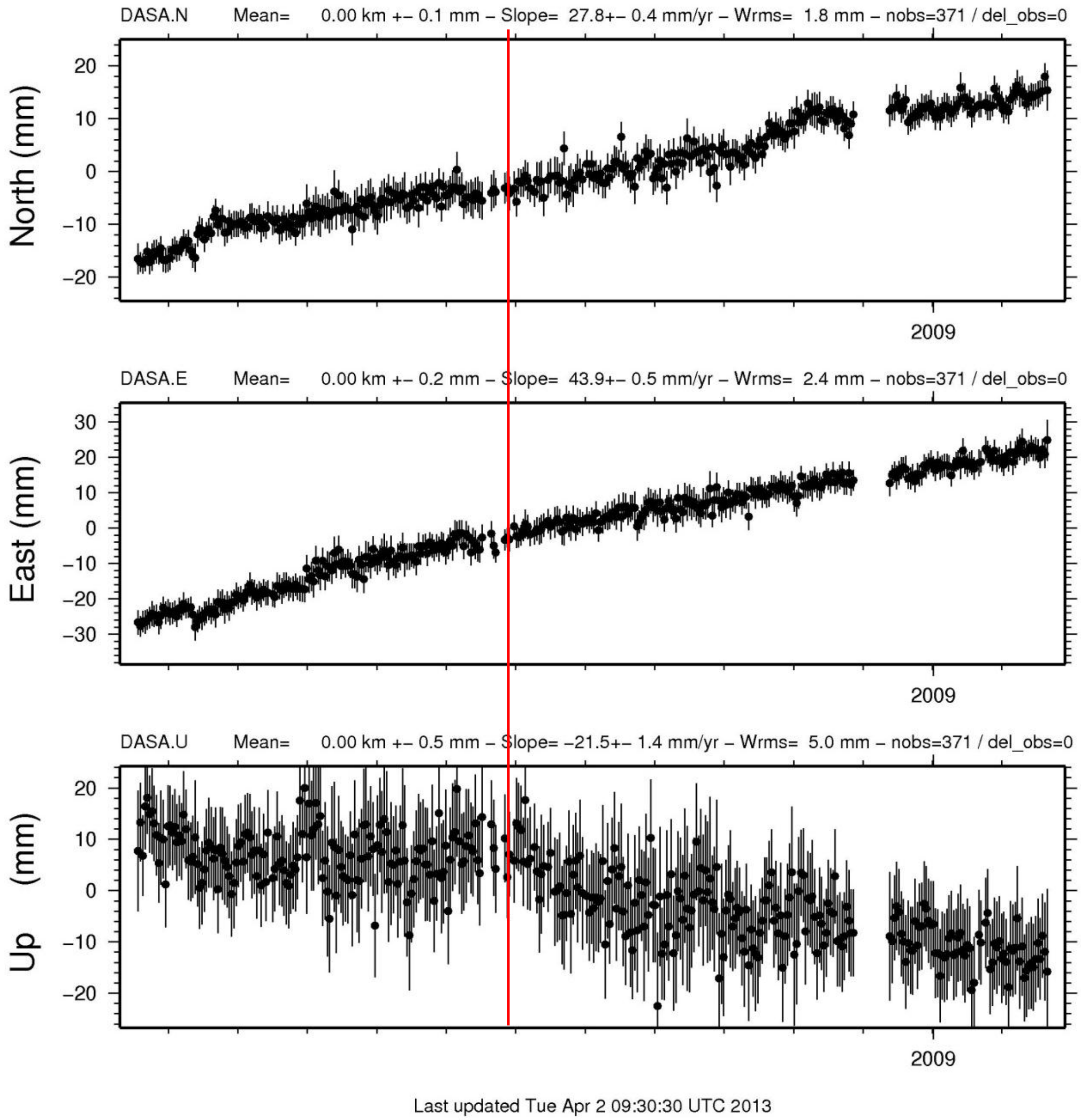

Figure 4-2 DASA timeseries (The vertical Red line shows the start of the subsidence)

4.2. Discussion

The data from the continuously operated DASM and DASA GPS stations, where currently DASA is not functional, are plotted with the same temporal window to a better analysis. However, the DASM has pretty much continuous data up to 2012.

The time series that is derived from GAMIT/GLOBK analysis software shows the daily solution in terms of the local coordinate system which is topocentric in the North, East and Up directions. Generally, from the time series plot one can clearly see how the station is behaving in terms of the movement in the three dimensions. The axes are oriented in such a way that east is pointing toward the positive y direction, north toward the positive x direction and up toward the positive z direction. If negative, the movement is toward the opposite directions. For the up direction positive means inflation and negative means deflation.

From the GAMIT/GLOBK output, the East component of the station DASA shows positive slope. This positive slope shows that the East component is moving toward the East direction with 43.9 $\pm$0.5 mm/yr. The North component is also with positive slope. This signifies that the North component is moving toward the North direction following the regional trend with 27.8 $\pm$0.4 mm/yr. However, the Up component's has negative slope -21.8 $\pm$ 1.4mm/yr. This shows that the Up component is moving in the opposite direction of the general plate's movement (absolute movement (Kearey, et al., 2009), (unavco.org)). Similarly DASM station moves 39.5 $\pm$0.2 mm/yr in the East, 48.5 $\pm$0.2 mm/yr in the North and -9.5 $\pm$0.7 mm/yr in up direction.

An independent regression analysis carried out in this work showed that (figure 4-3), the slope of the East component of DASA is 44 mm/yr and North is 28 mm/yr, which is close to the result from the GAMIT output. However, the Up component shows a change in slope with two different characteristics. It has a gentle slope of -10 mm/yr, from the first date to doy 146 of 2008 and a rougher slope that amount to -29 mm/yr from doy 147, 2008 up to the end of the data series in 2009. Unfortunately, the data from DASA is no more available after 2009.

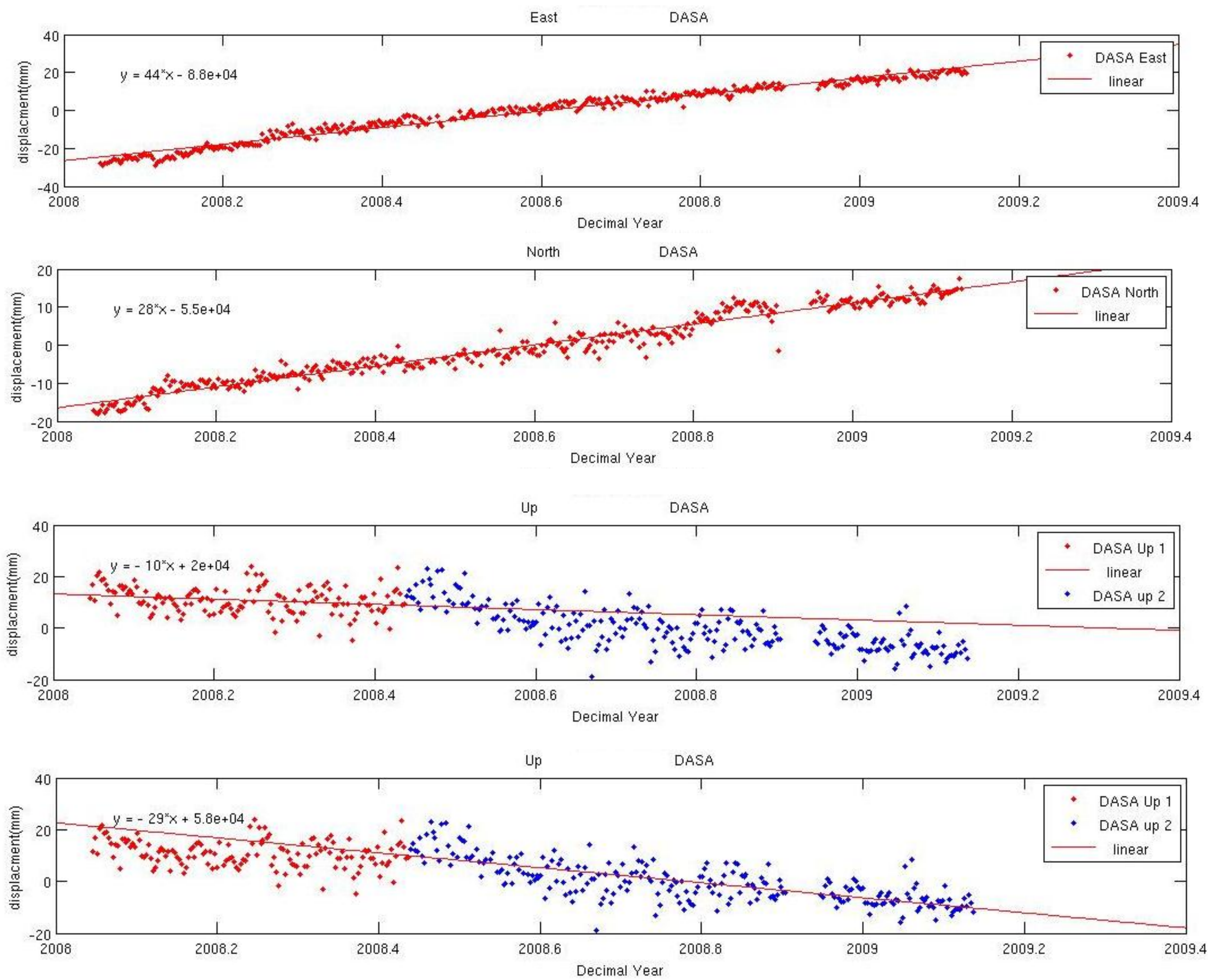

Figure 4-3 DASA GPS linear fit (doy 17, 2008 - 50, 2009)

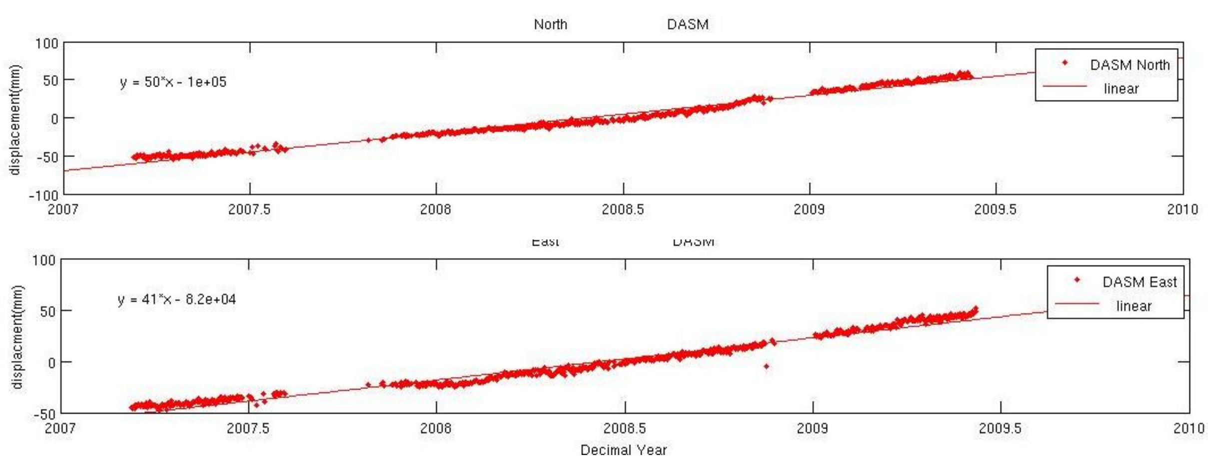

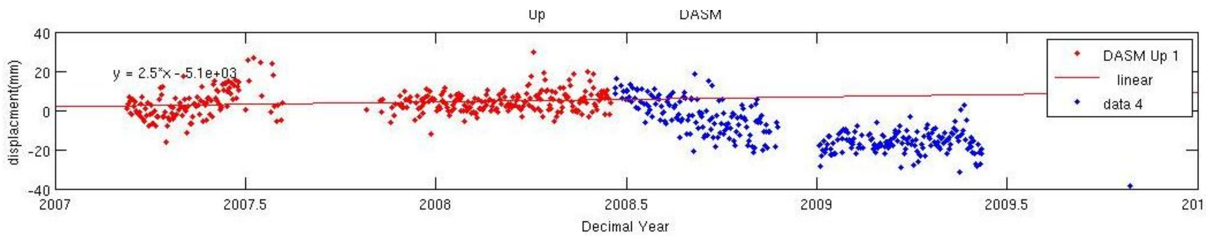

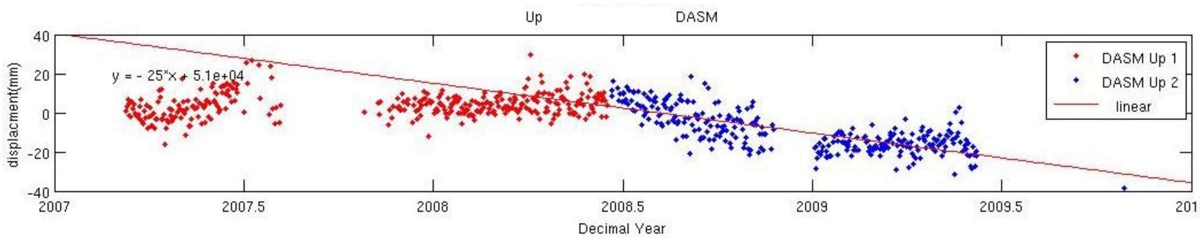

Figure 4-4 DASM GPS linear fit (doy 69, 2007 - 301, 2009)

Similarly, the DASM GPS station shows (figure 4-4) that the East component moves eastward with a velocity of 50 mm/yr and the North component moves northward with a velocity of of 41 mm/yr. similar to the deformation patterns of the DASA station, along the local vertical, the Up component of the DASM station have a change in slope around end of May, 2008. It shows nearly constant velocity that amounts to 2.5 mm/yr from early 2007 to doy 150 in 2008. However, from doy 151 in 2008 up to the end of data series in 2009 there is a faster velocity that amount to -25mm/yr, which signify a faster subsidence detected by DASA.

Thus, from the two stations it can be clearly seen that there is a subsidence in the region.

Chapter five

Method II

5. Interferometric Synthetic Aperture Radar

5.1. Introduction

Radar is an active sensor that provides its own illumination; and owing to their longer wavelength, radar signals penetrate water clouds, diffused ash clouds, and sparse to moderate vegetation better than visible light. Because radar is an active microwave system, it is equally effective in darkness and daylight, and during bad or good weather. Therefore, it is an all weather monitoring system which is similar to GPS. This makes the method to be one of the preferable methods in volcano monitoring, deformation study and in many other applications (Dzurisin, et al., 2007).

Synthetic Aperture Radar (SAR) is a coherent active microwave imaging sensor. Backscattered information of a target is recorded as a 2-D complex signal with amplitude and phase information from which SAR complex valued image with amplitude and phase is extracted. Interferometric SAR (In-SAR) technique makes use of phase difference information extracted from two complex valued SAR images acquired from different orbit positions. This information is useful in measuring a range of geodetic and geophysical quantities, naturally occurring, such as topography, slope, deformation (volcanoes, earthquakes, landslide, and ice fields), and man-made (aquifer recharge, geothermal fields, oil/mining subsidence etc.) (Lazarov, 2010).

The power of radar interferometry for geodesy stems from its high-resolution images that are generated from a controlled coherent light source. The coherence of the measurements ensures that the phase associated with each complex image element contains both the round-trip geometric path length from the radar sensor to the surface and back, and the ensemble phase associated with the coherent summation of scattering within the image element (Simons, et al., 2007).

InSAR raw image data are collected by transmitting a series of coded pulses from an antenna illuminating a swath offset from the flight track. The echo of each pulse is recorded during a period of reception between the transmission events. When a number of pulses are collected, it is possible to perform 2-D matched-filter compression on a collection of pulse echoes to focus the image. This technique is known as SAR because in the along-track, or azimuth direction, a large virtual aperture is formed by coherently combining the collection of radar pulses received as the radar antenna moves along in its flight path (Raney, 1971). Although the typical physical length of a SAR antenna is on the order of meters, the synthesized aperture length can be on the order of kilometers. Because the image is acquired from a side-looking vantage point (to avoid left-side/right-side ambiguities), the radar image is geometrically distorted relative to the ground coordinates (Simons, et al., 2007).

There are different satellites launched at different times by different Space Agencies and countries. The table in Appendix E summarizes most of the available SAR satellites and their characteristics.

Through out this thesis, Envisat satellite and its product Advanced Synthetic Aperture radar (ASAR) will be dealt. However, the general principle holds true for other satellites too. The reason I select the Envisat is because the data is available and easy to get with out charge.

5.2. Envisat

Envisat (Environmental Satellite) is owned by European Space Agency (ESA). It is launched in 2002 and the largest Earth Observation space craft ever built. It carries 10 sophisticated optical and radar instruments to provide continuous observation and monitoring of the Earth’s land, atmosphere, oceans and ice caps. Envisat data provide a wealth of information on the workings of the Earth system. Envisat’s largest single instrument is the Advanced Synthetic Aperture Radar (ASAR), operating at C-band. This ensures continuity of data after ERS-2, despite a small (31MHz) central frequency shift. It features enhanced capability in terms of coverage, range of incidence angles, polarisation, and modes of operation. The improvements allow radar beam elevation steerage and the selection of different swaths, 100 or 400 km wide. Envisat is in a 98.54° sun-synchronous circular orbit at 800 km altitude, with a 35-day repeat and the same ground track as ERS-2 (ESA, 2012).

Unfortunately, ESA declares end of mission for Envisat on 9 May 2012. ESA Press release said "Just weeks after celebrating its tenth year in orbit, communication with the Envisat satellite was suddenly lost on 8 April. Following rigorous attempts to re-establish contact and the investigation of failure scenarios, the end of the mission is being declared." (ESA, 2012). In the next sub-sections, the working principle and the mathematics behind image (interferogram) formation will be described briefly.

5.3. Types of Radar Interferometry

Radar interferometry can be divided based on geometric configuration of the baseline vector, as Cross-Track and Along-Track interferometry. Moreover, it can also be divided based on how the image is acquired as Strip mode, ScanSAR mode and Spotlight Mode.

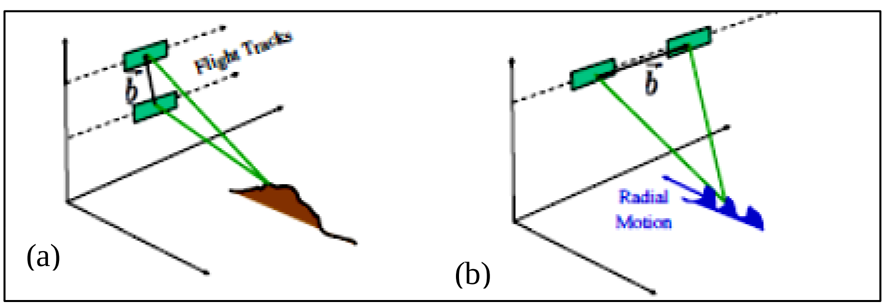

Figure 5-1(a) Cross-Track Interferometer, (b) Along-Track Interferometer

The scope of this thesis is only Strip Mode imaging system. One can get the detail from (Alessandro, et al., 2007).

5.3.1. Strip Mode Imaging System

A SAR imaging system from a satellite (such as ERS or Envisat) is sketched in Figure 5-2(a) and (b). A satellite carries radar with the antenna pointed to the Earth's surface in the plane perpendicular to the orbit (in practice this is not strictly true, because it is necessary to compensate for the Earth's rotation). The inclination of the antenna with respect to the nadir is called the off-nadir angle and in contemporary systems is usually in the range between 20° and 50° (it is 21° for Envisat). Due to the curvature of the Earth's surface, the incidence angle of the radiation on a flat horizontal terrain is larger than the off-nadir (typically 23° for Envisat) (Alessandro, et al., 2007). However, for the sake of simplicity it is assumed that the Earth is flat, and hence that the incidence angle is equal to the off-nadir angle, as shown in the figure.

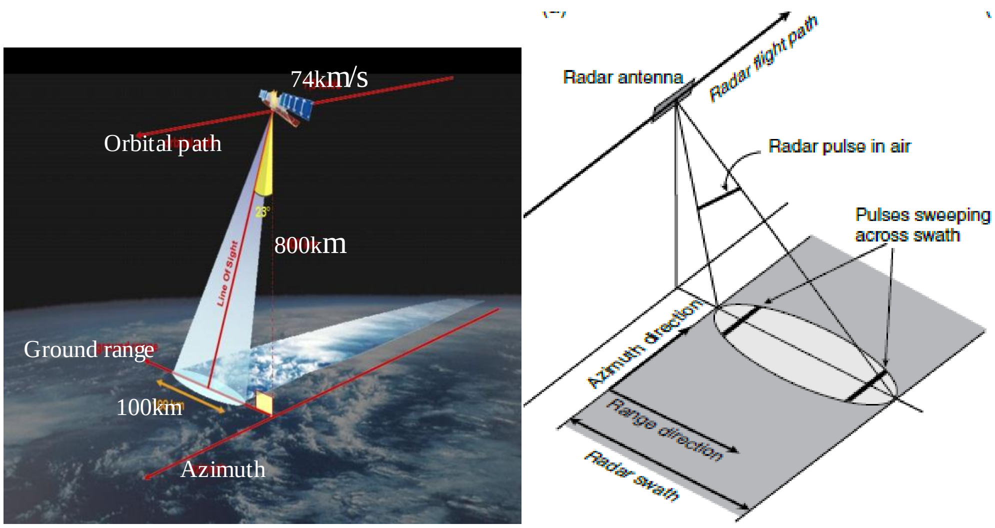

(a) (b)

Figure 5-2(a) Strip Mode SAR System (www.treuropa.com, 2012)(b) Strip mode configuration

In the case of Envisat, the illuminated area on the ground (the antenna footprint) is about 5 km in the along-track direction (also called the azimuth direction) and about 100 km in the across-track direction (also called the ground range direction). The direction along the Line of Sight (LOS) is usually called the slant-range direction (Alessandro, et al., 2007).

5.4. Complex SAR Image

A digital SAR image can be seen as a mosaic (i.e. a two-dimensional array formed by columns and rows) of small picture elements (pixels). Each pixel is associated with a small area of the Earth's surface (called a resolution cell). Each pixel gives a complex number that carries amplitude and phase information about the microwave field backscattered by all the scatterers (rocks, vegetation, buildings etc.) within the corresponding resolution cell projected on the ground. Different rows of the image are associated with different azimuth locations, whereas different columns indicate different slant range locations (Alessandro, et al., 2007).

The radiation transmitted from the radar has to reach the scatterers on the ground and then come back to the radar in order to form the SAR image (two-way travel).Thus, detected SAR image contains a measurement of both the phase and amplitude of the radiation backscattered toward the radar by the objects (scatterers) contained in each SAR resolution cell. The amplitude depends more on the roughness than on the chemical composition of the scatterers on the terrain. Typically, exposed rocks and urban areas show strong amplitudes, whereas smooth flat surfaces (like quiet water basins) show low amplitudes, since the radiation is mainly mirrored away from the radar (Alessandro, et al., 2007).

Scatterers at different distances from the radar (different slant ranges) introduce different delays between transmission and reception of the radiation. Due to the almost purely sinusoidal nature of the transmitted signal, this delay τ is equivalent to a phase change φ between transmitted and received signals. The phase change is thus proportional to the two-way travel distance $2R$ of the radiation divided by the transmitted wavelength λ. This concept is illustrated in figure below:

$$\varphi = \frac{2\pi}{\lambda} 2R = \frac{4\pi}{\lambda} R \quad \text{……………………………………………(5.1)}$$

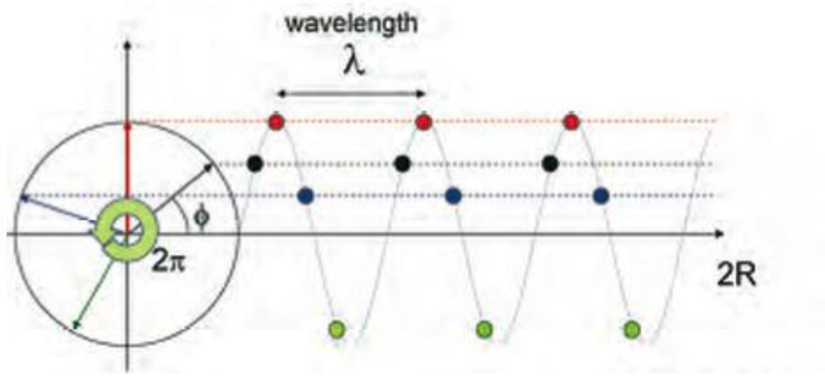

Phase Sinusoidal signal two-way distance

Figure 5-3A sinusoidal function sin φ is periodic with a 2π radian period. In the case of a relative narrow-band SAR (i.e. Envisat), the transmitted signal can be assimilated, as a first approximation, to a pure sinusoid whose angle or phase φ has the following linear dependence on the slant range coordinate r: $\phi = 2\pi r / \lambda$ (where λ is the SAR wavelength). Thus, assuming that the phase of the transmitted signal is zero, the received signal that covers the distance 2R travelling from the satellite to the target and back, shows a phase $\phi = 4\pi R/\lambda$ radians (Alessandro, et al., 2007).

However, due to the periodic nature of the signal, travel distances that differ by an integer multiple of the wavelength introduce exactly the same phase change. In other words the phase of the SAR signal is a measure of just the last fraction of the two-way travel distance that is smaller than the transmitted wavelength. In practice, due to the huge ratio between the resolution cell dimension (of the order of a few meters) and wavelength (~5.6 cm for Envisat), the phase change passing from one pixel to another within a single SAR image looks random and is of no practical utility (Alessandro, et al., 2007).

5.5. SAR Resolution and Topography

The terrain area imaged in each SAR resolution cell (called the ground resolution cell) depends on the local topography. It strongly depends on the terrain slope in the plane perpendicular to the orbit (ground range direction), and on the terrain slope in the azimuth direction.

Regarding the perspective deformation, in a similar fashion to what one experience each day such as looking at surfaces from different angles (e.g. a paper seen at 90 degrees is a line) the dimension of the ground resolution cell in azimuth is related to that of the SAR resolution cell. In other words, the dimension of the ground resolution cell in range is related to that of the SAR resolution cell by an unusual perspective deformation. Figure 5-4 shows how slant-range is projected onto the ground.

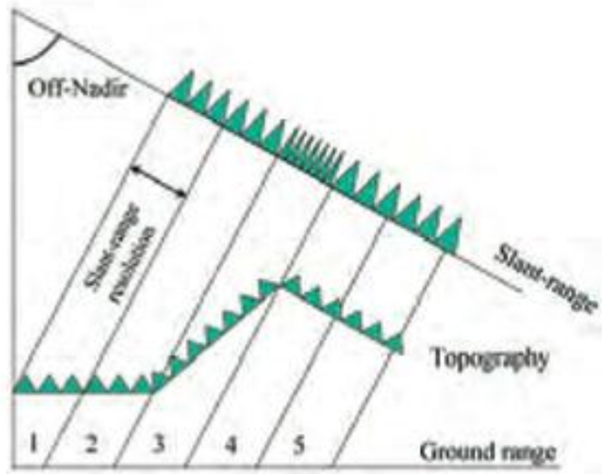

Figure 5-4 Effect of terrain on the SAR image. For SAR resolution cells in the plane perpendicular to the orbit, the part of the terrain imaged in each resolution cell clearly depends on the topography (Alessandro, et al., 2007).

5.6. Ascending and Descending Envisat passes

Envisat has the possibility to observe the same scene with incidence angles of both plus and minus 23 degrees. Observation of the whole of the Earth's surface is achieved by combination of the orbital satellite motion along the meridians (almost polar orbits) and the Earth's rotation in the equatorial plane. This possibility comes from the fact that during orbits that go from South to North (Ascending passes) and from North to South (descending passes), the SAR antenna pointing is usually fixed to the same side of the orbital plane with respect to the velocity vector. The radar antenna is always pointed to the right side of the track for Envisat i.e. Envisat is always right looking scene (Alessandro, et al., 2007).

5.7. Interferogram construction

These days, as a result of increasing number of application, radar interferometry processing has become standardized. ROI-PAC (Rosen, et al., 2004) is among the free softwares that are developed for InSAR processing. There are also commercial softwares such as GAMMA (Werner, et al., 2000). The mandatory inputs for interferogram construction are two Single Look Complex (SLC) images that are focused and that preserve the phase. These are referred to as 'master' and 'slave'. (See Figure 5-5)

5.7.1. Generation of Synthetic Fringes

A synthetic interferogram is generated based on the precise sensor orbits (in this case DORIS), timing information, and scene topography, (e.g. from a 90m resolution DEM). The DEM which is 90m by 90m resolution for this analysis is downloaded in grid format from (topex.ucsd.edu).This step assumes that a DEM is available: if an accurate DEM, sampled at the SAR resolution, is given, a complete removal of topography is possible, together with efficient spectral shift filtering.

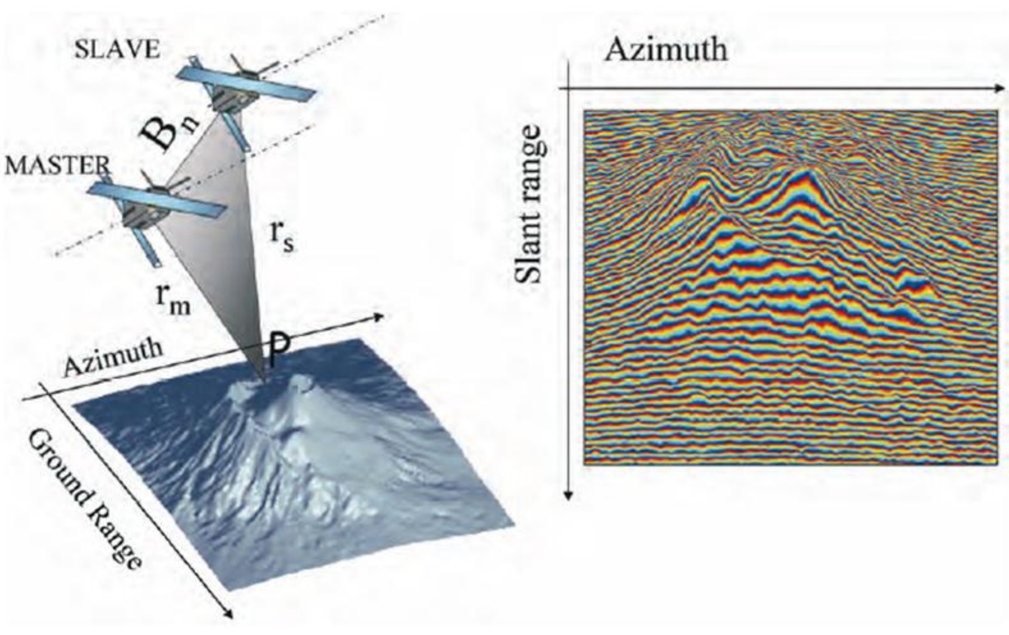

Figure 5-5 Generation of a synthetic interferogram(right) based on a DEM(left) and knowledge of the sensor orbits and timing (Alessandro, et al., 2007).

The interferogram phase is estimated by computing, for each target P in the azimuth-slant range plane, the deference in the sensor-target travel path distance for the two satellites as in figure 5.5 above (left).

$$\emptyset(P) = \frac{4\pi}{\lambda}\left[r_M(\overrightarrow{P}) - r_s(\vec{P})\right] \ldots\ldots\ldots\ldots\ldots\ldots\ldots\ldots\ldots\ldots\ldots\ldots\ldots\ldots \quad (5.2)$$

Where, $\emptyset(\mathrm{P})$ is phase change at P, $\mathrm{r_M}$ a range at Master image, $\mathrm{r_s}$ is a range at Slave image, λ is radar wavelength (5.6cm). One can see for more derivation Rosen, et al., (2000).

The actual implementation is somehow tricky, since the DEM is regularly gridded in a ground reference according to some geodetic projection, whereas the phase difference ϕ(P) is to be computed on a regular grid in the slant range, azimuth SAR reference. The complexity in transformation from SAR reference to ground reference is due to elevation dependency. So, to alleviate this complexity, it is worth helping to flatten the interferogram with respect to a reference ellipsoid (usually WGS84) so that a flat terrain profile is assumed.

The Synthetic interferogram provides an unwrapped phase field that can be used for:

- Subtracting the phase from the final SAR interferogram to remove the known topography, hence providing a differential interferogram, for monitoring change.
- Image co-registering which provides a map of the pixel to pixel mapping from the master to the slave image.

5.7.2. Co-registering

The co-registration step is fundamental in interferogram generation, as it ensures that each ground target contributes to the same (range, azimuth) pixel in both the master and the slave image. Co-registration accounts for orbit crossings/skewing, different sensor attitudes, different sampling rates, along-track and across-track shifts. However in Envisat the required transformation is manly composed of a small rotation of the two images, a range and an azimuth ‘stretch’(change in sampling rate)and further second-order effects.

A map of pixel-to-pixel correspondence could be provided, within an accuracy of one centimeter, by the synthetic fringes, scaled by the wavelength.

5.7.3. Interferogram Computation

Generation of the interferogram requires the pixel-to-pixel computation of the Hermitian product of two co-registered, spectral-shift-filtered images.

$$v_i = u_M \times u_S^* \ldots\ldots\ldots\ldots\ldots\ldots\ldots\ldots\ldots\ldots\ldots\ldots\ldots(5.3)$$

Where u_M and u_S^* refer to the master and complex conjugate of the slave images respectively.

The noise level can be reduced by averaging adjacent pixels in the complex interferogram. This processing, defined as 'complex multilooking', trades geometric resolution for phase accuracy (or altimetric resolution when the interferogram is exploited for DEM generation). Such averaging is quite effective with respect to any uncorrelated noise due to temporal, baseline, volume, etc., sources. However, it is not able to remove space-correlated artifacts, e.g. due to atmospheric turbulence, errors in flattening, or DEM removal etc. (Alessandro, et al., 2007).

The other parameter is coherence, or better its absolute value (since it is a complex quantity), provides a useful measure of the interferogram quality (SNR).

$$\hat{\gamma} = \frac{\sum_{n,m} u_1(n,m).u_2^*(n,m).e^{-j\phi(n,m)}}{\sqrt{\sum_{n,m}|u_1(n,m)|^2 \sum_{n,m}|u_1(n,m)|^2}} \ldots\ldots\ldots\ldots\ldots (5.4)$$

Where, $\phi(n,m)$ is the phase contribution due to topography, with the linear approximation.

The 'sampled' estimator is usually exploited where the summation is extended to the 2D patch of uniform speckle. The absolute value is then taken. Excluding random noise, the changes with time of the scattering properties of a target determine its coherence. For example, water bodies have low coherence because their surfaces are constantly moving; they therefore appear black in coherence images. Motion and change in vegetation also affect coherence. The more the vegetation the less is the coherence however it is possible to penetrate the leave and hit the ground and backscattered. The joint use of coherence and the amplitude of the backscatter allows for better image segmentation. While the amplitude of the return radar wave depends on the electromagnetic structure of the target, the coherence is mostly related to its mechanical stability (Alessandro, et al., 2007).

5.7.4. Interferogram Geocoding and Mosaicking

The last steps in the interferogram generation chain are Geocoding and mosaicking. Mosaicking is required when several interferograms (each, say, 30 × 100 km) are joined together to make a long strip. The need for block processing arises not only for computational efficiency, but to reduce the error due to the many approximations made so far (for example: the co-registering model, the DEM vs. SAR image alignment, the Doppler Centroid variation with azimuth etc.) (Alessandro, et al., 2007).

Geocoding is performed on the mosaicked interferogram and consists of resampling it onto a uniform grid on the reference ellipsoid. In the geocoding step, one combines the range distance equation (a sphere centered in the sensor location), and the Doppler equation (a plane orthogonal to sensor-target velocity, in the case of zero-Doppler focusing), thus getting a circle in 3D space. The actual scatterer location is found by intersection with the hyperbola obtained by assuming $\Delta r(p)$ constant (e.g. the interferometric information) or by exploiting the known DEM. In practice, this corresponds to the usual geocoding where one has to substitute the flat Earth assumption (the ellipsoid or geoid model for Earth) by the actual interferometric information. Processing is then iterated for each point, as is done for normal geocoding (Alessandro, et al., 2007).

5.7.5. Phase unwrapping techniques

Phase unwrapping (PU) is done after interferograms have already been generated and properly filtered. Since the interferometric phase is known only modulo-2π and the maximum height variation in the area of interest can give rise to hundreds of cycles, an unwrapping procedure is necessary in order to estimate the local topography. If the phase contribution due to an ideally flat Earth has been properly estimated and compensated for (i.e. the interferogram has been flattened), phase unwrapping allows one to pass from the fringe pattern (similar to a set of contour lines) to a phase field proportional to the local topography (Alessandro, et al., 2007).

The flattened interferogram provides just a measurement of the relative terrain altitude that is ambiguous. The phase variation between two points on the flattened interferogram provides a measurement of the actual altitude variation plus an integer number of altitude of ambiguity (equivalent to an integer number of 2π phase cycles). The process that allows to add to the interferometric fringes the correct number of altitude of ambiguity is called phase unwrapping. However it should be noted that usually phase unwrapping does not have a unique solution and "a priori" information should be exploited to get the right solution (Ferretti, et al., 1999).

The aim of phase unwrapping (PU) is to recover the integer number of cycles n to be added to the wrapped phase ϕ so that the unambiguous phase value ψ can be finally obtained for each image pixel:

$$\psi = \phi + 2\pi \cdot n \text{ ………………………………. } (5.5)$$

There are also various algorithms; such as branch cut (Goldstein, et al., 1988) and minimum cost flow (Chen, et al., 2000) have been developed to tackle this problem in a range of conditions. Nevertheless, the resulting interferogram often has unwrapping errors which appear as 2π phase jumps which can be spotted visually and manually corrected (Biggs, et al., 2007). However, these algorithms are beyond the scope of this thesis to be discussed.

5.7.6. Source of Errors in InSAR Interferometry

InSAR uses electromagnetic wave of C-band (with frequency of 5.331GHz and wavelength of 56.6mm), it shares the error associated with the electromagnetic signal as well as the error associated with how precisely the satellite orbit is determined (as GPS precise orbit determination). Generally, the phase signal comprises of geometric, topographic, atmospheric contributions as well as noise (thermal noise, computational error and etc.) and the deformation signal which we are looking for.

The measured phase difference between two corresponding pixels is expressed by interferometry equation (Reigber, et al., 2007) after the co-registration of the two images as:

$$\Delta\phi_{int} = \Delta\phi_{def} + \Delta\phi_{orbit} + \Delta\phi_{topo} + \Delta\phi_{flat} + \Delta\phi_{atm} + \Delta\phi_{noise} \ldots\ldots\ldots(5.6)$$

where, $\Delta\phi_{def}$ is deformation(differential displacement pattern) , $\Delta\phi_{flat}$ is flat earth phase caused by the imaging geometry $\Delta\phi_{orbit}$ is phase error caused by inaccurate orbit parameters, $\Delta\phi_{topo}$ is topographic phase signature $\Delta\phi_{atm}$ is atmospheric artefacts and $\Delta\phi_{noise}$ is noise.

5.7.6.1. Orbital contribution

If the satellite's orbits and the ground topography are accurately known, the differences in satellite viewing geometry can be corrected. There are a number of phenomena which cause perturbation from a nominal elliptical orbit. Among them, are tidal pull and lateral variation in the earth's gravity field, which can be modeled accurately, however, factors such as solar radiation pressure, thermal re-radiation and atmospheric drag, are more difficult to model (Ziebart, et al., 2005).

Baseline separation causes a difference in path length which varies primarily with incidence angle and to a lesser degree with topography. InSAR processing software, such as ROI-PAC, initially removes the effect of baseline separation approximating the surface of the earth to be a smooth ellipsoid; once linearized, the resulting rate of change in phase with respect to incidence angle is directly proportional to the perpendicular baseline. Subsequently, a digital elevation model (DEM) can be used to correct for additional topographic effects (Biggs, et al., 2007). Precise orbit data are available for interferogram computation. In this thesis, DORIS Precise orbit data is used (www.doris.tudelft.nl).

Attempting to remove the orbital contribution empirically will remove the long-wavelength component of the signal. For many applications, such as glaciology and volcanology, this approach is sufficient since the deformation signal is only present in a small portion of the interferogram and it is possible to define a 'far-field' area of the interferogram which is not affected by deformation and use this to re-estimate the baseline parameters (Biggs, et al., 2007).

5.7.6.2. Atmospheric contribution

Phase distortion due to atmospheric effects (i.e. refractive index variations in the propagation medium) has gained increasing attention since it can seriously compromise InSAR quality, especially for those pass pairs with low normal baseline values. These effects are mainly due to the time and space variations of atmospheric water-vapor and exhibit power law energy spectra.

Atmospheric errors result from interactions between the radar beam and the atmosphere it passes through. The amount of atmospheric phase delay is determined by the refractive index; primarily a function of pressure and temperature (the 'dry' component) and water-vapor content (the 'wet' component). On the length scale of interferograms, the most variable, and therefore, the most significant factor is the amount of water-vapor in the troposphere (Biggs, et al., 2007).

5.8. Softwares used for InSAR data analysis

The main Software used to process the Envisat raw data and interferogram formation is ROI-PAC from Caltech/JPL (Rosen, et al., 2004). However there are also softwares/scripts used for further data analysis and for time series and rate estimation. One of the additional software is PI-RATE (Poly Interferometric Rate and Time Series Estimator) developed in University of Leeds. A script written by Juliet Biggs, University of Bristol is also used.

5.8.1. ROI-PAC

The general principle of interferogram construction and source of errors in InSAR interferometry is described in section 5.7. Here, with a brief recap we show how the software is dealing with the InSAR processing mentioned.

1. Creating a Single look complex (SLC)

The input is a pair of overlapping radar images taken from slightly different vantage point at different time (for Envisat 35 days is a minimum repeat pass), analogous to a stereo pair of aerial photographs used to produce a topographic map. These raw pair of images must be changed to SLC image which is compatible to ROI-PAC to form an interferogram from the first acquisition (master) and second acquisition (slave) images. The individual files are composed of two layers with amplitude and phase. Each image has corresponding '.rsc' file that tells about the file size and give some relevant satellite parameters (Hamling, 2010).

Co-registration of overlapping radar images

After the SLCs have been processed, the two images should be co-registered. Co-registration is the process of resampling the slave images into the master image geometry. The matching is done in the Fourier domain (using FFT) by cross-correlating the master image with the slave (Hamling, 2010).

2. Interferogram formation

When two images have been successfully co-registered, an interferogram can be produced simply by differencing the phase values of corresponding pixels. This is done by multiplying the complex phase of the master image by the complex conjugate phase of the slave image.

Mathematically:

$$I_M = A_M e^{i\emptyset_M} \ldots\ldots\ldots\ldots\ldots (5.7)$$

and

$$I_S = A_S e^{i\emptyset_S} \ldots\ldots\ldots\ldots\ldots (5.8)$$

Thus

$$I_M I_S^* = A_M A_S e^{i(\emptyset_M - \emptyset_S)} \ldots\ldots\ldots\ldots\ldots\ldots (5.9)$$

where, the subscript 'M' for Master image and 'S' for Slave image. A_M and A_S are the amplitude of the master and the slave respectively. And, $\emptyset_M and$ $\emptyset_S$ are the phases of master and slave phases respectively (Hamling, 2010).

As a result of the multiplication, the noise level is increased but to improve the signal to noise ratio (SNR), the interferogram is averaged in the azimuth direction. Actually, the pixel size for Envisat is ~5 m in Azimuth and ~20 m in range. Thus, four looks are taken in azimuth to make the pixels in the interferogram square. The interferogram produced includes contributions from the different viewing geometry of the two parent images, topography, and path delays owing to two different atmospheric conditions, noise, and range changes caused by surface deformation during the interval spanned by the image acquisitions. This is the last bit of information that we would like to tease out of the data, removing other source of phase difference in the interferogram (Hamling, 2010).

3. Removing the effects of viewing geometry and topography

The difference in viewing geometry between two images acquired from slightly different vantage point produces a regular pattern of phase difference between the images. If the target area were perfectly flat, these differences would manifest themselves in the interferogram as a series of nearly parallel band called orbital fringes. These can be computed and removed based on the known trajectory and imaging geometry of the SAR, along with the small additional effect of Earth's curvature. The result is called a flattened interferogram (Dzurisin, et al., 2007).

The effect of surface topography can be removed from a flattened interferogram by first constructing a synthetic interferogram based on known topography (i.e. on a DEM). Subtracting the synthetic interferogram from the observed flattened interferogram, one left with a topographic removed interferogram. However, this interferogram contains only the effect of noise, path delays, and surface deformation (the useful signal) (Hamling, 2010).

4. Filtering

A topographic removed interferogram can be spatially filtered to reduce the effect of short-wavelength noise, and displayed over an amplitude image to facilitate visual correlation of deformation fringes with surface features. The filtering stage is essential to improve further SNR. The filter applied is a non-linear power spectrum filter (Goldstein, et al., 1998). It is calculated by dividing the interfereogram into overlapping rectangular patches. The power spectrum, Z(u,v), is computed by smoothing the intensity of the 2D Fast Fourier Transform (FFT). Thus, the response of the filter is give by:

$$H(u,v) = |Z(u,v)|^{\alpha} \qquad \text{……………………….(5.10)}$$

Where $0 \le \alpha \le 1$, in the extreme $\alpha = 0$, implies no filter applied and $\alpha = 1$ is for strong filtering.

5. Phase unwrapping

Phase unwrapping is a process of converting the modulo 2π interferogrametric phase into a continuous signal. It is important to get rid of phase discontinuities. The branch cut algorithm based on (Goldstein, et al., 1998) is used to unwrap the interferogram in ROI-PAC.

6. Geocoding

The final stage is geocoding. It is the mapping of the interferogram into geographic coordinates using the information gathered while matching the simulated amplitude image from the DEM to the master geometry (Hamling, 2010).

All the above Steps can be summarized in the following flow chart (see, figure 5-6).

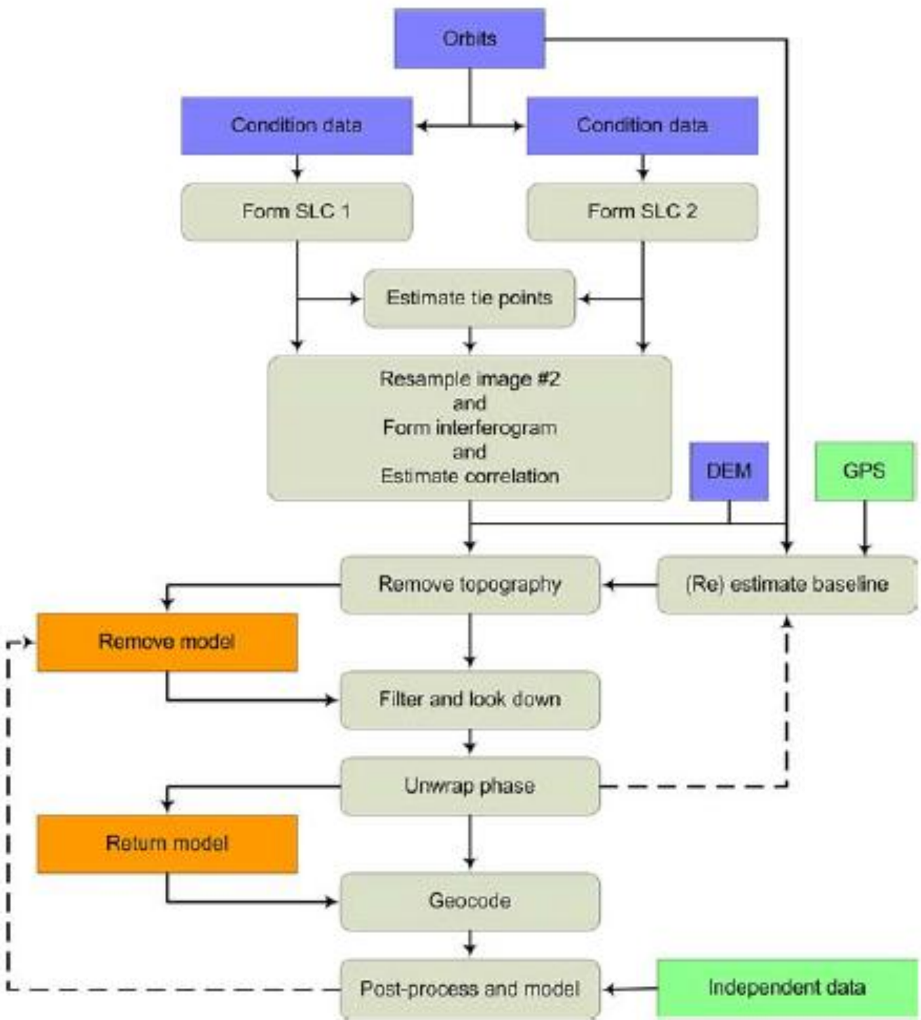

Figure 5-6 ROI-PAC work flow (Simons, et al., 2007)

5.8.2. Time Series Analysis

5.8.2.1. Simple/traditional Stacking

Large magnitude earthquakes and magmatic intrusions can be detected with a single interferogram derived from the two acquisitions before and after the event. However, small scale deformation cannot be detected as such. Instead, it requires interferograms which cover large period of time so that the signal (required deformation) can be isolated from unwanted signal (i.e. noise). In fact, the higher the temporal variation, the more will be decorrelation of the interferograms. The way out, sometimes, is stacking each interferogram. The disadvantage of stacking is that it increases the signal to noise ration by a factor of $\sqrt{N}$ despite the signal of the stacked N interfrogams increased by N times. The principle of stacking is: selecting one master interferogram which is coherent and pick a pixel. Then subtract this master interferogram from each interferogram to get the residuals and add up all the residuals. The sum will then be changed from radar geometry (radian) into cm or mm (Hamling, 2010). To get the rate the stacked value will be divided by the duration. The Matlab scripts which do the traditional stacking can be seen in Appendices C and D.

5.8.2.2. Chain Stacking

Chain stacking is an alternate way of simple stacking in a way that the slave of the first interferogram will be the master of the next interferogram. Hence, orbital and atmospheric errors from the middle acquisition are cancelled leaving the contributions from only the first master and last slave. The advantage of the chain method is that it can be constructed from a set of short time-period interferograms which do not suffer from the effects of temporal decorrelation like in the traditional stacking method. However, only pixels which are coherent in every interferogram remain (Hamling, 2010).

5.8.2.3. Simple Time Series

As many combinations as possible inteferogram can be constructed from each acquisition of InSAR data. However, due to temporal and spatial (large perpendicular baseline) interferograms will have large decorrelation. Thus, by selecting interferogram that are coherent, it is possible to do time series. Below is the mathematical formulation and example of this method as it is given in (Hamling, 2010) and (Biggs, 2007) .

The formulation to find the time series of the displacements, generally, can be given by:

$$\boldsymbol{Gm} = \boldsymbol{d} \quad \dots\dots\dots\dots\dots\dots(5.11)$$

Where, $\boldsymbol{G}$ is design matrix, $\boldsymbol{m}$ is the displacement vector to be solved for and $\boldsymbol{d}$, is a vector containing the observed displacement from each interferogram. Thus, least-square inversion technique can be formed to find the time series of displacements.

$$\boldsymbol{m} = (\boldsymbol{G}^T\boldsymbol{G})^{-1}\boldsymbol{G}^T\boldsymbol{d} \dots\dots\dots\dots\dots\dots(5.12)$$

5.8.2.4. Π-RATE

Π-RATE (Poly-Interferogram Rate And Time-series Estimator) is a Matlab-based software package that estimates displacement rate, time series and their associated uncertainties from a set of unwrapped InSAR images (Wang, et al., 2012). The π-rate software was developed by Hua Wang at the University of Leeds with contributions of Tim Wright, Juliet Biggs[2] and John Elliot[3]. The development history of π-rate is mentioned in the user manual (Wang, et al., 2012). The viewer for the results from π-rate is Sarview software which is developed also in University of Leeds. The π-rate algorithm overview and processing steps describe in detail in the Ph.d. thesis of Ian Hammling (Hamling, 2010). A brief summary will be discussed below.

Algorithm overview

Inputs for processing with pirate are unwrapped and geocoded interferograms. The algorithm consists of four main steps: an orbital error correction, an atmospheric correction, construction of a rate map and estimation of the associated errors. For a given interferogram network a minimum spanning tree (MST) algorithm is applied based on the fraction of unwrapped pixels. The tie point with the maximum number of coherent pixels and minimum standard deviation is then selected as the reference point.

Orbital Correction

ROI-PAC removes the effect of the baseline from the interferogram assuming the Earth is a smooth ellipsoid and that the satellite orbits are accurately known. However, practically, our knowledge of the satellite orbits is based on models with reported accuracies of 5-7cm

[2] University of Bristol
[3] University of Oxford

in the radial direction and 10-15 cm cross-track (Scharoo, et al., 1998). An orbital error still remains even after effects of the baseline are removed (Zebker, 1994). Thus, this orbital error can be estimate and removed using the method of (Biggs, et al., 2007) which is implemented in π-rate.

Atmospheric correction

To correct for the atmosphere π-rate adopts the same approach used to estimate the orbital errors described above. As with the orbital correction; each of the interferograms is down sampled by taking a further 10 looks. The phase value $\emptyset_{ijk}$ (where i and j are standing for the i^{th} and j^{th} pixel and k is standing for the k^{th} interferogram) at each pixel in all of the interferograms, is then used to invert for the correlation of phase change with topography using a down sampled DEM such that:

$$\emptyset_{ijk} = (w_j - w_i)h_k + c_{ij}, \ldots\ldots\ldots\ldots\ldots\ldots\ldots\ldots\ldots(5.13\ )$$

Where, $w_{i,j}$ are the phase gradients for the i^{th} and j^{th} pixels, h is the elevation and c is a static offset in the interferogram. Once solved for the gradients are forward modeled to generate a synthetic interferogram of atmospheric noise, which is subsequently removed from each of the interferograms in the network.

.Variance-covariance estimation

The variance-covariance matrix (VCM) is calculated using a 1-D covariance function specific to each interferogram. It is assumed that the principal source of noise in the interferogram is due to variation in water vapor content in the troposphere between acquisitions. Once the covariance function is being calculated, it will be used to construct the variance-covariance matrix (VCM) by fitting a functional model similar to that given in equation (5.8.8)

$$c(r_{ij}) = \sigma^2 e^{(-\frac{r_{ij}}{\alpha})} \ldots\ldots\ldots\ldots\ldots(5.14)$$

Where $c(r_{ij})$ is the covariance between pixels i and j, σ^2 is the variance; r is the distance between the pixels, and α is a constants governing the length scale of decay.

Time Series Estimation

For most applications it can be assumed that the surface displacements are smooth with time. To minimize the effects of any residual atmospheric noise, orbital and unwrapping errors a smoothing constraint can be included. There are a number of methods to calculate the smoothing constraint including finite difference approximations (Schmidt, et al., 2003) and singular value decomposition (Berardino, et al., 2002).

The Laplacian smoothing method utilizes the finite difference approximation of the second order differential of the time series as a smoothing constraint such that

$$\begin{pmatrix} \boldsymbol{G} & 0 \\ \gamma^2 & \frac{d^2}{dt^2} \end{pmatrix} \boldsymbol{m} = \begin{pmatrix} \boldsymbol{d} \\ 0 \end{pmatrix} \ldots\ldots\ldots\ldots\ldots\ldots\ldots(5.15)$$

where, γ^2 is the weighting for the smoothing parameter, **G** is the design matrix, **m** is the model,**d** is the data to be fitted and $\frac{d^2}{dt^2}$ is the second order differential. For $\gamma = 0$ no smoothing is applied and the time series will be rough and prone to sharp fluctuations from one time step to another, for large values of γ the time series will be dampened.

If **G** is rank deficient, as in the case for a network of interferograms, which cannot be connected, and therefore $\mathbf{G}^{\mathbf{T}}\mathbf{G}$ is singular, it is not possible to find the inverse of **G** directly. To overcome this problem **G** can be decomposed using the SVD method whereby the pseudo-inverse of **G**, which gives the minimum-norm least squares solution, is obtained.

Stacking and rate map formation

The final processing step is the formation of the rate map. In forming the rate map it is necessary to combine all of the measurements from pixels that are coherent in most of the interferograms. This is done using the MST matrix. Each interferogram is checked to ensure that the minimum number of observations is available for each pixel and a least squares inversion is adopted on a pixel-by-pixel basis to find the best fitting rate,r_{los}.

$$\frac{2\pi}{\lambda}\boldsymbol{T}r_{los} = \boldsymbol{P} \ldots\ldots\ldots\ldots\ \ldots..(5.16)$$

where T is a vector containing the time-spans, and P is a vector of phase values, at each pixel in each interferogram and λ is the wavelength.

To account for the correlation between interferograms and any residual atmospheric and orbital noise the inversion is weighted using a variance-covariance matrix,Σ_P. Each element, within the variance-covariance matrix depends on the atmospheric error for each interferogram, the orbital error for each pixel, and the correlation between interferograms.

The rate and associated error are then:

$$\frac{\lambda}{2\pi}[\boldsymbol{T}^T\Sigma_P^{-1}\boldsymbol{T}]^{-1}\boldsymbol{T}^T\Sigma_P^{-1}\boldsymbol{P}\text{……………………….}(5.17)$$

$$\Sigma_r = [\boldsymbol{T}^T\Sigma_P^{-1}\boldsymbol{T}]^{-1}\text{…………………….}(5.18)$$

To ensure that unreliable pixels aren't included in the final rate map the variance for each pixel is compared with an a priori value, typically 2 mm. If the variance is greater, then this pixel is removed from the rate map. Once the rate map is formed the standard deviation at each pixel is examined and compared with a user defined allowable maximum error. Any pixels with standard deviations that exceed this value are then removed from the final rate map. The aforementioned processing steps for calculating a rate map using π- rate is summarized in the following flow chart (see, figure 5.7)

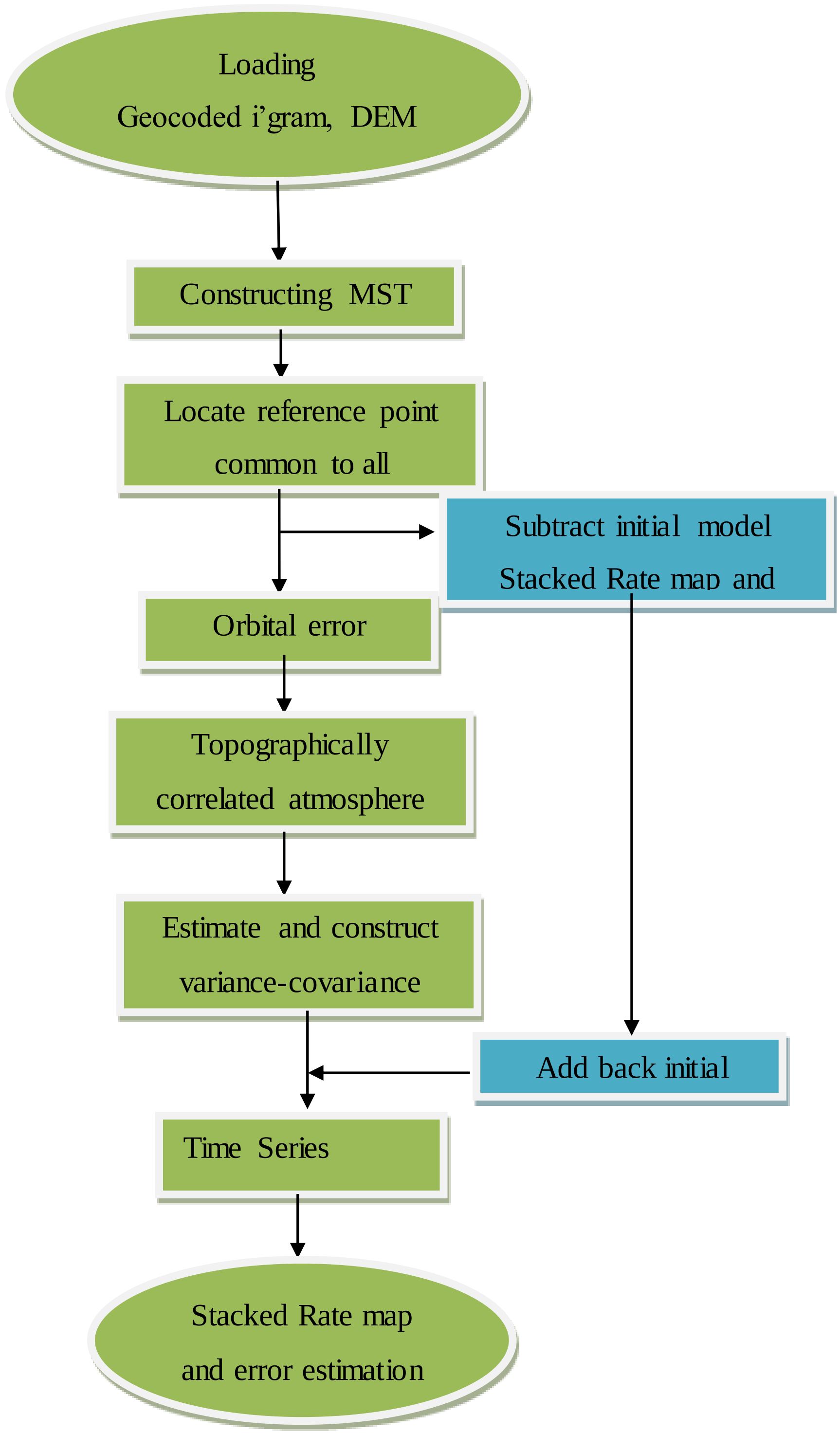

Figure 5-7 Flowchart showing the main processing steps for calculating a rate map using π- rate (Hamling, 2010).

5.9. InSAR Data Source and Interferograms constructed

5.9.1. Data Source

The InSAR data used is from Envisat Satellite, ASAR, image mode (IM2) and Level 0(raw). Two tracks, namely: track 028 ascending track and track 278 which is descending are used. The data is acquired from the European Space Agency (ESA). Table 5-1 shows dates of acquisition of InSAR data for track 028. The range of the dates is from 2008-05-28 to 2010-02-17 a total of 19 data with 35 days interval have been taken from this track.

No.	Date of Acquisition		No.	Date of Acquisition
1	2008-05-28		11	2009-05-13
2	2008-07-04		12	2009-06-17
3	2008-08-06		13	2009-07-22
4	2008-09-10		14	2009-08-26
5	2008-10-15		15	2009-09-30
6	2008-11-19		16	2009-11-04
7	2008-12-25		17	2009-12-09
8	2009-01-28		18	2010-01-13
9	2009-03-04		19	2010-02-17
10	2009-04-08			

Table 5-1 Track 028 date of acquisition

On the other hand, a total of 25 data set has been taken for track 278. This was taken in the time span from 2008-05-11 to 2010-10-03, with 35 days interval between acquisitions(see, Table 5-2).

No.	Date of Acquisition		No.	Date of Acquisition
1	2008-05-11		14	2009-08-09
2	2008-06-15		15	2009-09-13
3	2008-07-20		16	2009-10-18
4	2008-08-24		17	2009-11-22
5	2008-09-28		18	2009-12-27
6	2008-11-02		19	2010-01-31

7	2008-12-07		20	2010-03-07
8	2009-01-11		21	2010-05-16
9	2009-02-15		22	2010-06-20
10	2009-03-22		23	2010-07-25
11	2009-04-26		24	2010-08-29
12	2009-05-31		25	2010-10-03
13	2009-07-06			

Table 5-2 Track 278 date of acquisition

5.9.2. Interferogram constructed

By combining the different data sets mentioned in section 5.9.1 interferograms are formed for both track 028 and 278. Tables 5-3 and 5-4 summarize the interferograms formed.

No.	Master	Slave
1	080528	080702
2	080528	080806
3	080528	080910
4	080528	081015
5	080528	081119
6	080528	081224
7	080528	090128
8	080528	091209
9	080528	100113
10	080528	100217
11	080806	081224
12	080806	090722
13	080806	091104
14	080806	100113
15	080910	081015
16	080910	091104
17	081015	081119
26	081015	081224

18	080528	090304
19	080528	090408
20	080528	090513
21	080528	090617
22	080528	090722
23	080528	090826
24	080528	090930
25	080528	091104
27	081015	100113
28	081119	081224
29	081224	090128
30	081224	090408
31	081224	090930
32	081224	091104
33	081224	091209
34	081224	100113
35	090128	090304
36	090128	091209
37	090304	090408

39	090408	090513
40	090408	090617
41	090408	091104
42	090408	091209
43	090408	100113
44	090408	100217
45	090513	090617
46	090513	100217
47	090617	090722
48	090722	090826
49	090722	090930
50	090722	091104
51	090826	090930
52	090930	091104
53	091104	091209
54	091104	100113
55	091209	100113
56	100113	100217

Table 5-3 Track 028 combination of interferograms

No.	Master	Slave
1	080511	080615
2	080511	080720
3	080511	080824
4	080511	080928
5	080511	081102
6	080511	081207
7	080511	090111
8	080511	090215
9	080511	090322
10	080511	090426
11	080511	090531
12	080511	090705
13	080511	090809
14	080511	090913
15	080511	091018
16	080511	091122
17	080511	091227
18	080511	100131
19	080511	100307
20	080511	100516
21	080511	100620
22	080511	100725
23	080511	100829
24	080511	101003
25	080615	080720
26	080720	080824
27	080824	080928
28	080928	081102
29	081102	081207
30	081207	090111
31	090111	090215
32	090215	090322
33	090322	090426
34	090426	090531
35	090531	090705
36	090705	090809
37	090809	090913
38	090913	091018
39	091018	091122
40	091122	091227
41	091227	100131
42	100131	100307
43	100307	100516
44	100516	100620
45	100620	100725
46	100725	100829
47	100829	101003

Table 5-4 Track 278 interferograms

Chapter Six

6. InSAR Result and Discussion

6.1. InSAR Result

The results from both track 028 and track 278 shows that there is a subsidence in the direction of satellite line of site (LOS), at the location of the study area.

The following geocoded interferograms (Figure 6-1 and Figure 6-2) are from track 278 track 028 respectively constructed using ROI-PAC software and plotting using GMT. The black circle shows the specific location of the area where the subsidence took place. The red color shows away from the satellite, which is subsidence.

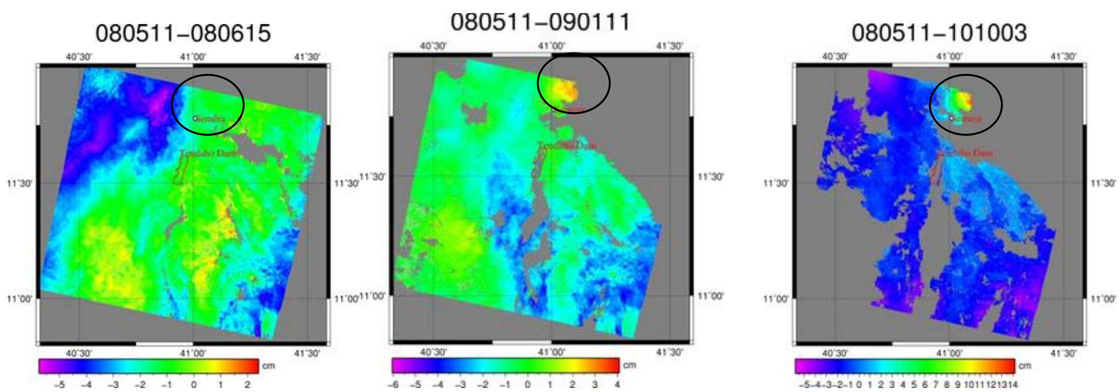

Figure 6-1 Track 278 Geocoded interferograms

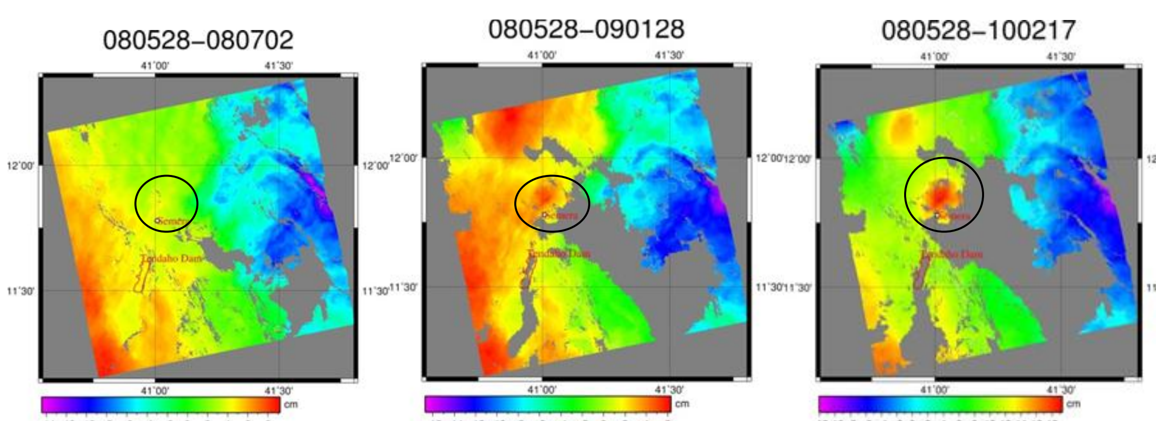

Figure 6-2 Track 028 Geocoded interferograms

Traditional Stacking and rate results

As mentioned in section 5.8.2.1, the stacking helps the analysis by increasing the signal to noise ratio (SNR).The scripts that do traditional stacking is described in Appendix C and D. The implementation of this approach also showed that there is subsidence, which is at the study area marked by the blue color (Figures 6-2 and 6-3). Here, the blue color indicates that there is a movement away from the satellite. The rate of subsidence is ~35mm/yr (track 278) and ~25mm/yr (track 028). The uplift at the left top corner of the plot which is shown by red color in track 028 is southern tip of Ado Ale Volcanic Complex (AVC).

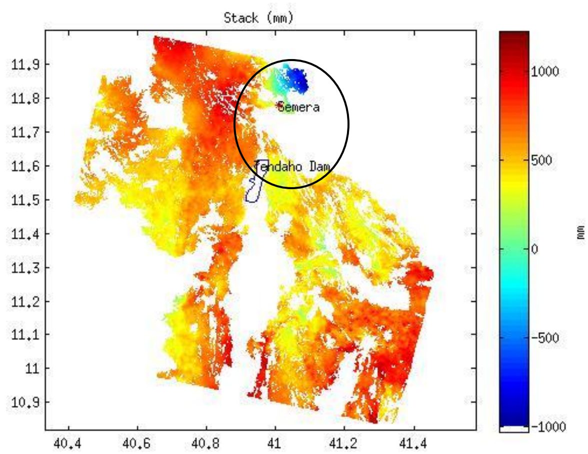

(a)

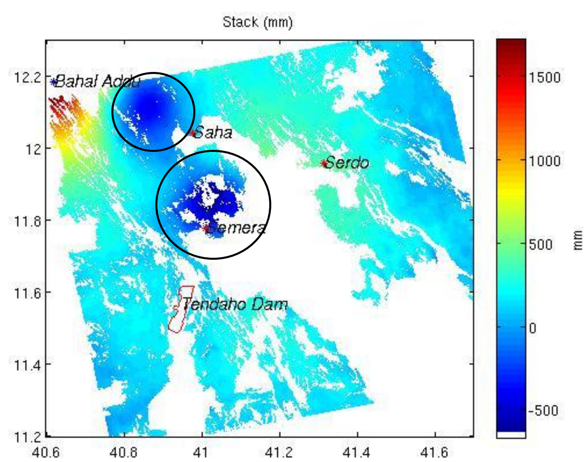

(b)

Figure 6-3 Traditional stacking (a) track 278 and (b) track 028, black circle shows the area of subsidence (The blue color shows subsidence and red shows uplift)

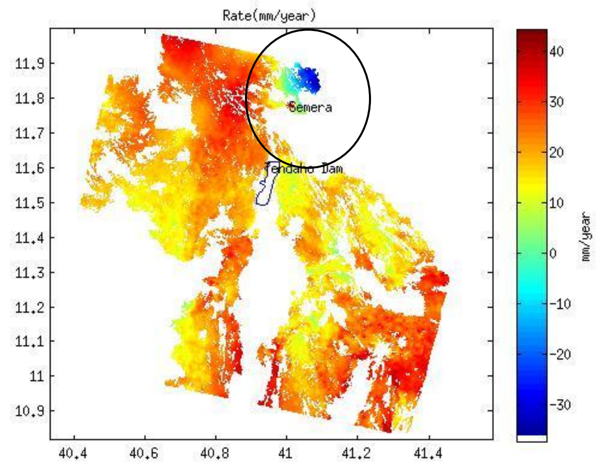

(a)

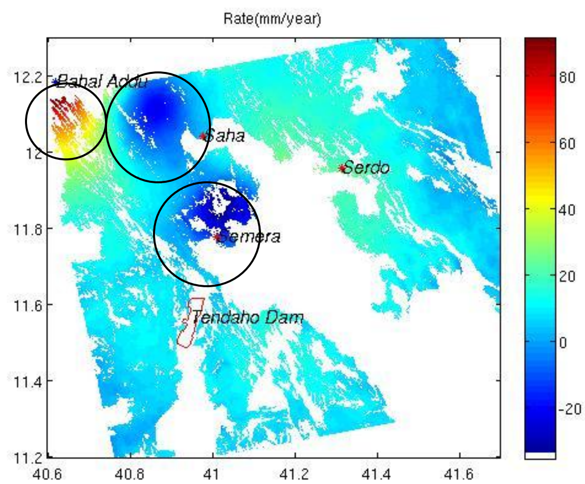

(b)

Figure 6-4 The rate map (a) track 278 and (b) track 028; the block circle shows the area of subsidence

The rate maps in figure 6-4 shows that the subsidence rate is -35 mm/yr and -25 mm/yr for track 278 and track 028 respectively. There is a difference in rate in the ascending and descending track. The main difference lies on the data time range. Track 278 has more data range (i.e. from 2008-05-11 to 2010-10-03) than track 028 (i.e. from 2008-05-28 to 2010-02-17) which indicates the more the data range the better the capability in capturing the deformation. There is also a subsidence and associated uplift in the Northwest of the study area which is the southern tip of Ado Ale volcanic complex which is associated with the dike intrusion in the area.

Pirate results

The stacking result using the Pirate software shows that the subsidence is ~55mm/yr (track 278) and ~50mm/yr (track 028). The black circle in figure 6-5 shows the area of subsidence.

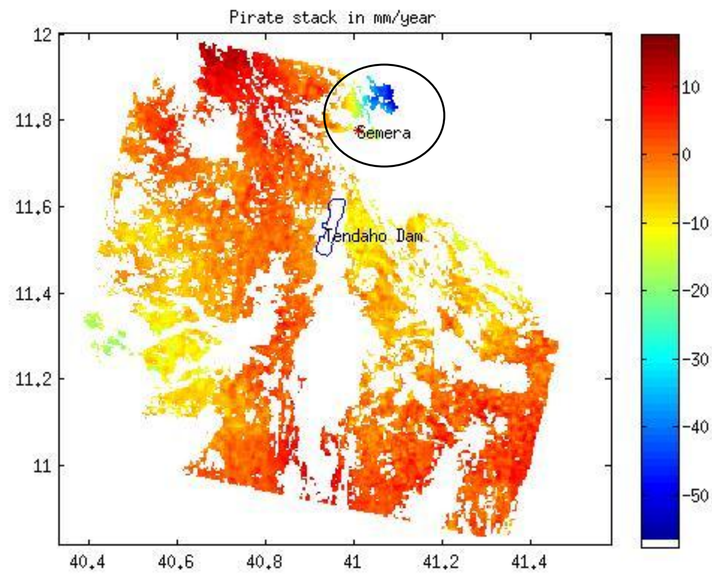

(a)

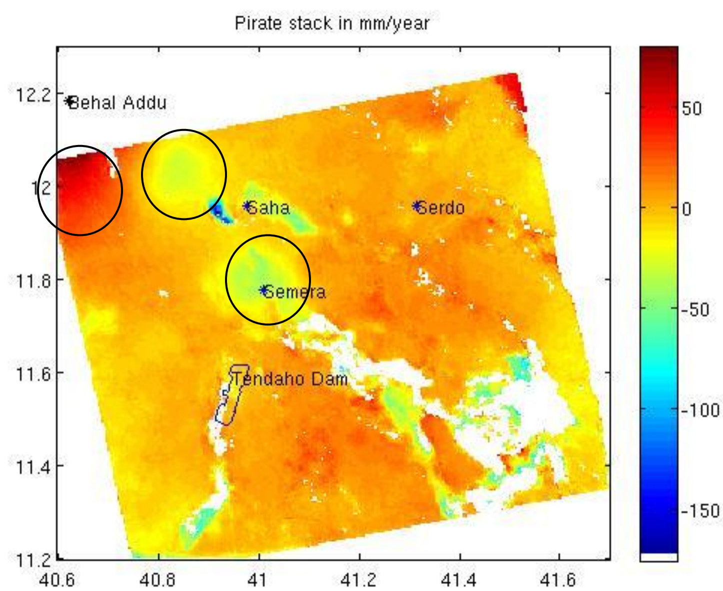

(b)

Figure 6-5 Pirate stacked map (a) track 278 and (b) track 028. The black circles show the deformation. Red is uplift and blue is subsidence.

The figure 6-6 shows the coherence of the interferograms that are stacked together. Most of the area is coherent. This is because arid areas with less vegetation like afar is best for InSAR data acquisition so as for processing.

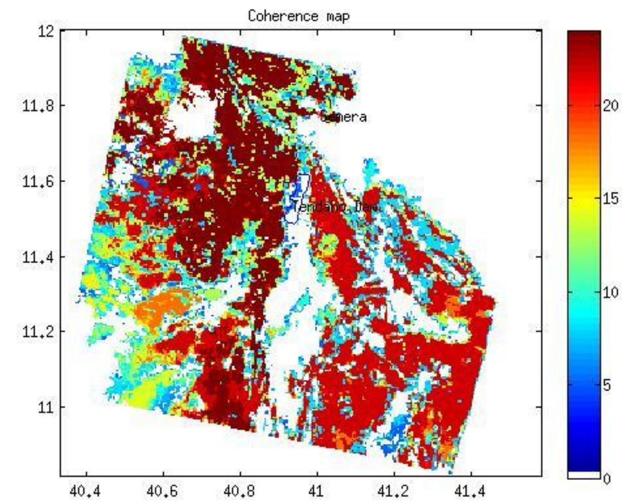

(a)

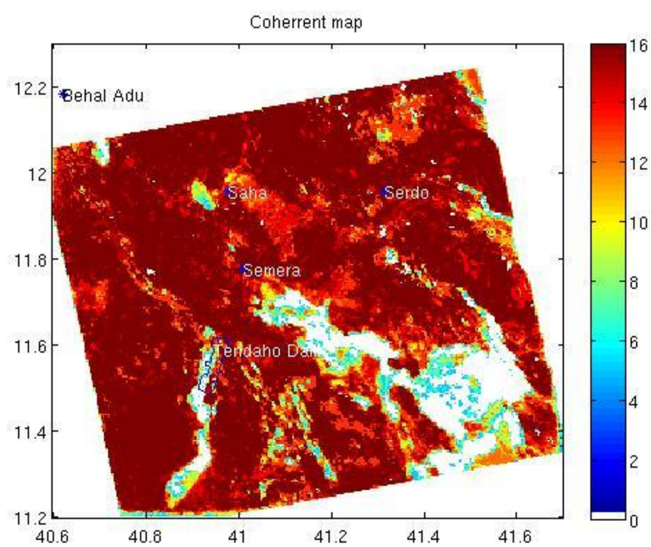

(b)

Figure 6-6 Pirate Coherence map (a) track 278 and (b) track 028, showing the intensity of the coherence of the interferograms

Figure 6-7 shows the error associated with each pixel of the interferograms in the study area. The error ranges form $\pm$ 3.9 mm/yr to $\pm$ 4.9 mm/yr for track 278 and from $\pm$1 mm/yr to $\pm$ 4mm/yr for track 028.

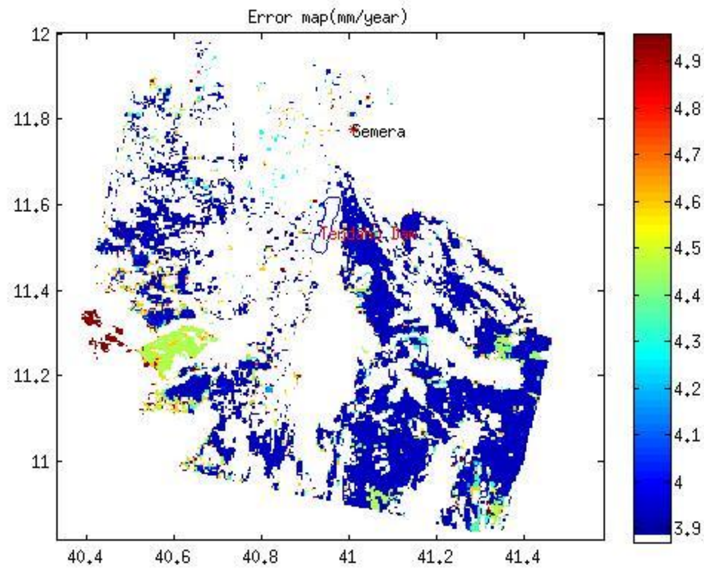

(a)

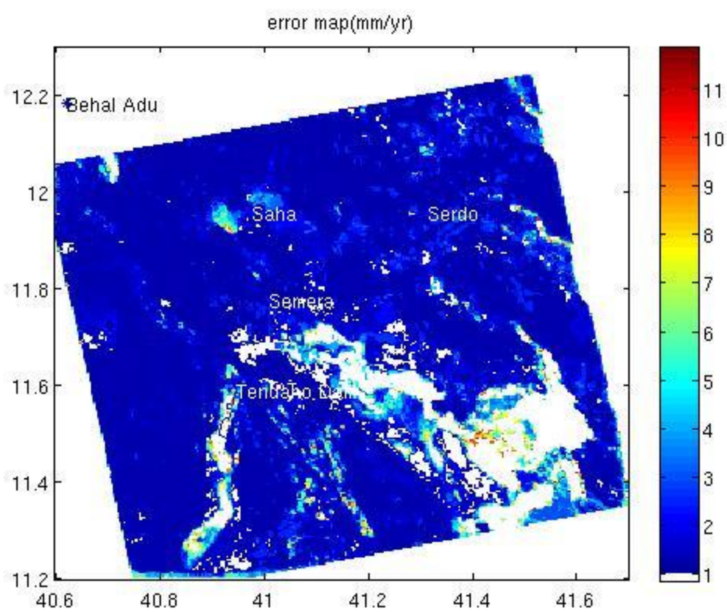

(b)

Figure 6-7 Pirate Error map (mm/yr) (a) track 278 and (b) track 028.

Chain stacking

Chain stacking is done using the script developed by Biggs (Biggs, et al., 2007). Figure 6-8 shows the cumulative displacement of each pixel of interferograms at each day of acquisition with respect to the first date of acquisition in this process. For track 278, the deformation pattern over the time scale is studied by subtracting the value of each pixel of the interferograms from the reference pixel observed on 2008-05-11. Similarly, the deformation of the ground surface is computed from track 028 by subtracting each pixel from the reference pixel on 2008-05-28 of the interferogram. This shows that as the time advances the area continued to subside. The difference arises from the duration of the data sets used.

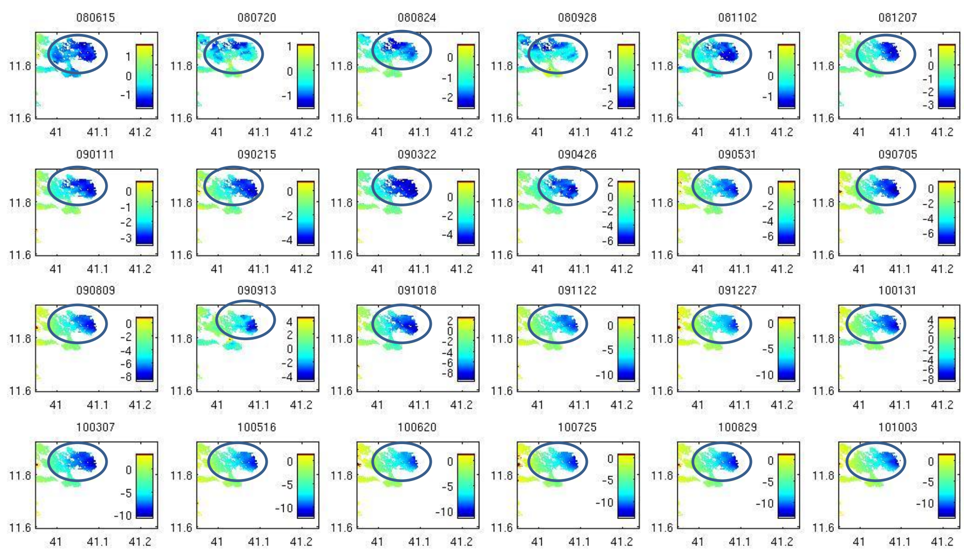

(a)

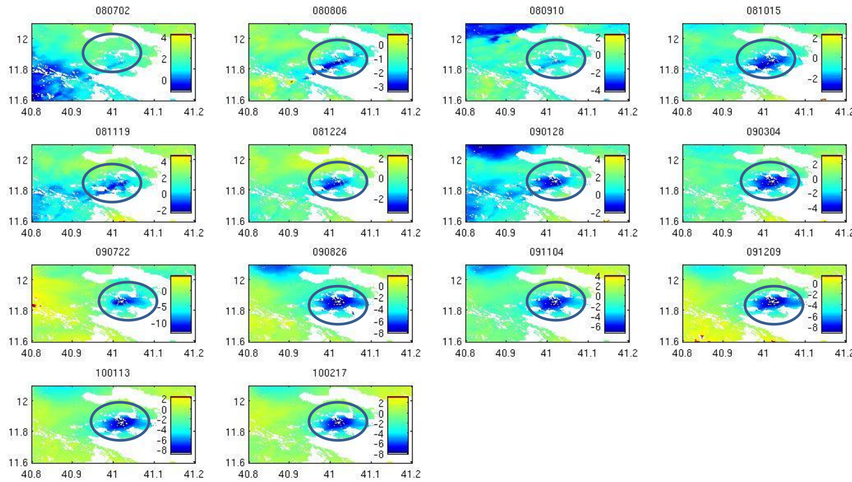

(b)

Figure 6-8 Cumulative displacement (cm) of (a) track 278 and (b) track 028.

The cumulative displacement at DASM (the location of the GPS station in Semera) which is at periphery of the area of subsidence is shown in figure 6-9 in both tracks. Though, at a lower rate this also shows subsidence. The maximum cumulative subsidence is 115 mm for track 278 and 50 mm for track 028 with respect to 2008-05-11 and 2008-05-28 respectively. This result agrees with the result from pirate in such a way that -55mm/yr for two years and -50mm/yr for one year.

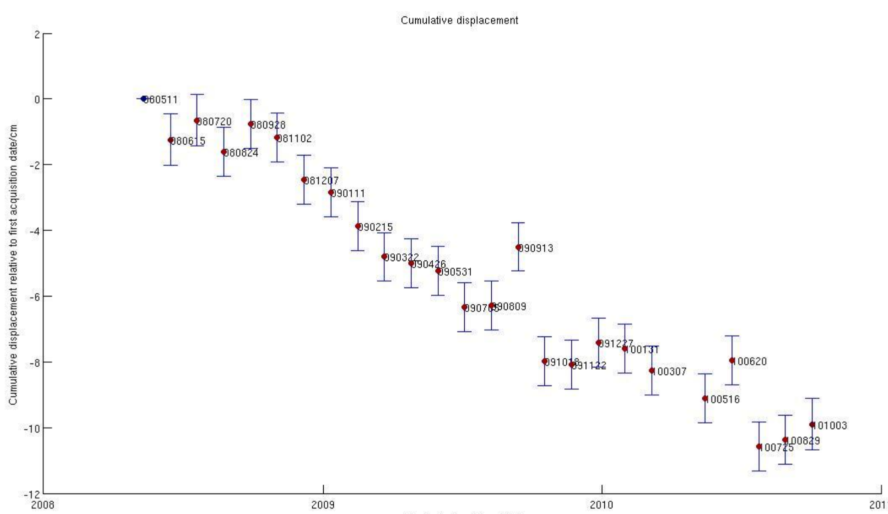

(a)

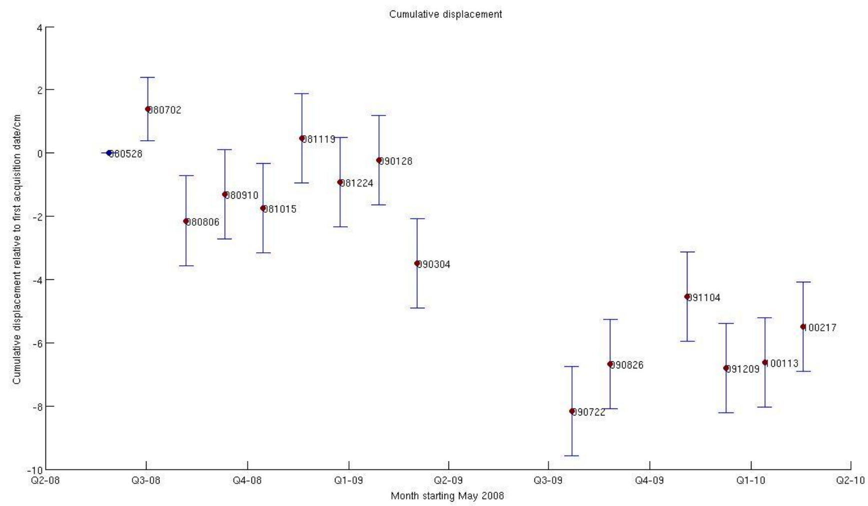

(b)

Figure 6-9 cumulative displacement (cm) of (a) track 278 and (b) track 028 at DASM GPS station.

6.2. InSAR Discussion

The interferograms constructed from Track 028 and track 278 (figure 6-1 and Appendix A) shows strong signals in the northeastern part of Semera. Track 028 not only showed the deformation in the study area but it also helped to compare it to what is happening at the southern tip of the Ado Ale Volcanic complex (AVC). InSAR measurement results in section 6.1 show one dimensional (1D) deformation along the satellite line of site (LOS).

Figure 6-4 shows also the rate map of each pixel with maximum subsidence of ~35mm/yr (track 278) and ~25 mm/yr (track 028). This method is simple to implement; however it does not consider phase contribution from atmosphere and orbit.

To alleviate atmospheric and orbital phase contribution, pirate software is used. Thus, from pirate results, it can be seen that the overall interferogram is coherent and the signal can be seen clearly. The pirate stacking given in figure 6-5 clearly shows the two subsidence areas in track 028 and a subsidence in north east of semera in track 278. The maximum rates are ~55mm/yr and ~50mm/yr for track 278 and 028 respectively.

The difference is due to track 278 having longer time of measurement than track 028 and as a result the longer measurement has a better approximation of the rate.

Figure 6-6 shows how coherent each pixel is in the process. The more coherent the interferogram is, the better to understand the signal in each interferogram. Thus, both are coherent enough for deformation analysis. Figure 6-7 shows the error in the processing. The error from track 278 is bigger than that of 028 within the study area. This is because the interferogram used in this process from track 028 are with small perpendicular baseline and smaller temporal variation. From this one can see that the smaller the perpendicular baseline the better the interferogram.

The last method that is used is chain stacking which looks for a cumulative displacement of each pixel. Figure 6-8 shows cumulative displacement of each acquisition date with respect to 2008-05-11 for track 028 and 2008-05-28 for track 278. Figure 6-9 also shows the time series of a pixel at DASM GPS station. The cumulative displacement shown within the circle is subsidence. Therefore, these results also agree with the pirate method.

The time-series plot at DASM GPS station shows a clear subsidence with maximum of -120 mm for track 278 and -90 mm for track 028 with respect to 2008-05-11 for track 028 and 2008-05-28 for track 278. The reason for the difference is mainly due to the different time span used for the two series.

Generally, from the aforementioned discussions there is a clear subsidence in the north east of Semera town, central Afar, which is the focus area of this thesis. In addition there is uplift and subsidence in the southeastern part of the AVC.

6.3. Combined result of GPS and InSAR

In this section the results from InSAR and GPS will be compared and a final conclusion will be drawn. Figures 6-10 and 6-11 show the comparison of GPS and InSAR results. After changing the 3D GPS time-series, topocentric coordinate of DASM (the GPS station located at Semera) which is changed in to 1D Envisat LOS comparison is made to see how both results are correlated to each other. The result from the two satellite geodetic methods is plotted together for a better analysis.

The GPS daily solution of North, East and Up coordinates is converted into Envisat satellite line of site (LOS) using a Matlab code developed in this thesis (Appendix B). The rate of DASM GPS repeatability (figure 6-10) modeled linearly along the LOS track 278 is -36 mm/yr and along the LOS of track 028 is -57mm/yr.

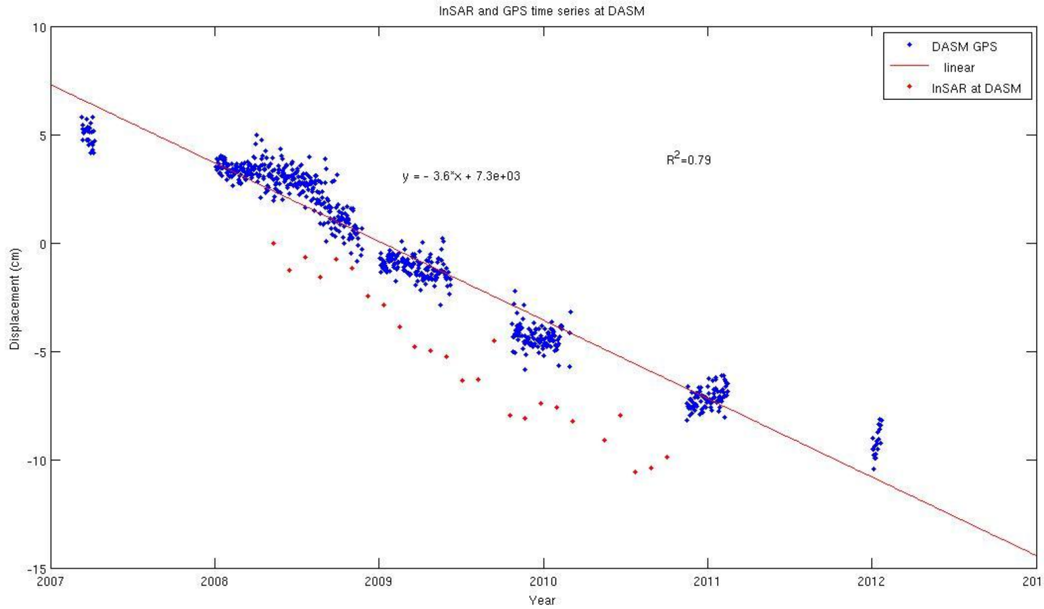

(a)

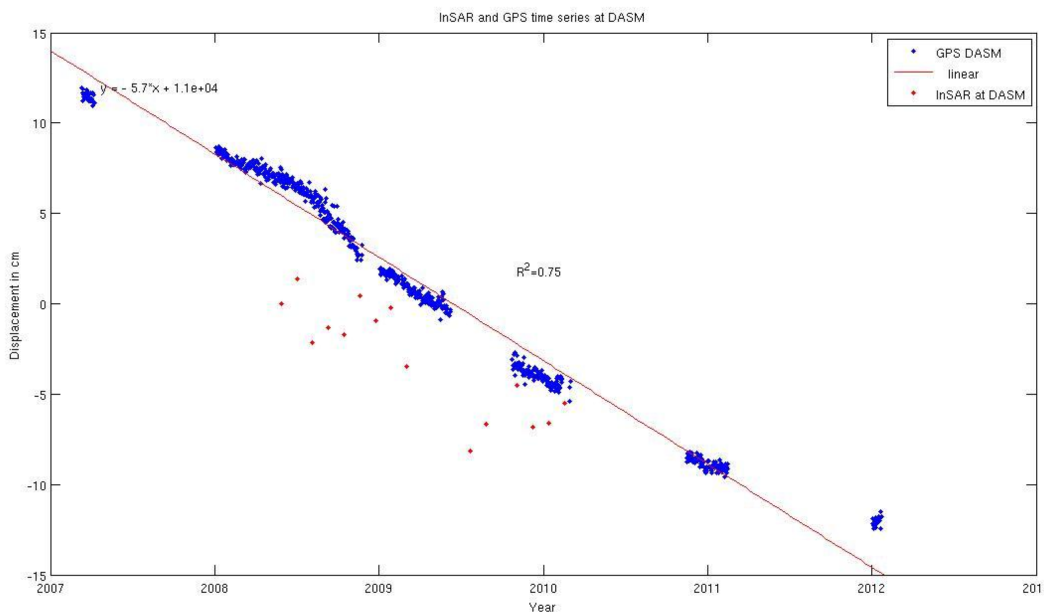

(b)

Figure 6-10 GPS and InSAR LOS displacement at DASM and the linear model (shown by red line) of GPS daily solution (cm). (a) Track 278 and (b) track 028.

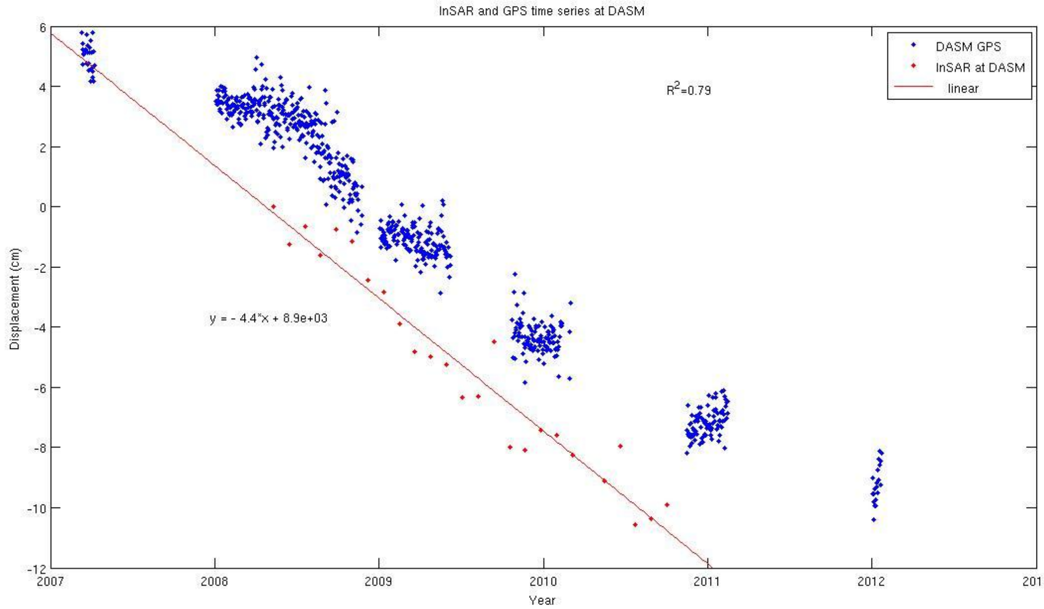

(a)

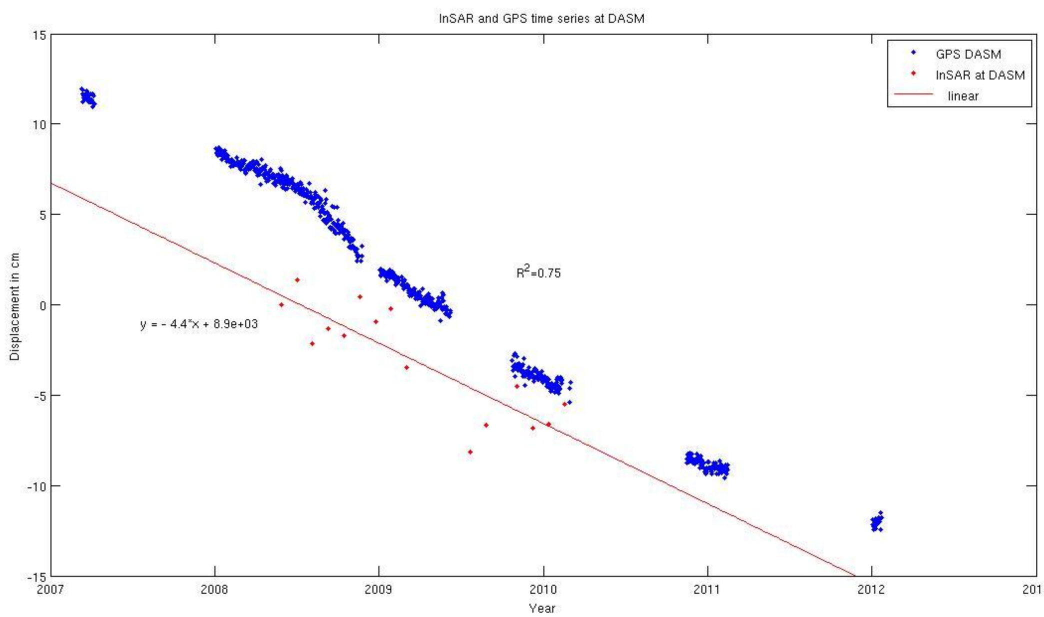

(b)

Figure 6-11 GPS and InSAR LOS displacement at DASM and the linear model (shown by red line) of InSAR time series (cm). (a) Track 278 and (b) track 028.

The InSAR time series at DASM (figure 6-11) shows that there is 44 mm/yr subsidence for both tracks along LOS. The negative slope (rate) shows that the deformation is subsidence. The correlation (R^2) between the GPS time series and InSAR time series is 0.79 and 0.75 in track 278 and track 028 respectively.

The linear fit model shows that -36 mm/yr of velocity of GPS measurement along LOS of track 278(descending track) and -44mm/yr of velocity of InSAR at DASM. The InSAR time-series is faster than the GPS time-series with a difference of 8mm/yr. The correlation coefficient is 0.79 which is well correlated. Comparison of track 028(ascending track) with DASM GPS time-series, the linear model showed that -57mm/yr of velocity of GPS measurement and -44mm/yr of velocity of InSAR at DASM. GPS LOS velocity is faster than the InSAR time-series with a difference of 13mm/yr. The correlation coefficient is 0.75 which is well correlated too.

6.4. Over all Discussion

The results and discussion so far elaborated the numerical figures which come out of InSAR and GPS processing. Indeed, there is a subsidence in the North East of Semera, in Central Afar. What causes this subsidence and if it is an isolated subsidence or a subsidence related to the event since 2005 in the AVC is a work for further research. However, from the existing evidence that one deflate while the other one is inflating is a good indication that the two systems though far apart are well connected. However, due to the short period of investigation this cannot be concluded with certainty.

As it is mentioned in chapter one, the study area is in between the MHR to North West and the Tendaho Rift to the south. The area is covered by stratoid basalt and some area covered by sedimentary rock. The source of these is likely as a result of the Afar plume (Barrat, et al., 2003). In Addition, isotopic ratios have shown that Tertiary and Quaternary basalts have a similar mantle source (Barrat, et al., 2003). The younger volcanic and lacustrine deposits have been estimated of 1.6km based on drilled data in southern section of TG (Aquater, 1996). The sediments is trapped by recent volcanic deposit from volcanic in the basin for instance Kurub volcanic hill. Previous studies made to investigate the subsurface one by Aquater 1996, which is based on surface geologic information and the other one based on gravity and magnetic model (Bridges, et al., 2012), locate the area as a center of a divergent boundary.

Bridges et. al., 2012 work specially showed that the area is located on a center of a divergent boundary where the central part is dominated by a negative total-field magnetic anomaly flanked by positive total-field anomalies

These studies clearly indicated that the area is an active area and it is lying at the center of divergence where symmetric magnetic properties are observed. The result form both GPS and InSAR also agree with previous studies that indicate the area is active.

Chapter Seven

7. Conclusion and Recommendation

7.1 Conclusion

In this study, a deformation at the northeastern part of Semera town is identified using the two satellite geodetic methods. Both the GPS and InSAR measurement showed that there is subsidence in the area. The comparison also shows that the results of the methods are well correlated. However, since the InSAR measurement is 1D, which is along the satellite line of site, the time-series measurement is less sensitive for one dimensional deformation. The three dimensional GPS measurement on the contrary clearly shows that a subsidence of -25mm/yr and -29mm/yr at DASM and DASA GPS stations respectively.

The main source of subsidence and inflation in the Northwest of the area (Southern end of the AVC) has been associated with magmatic processes (Wright, et al., 2006). In particular, in the current study is the coincidence of inflation with the same rate to the north of the deflation site is observe and agrees well with previous findings (Wright, et al., 2006).

Since the accuracy of the measurement in this study is within few millimeters, it verifies the existence and nature of the deformation.

The area where the subsidence is inferred include Semera, the capital city of the Regional State of Afar and near by towns such as Logia and Dubti. On top of these, the area is within the 'Triple Junction' of the diverging plates and a subsidence of this extent is a source of geohazard. The nearby towns are also homes for large population and capital intensive infrastructures which are under construction. Therefore, attention should be given to what is happening to the area in order to mitigate geohazards. This study should serve as an indicator for the need for future work on the deformation in the region.

7.2 Recommendation

In this study, 1D deformation from InSAR is addressed which is less sensitive to real change in the study area. In order to compare the InSAR result with the GPS result, there should be a mechanism to change LOS displacement into 3D displacement so that comparison with the GPS measurement will be better.

The scarcity of GPS stations in the area makes the interpretation less sensitive. To understand the deformation better, more GPS receivers (at least 3 and more) should be installed in the area. As far as InSAR data is concerned, more tracks of Envisat and if possible other satellites data might be processed to get longer time span.

The time span of the data should be increased in order to understand the mechanism of uplift and subsidence.

In Addition to Space geodetic methods, geophysical methods such as Magneto Telluric (MT) and Electrical Resistivity survey could be carried out to ascertain the involvement of magma in the process of uplift and subsidence.

Reference

Abbate, E., Passerini, P., & Zan, L. (1995). Strike-slip faults in a rift area: A transect in the Afar Triangle,East Africa. *Tectonophysics*, 67-97.

Acocella, V., Abebe, B., Korme, T., & and F., B. (2008). Structure of Tendaho Graben and Manda Hararo Rift: Implications for the evolution of the southern Red Sea propagator in Central Afar. *Tectonics, 27, TC4016*(doi:10.1029/2007TC002236).

Acton, G. D., Tessema, A., Jackson, M., & Bilham, R. (2000). The tectonic and geomagnetic significance of paleomagnetic observations from volcanic rocks from central Afar, Africa. *Earth and Planetary Science letter*.

Alessandro, F., Andrea, M.-G., Claudio, P., & Rocca, F. (2007). InSAR Principles: Guidelines for SAR Interferometry Processing and Interpretation. In *TM 19 A,B,C.* ESA.

Aquater. (1996). *Tendaho Geothermal Project -final report.* Aquater.

Ayele, A., Jacques, E., Kassim, M., Kidan, T. O., Chabalier, J. d., & and King, G. (2007). The volcano-seismic crisis in Afar, Ethiopia, starting September 2005. *Earth Planet. Sci. Lett. 255(1-2)*, 177-187.

Barrat, J., Joron, J., Taylor, R., Fourcade, S., Nesbitt, R., & and Jahn, B. (2003). Geochemistry of basalts form Manda Hararo, Ethiopia: LREE-depleted basalts in Central Afar. *Lithos. V. 69*, 1-13.

Battistelli, A., Yiheyis, A., Calore, C., Ferragina, C., & Abatneh, W. (2002). Reservoir engineering assessment of Dubti geothermal field, Northern Tendaho Rift,Ethiopia. *Geothermics*.

Berardino, P., Fornaro, G., Lanari, R., & Sansosti, F. (2002). A new algorithm for surface deformation monitoring based on small baseline differential SAR Interferograms.

Beyene, A., & Abdelsalam, M. (2005). Tectonics of the Afar Depression: A review and synthesis. *J.African Earth Sci.*

Biggs, J. (2007). *InSAR Observations of the Earthquake Cycle on the Denali Fault, Alaska, Ph.D. thesis,*. Department of Earth Sciences, University of Oxford.

Biggs, J., Tim, W., Zhong, L., & Barry, P. (2007). Multi-interferogram method for measuring interseismic deformation:Denali Fault, Alaska. *Geophys. J. Int. (2007)*, 170, 1165–1179.

Bridges, D. L., Mickus, K., Gao, S. S., Abdelsalam, M. G., & AberaAlemu. (2012). Magnetic stripes of a transitional continental rift in Afar. *Geological Society of America*.

Chen, C., & Zebker, H. (2000). Network approaches to two-dimensional phase unwarpping: intractability and atow new alogorithms.

d'Acremont, E. e. (2005). Structure and evolution of the eastern Gulf of Aden conjugate margins from seismic reflection data. *Geophysics Journal International*, 160, 869-890.

Dzurisin, D., & Lu, Z. (2007). Interferometric synthetic-aperture radar(InSAR). In D. Dzurisin, *Volcano Deformation Geodetic monitering Techniques* (p. 154).

ESA. (2012). Retrieved November 20, 2012, from http://www.esa.int: http://www.esa.int/esaCP/SEM1SXSWT1H_index_0.html

Fernandes, R. (2004). Angular velocities of Nubia and Somalia from continuous GPS data: implications on presentday relative kinematics. *Earth Planet., Sci. Lett. 222*, 197-208.

Ferretti, A., Prati, C., & Rocca, a. F. (1999). Multibaseline InSAR DEM Reconstruction: the Wavelet Approach. *IEEE Trans. Geosci. Remote Sensing, vol. 37, no. 2*, pp. 705-715.

G. Blewitt. (2007). GPS and Space-Based Geodetic Methods. In *Treates on Geophysics* (Vol. III, pp. 351-390).

Goldstein, R., & Werner, C. L. (1998). Radar interferogram filtering for geophysical applications. *Geophyisics Research Letters*.

Goldstein, R., Zebker, H., & Werner, C. (1988). Satellite radar interferometry: Two dimensional phase unwrapping.

Guochang Xu. (2007). *GPS - Theory, Algorithms and Applications.* Berlin.

Hamling, I. J. (2010). *Measuring and modelling deformation during the Dabbahu (Afar) rifting episode(Phd thesis).* University of Leeds.

Herring, T. A., King, R. W., & McClusky, S. C. (2010). GPS Analysis at MIT, GAMIT/GLOBK Manual.

Herring, T. A., King, R. W., & McClusky, S. C. (2010). *Introduction to GAMIT/GLOBK, Release 10.4.*

Hofmann-Wellenhof, B., Herbert, L., & Elmar, W. (2008). *GNSS – Global Navigation Satellite Systems GPS, GLONASS, Galileo,and more.* Austria.

INTERMAP. (2007, February). InSAR Newsletter, No.2.

Kearey, P., Klepeis, K. A., & Vine, F. J. (2009). In *Global Tectonics, 3rd Edition* (pp. 101-150).

Kidane, T. C.-Y., & Gallet, y. H. (2003). New paleomagnetic and geochronologic results from Ethiopain Afar: Block rotations linked to rift overlap and propagation and determination of a ~2 Ma referece pole for stable Africa. *J. of Geophysics reserach*.

Lazarov, A. D. (2010). In *InSAR Geometry and Basic Operation.*

M. Hern´andez-Pajares, J. J. (2008). *GPS data processing: code and phase Algorithms, Techniques and Recipes.* Barcelona, Spain.

NASA-Earthmap. (2013). Retrieved January 21, 2013, from http://visibleearth.nasa.gov.

Parkinson, B. W. (1996). *Global Positioning System: Theory and Applications,Vol.I,II, American Institute of Aeronautics and Astronautics, Progress in Astronautics and Aeronautics, Vol. 16.*

Raney, R. (1971). Synthetic aperture imaging radar and moving targets. *IEEE Transactions on Aerospace and Electronics Systems AE S-7*, 499-505.

Reigber, A., Erten, E., Guillaso, E., & O., H. (2007). A free and easy-to-use software tool for DInSAR analysis. *ENVISAT Symposium*, (pp. 23-27). Montreux, Switzerland.

Rosen, P. A. (2000). Synthetic Aperture Radar Interferometry. *Porceedings of the IEEE, Vol. 88,No. 3.* IEEE.

Rosen, P., Hensley, S., Peltzer, G., & Simons, M. (2004). *Updated Repeat Orbit.*

Rowland, J. V., Baker, E., Ebinger, C. J., Keir, D., Kidane, T., Biggs, J., et al. (2007). Fault growth at a nascent slow-spreading ridge: 2005 Dabbahu rifting episode, Afar. *Geophysical Journal International*.

Scharoo, R., & Visser, P. (1998). Precise orbit determinatino and gravity field improvement for the ERS satellites. *J. Geophys. Res.*, 103, 8113–8127.

Schmidt, D. A., & Burgmann, R. (2003). Time-dependent land uplift and subsidence in the SAnta Clara Valley, California, from a large interferogmetric, Synthetic aperture radar dataset.

Seeber, G. (2003). *Satellite Geodesy.* Berlin.

Simons, M., & Rosen, P. (2007). InSAR. In *Treates in Geophysics* (Vol. 3, pp. 391-446). Pasadena, CA, USA: California Institure of Technology.

topex.ucsd.edu. (n.d.). *http://topex.ucsd.edu/gmtsar/demgen*. Retrieved September 25, 2012

unavco.org. (n.d.). *http://sps.unavco.org/crustal_motion/dxdt/model/.* Retrieved November 12, 2012

Wang, H., Biggs, J., & Wright, T. J. (2012). *Poly-Interferogram Rate And Time-series Estimator(V3.1).*

Werner, C., Wegmuller, U., Strozzi, T., & and Weismann. (2000). A. Gamma SAR and interferometric processing software. *ERS - ENVISAT Symposium.*

Wolfenden. (2005). Evaluation of a volcanic rifted margin: southern Red Sea, Ethiopia. *Bulletin geological Society of America*, 117,846-864.

Wright, T., Ebinger, C., Biggs, J., Ayele, A., Yirgu, G., Keir, D., et al. (2006). Magma-maintained rift segmentation at continental rupture in the 2005 Afar dyking episode. *Nature 442*, 291-194.

www.doris.tudelft.nl. (n.d.). *www.doris.tudelft.nl*. Retrieved November 27, 2012

www.treuropa.com. (2012). *http://www.treuropa.com*. Retrieved November 25, 2012, from http://www.treuropa.com/Home/Technique/SARImagery/tabid/409/Default.aspx

Zebker, H. R. (1994). On the derivation of coseismic displacement fields using differential radar interferometry: The Landers earthquake. *J. Geophys.Res.*

Ziebart, M., Adhya, S., Sibthorpe, A., Edwards, S., & Cross, &. (2005). Combined radiation pressure and thermal modelling of complex satellites: Algorithms and on-orbit tests. *Advances in Space Research*.

Appendix A

Interferograms track 278

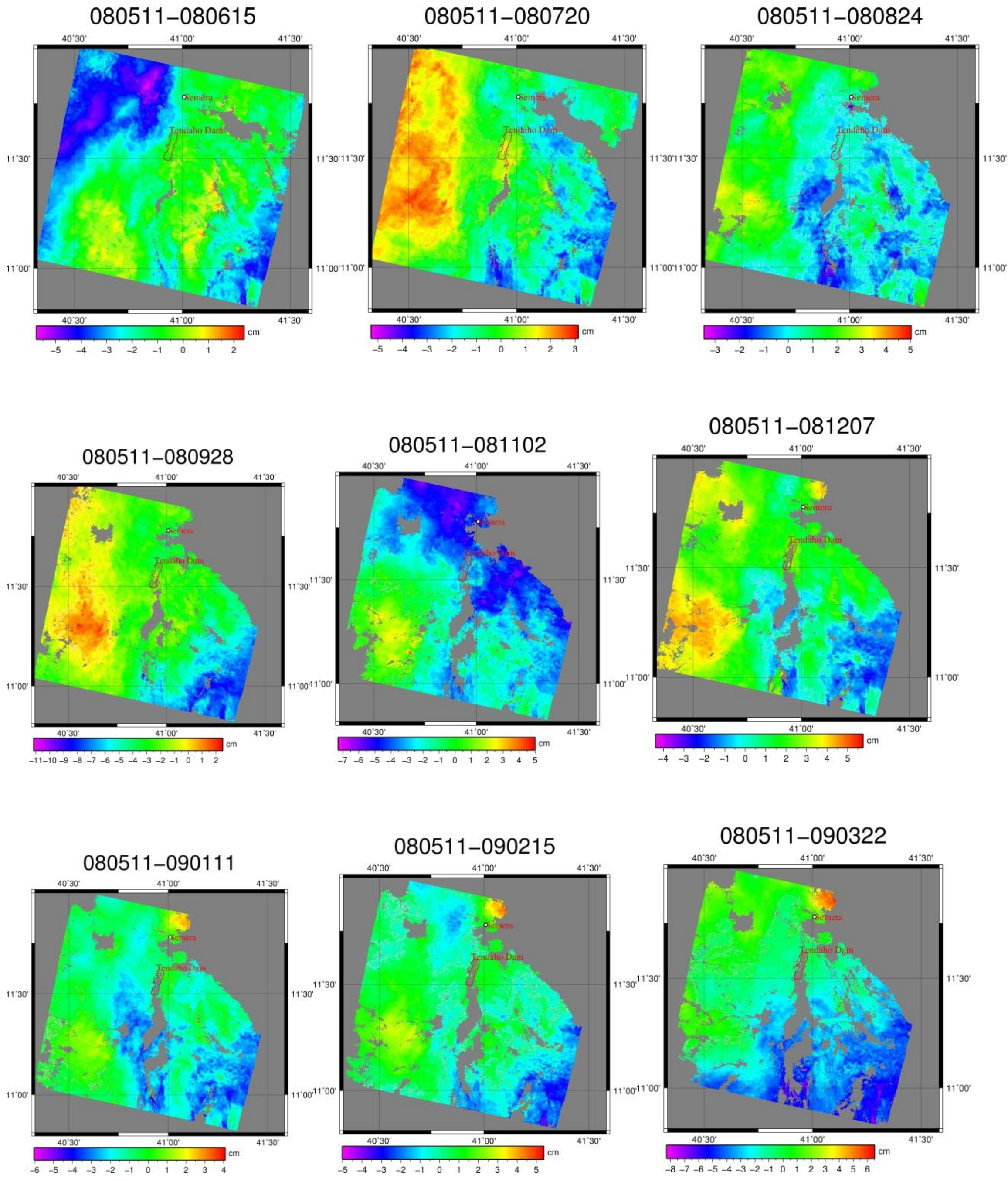

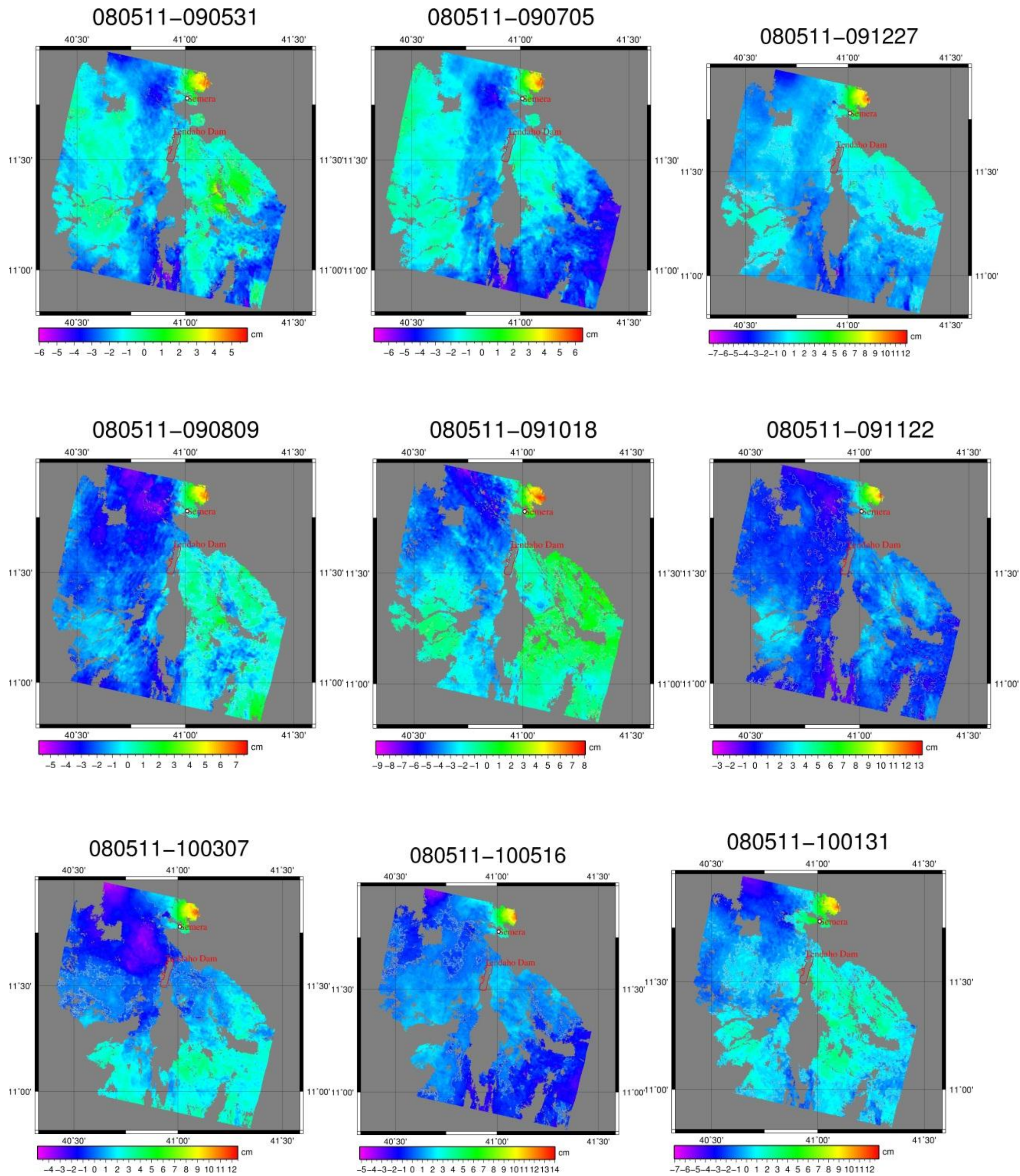
080511−090531
080511−090705
080511−091227
080511−090809
080511−091018
080511−091122
080511−100307
080511−100516
080511−100131
40°30'
41°00'
41°30'
11°30'
11°00'
Semera
Tendaho Dam
cm

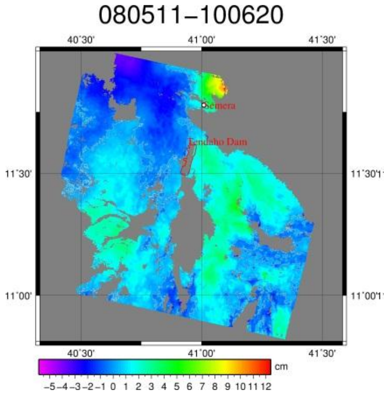
080511−100620
40˚30'
41˚00'
41˚30'
11˚30'
11˚00'
Semera
Lendabo Dam
cm
−5 −4 −3 −2 −1 0 1 2 3 4 5 6 7 8 9 10 11 12

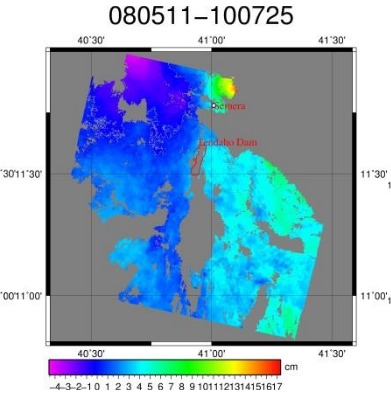
080511−100725
40˚30'
41˚00'
41˚30'
11˚30'
11˚00'
Semera
Lendabo Dam
cm
−4 −3 −2 −1 0 1 2 3 4 5 6 7 8 9 10 11 12 13 14 15 16 17

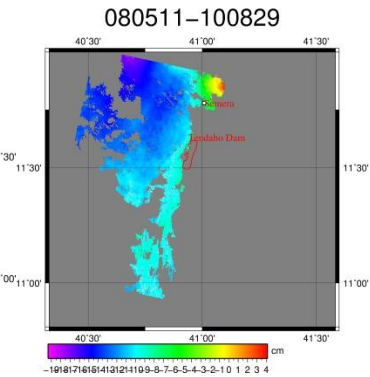
080511−100829
40˚30'
41˚00'
41˚30'
11˚30'
11˚00'
Semera
Lendabo Dam
cm

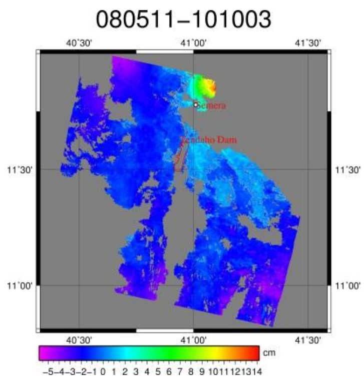
080511−101003
40˚30'
41˚00'
41˚30'
11˚30'
11˚00'
Semera
Lendabo Dam
cm
−5 −4 −3 −2 −1 0 1 2 3 4 5 6 7 8 9 10 11 12 13 14

Track 028

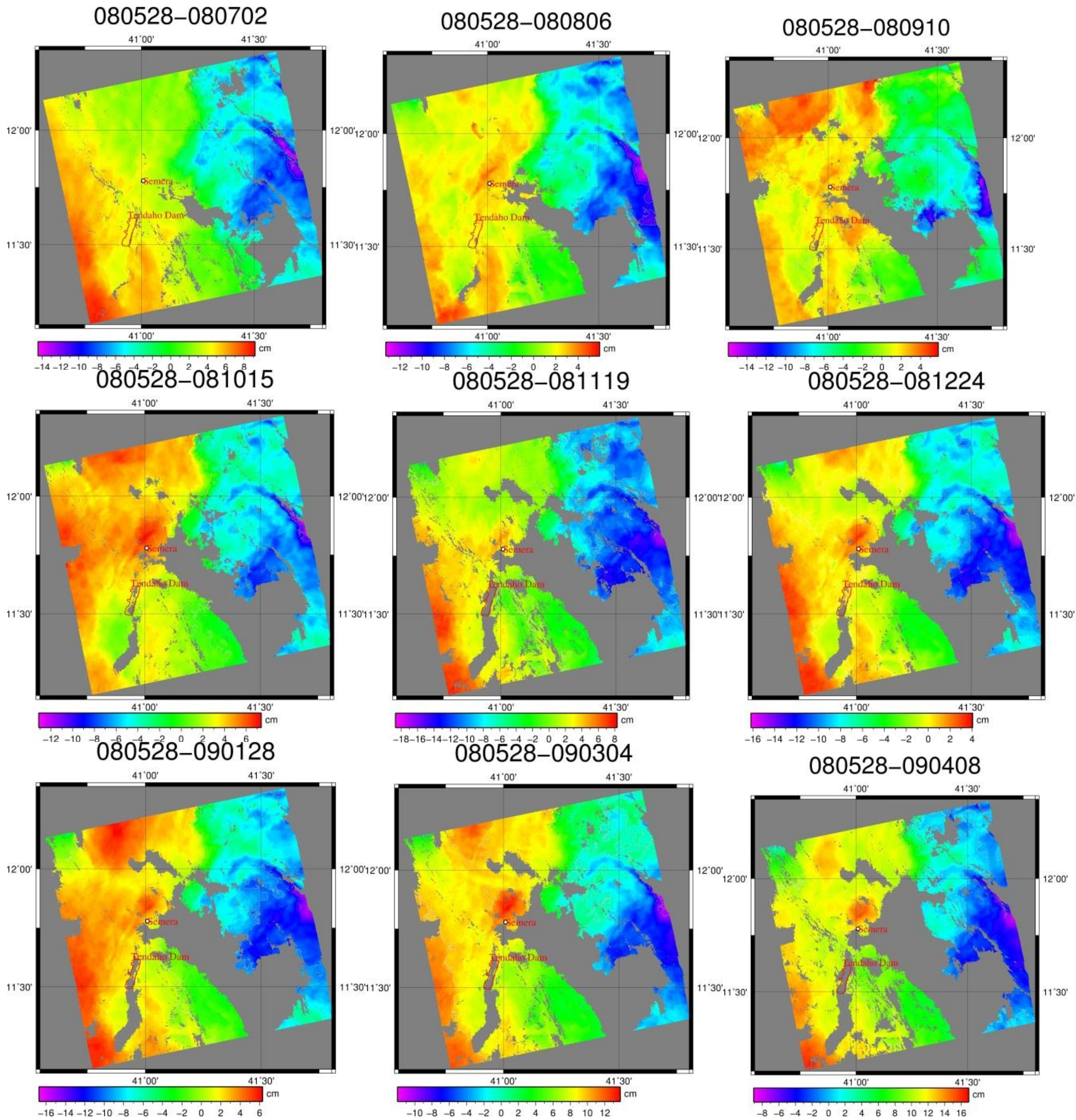
080528–080702
080528–080806
080528–080910
080528–081015
080528–081119
080528–081224
080528–090128
080528–090304
080528–090408
41˚00'
41˚30'
12˚00'
11˚30'
Semera
Tendaho Dam
cm

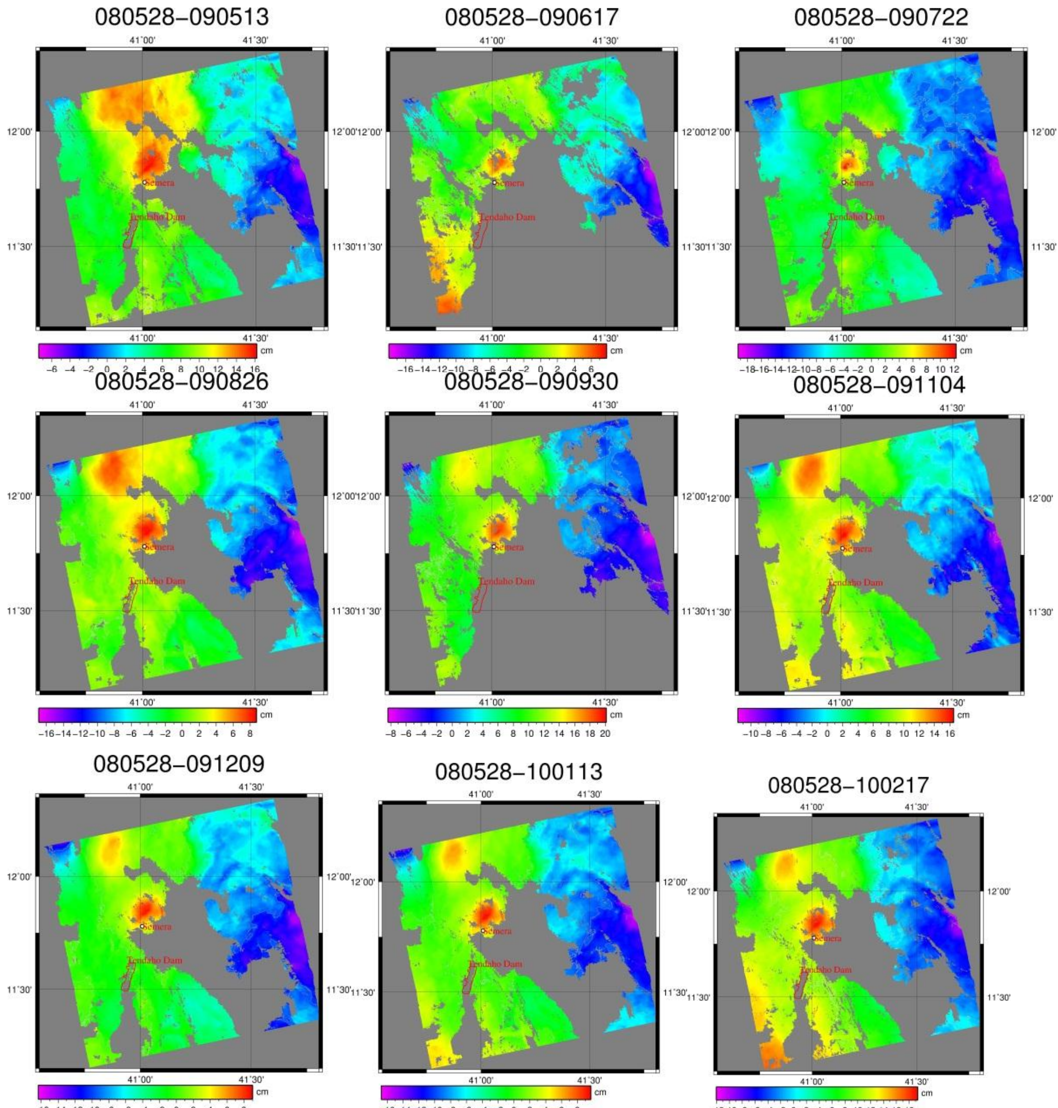
080528−090513
080528−090617
080528−090722
080528−090826
080528−090930
080528−091104
080528−091209
080528−100113
080528−100217
41˚00'
41˚30'
12˚00'
11˚30'
Semera
Tendaho Dam
cm

Appendix B

Matlab code to change the GPS daily solution in to InSAR line of site. The much of the codes are refered from Tim Wright's scripts to model different earthquake sources.

```
%% Set Heading and Incidence Angle for Satellite for tr28 heading is
%% +77.6 for Ascending track and -77.6 for Descending track
Heading = 77.6;     % Heading (azimuth) of satellite measured clockwise from North, in degrees
Incidence =23;      % Incidence angle of satellite in degrees
   %% Calculate LOS_vector from Heading and Incidence
DEG2RAD = pi/180;
%for Desending track
%sat_inc = 90 - Incidence; %for descending
%sat_az  = 360 - Heading;   %for descending
% for Ascending track
sat_inc=Incidence;
sat_az=Heading;
los_x=-cos(sat_az*DEG2RAD)*cos(sat_inc*DEG2RAD);
los_y=-sin(sat_az*DEG2RAD)*cos(sat_inc*DEG2RAD);
los_z=sin(sat_inc*DEG2RAD);
LOS_vector = [los_x los_y los_z];  %Unit vector in satellite line of site
x=load ('/scratch/comp_all/Insarproc/Timesries_JB/gps_new/DASA.E');
y=load ('/scratch/comp_all/Insarproc/Timesries_JB/gps_new/DASA.N');
z=load ('/scratch/comp_all/Insarproc/Timesries_JB/gps_new/DASA.U');
gps = [x(:,2)/10 y(:,2)/10 z(:,2)/10];
%v1=[x(:,1) x(:,2) x(:,3)]
datet = x(:,1);
i=0;

for i=1:length(x)
```

```
    gpslos = LOS_vector*gps'; % LOS calculation

end
figure
%plot(x(:,1),gpslos(1,:),'b.',x(:,1),x(:,2),'ro',y(:,1),y(:,2),'yo',z(:,1),z(:,2),'go')
plot(datet,gpslos(1,:),'b.')
ylim([-10 4]);
 %datetick 'x'
%hold on
%ins= load('dasmins278');
%plot(ins(:,1),-ins(:,2),'r.');
```

Appendix C

```
% program to load the data in to matlab and calcualte the time
% span of the inteferograms and the total duration of the
% available data
close all; clear all;

%opt.origin=roi_pac;

%%%%%%% DIMENSIONS / COORDINATES OF IMAGE TO IMPORT
%%%%%%%
%xmin=40.0008333330000;xmax=42.0008325330000;
%ymin=10.9991674670000;ymax=12.9991666670000;

%xmin = 40.9; xmax = 41.05;
%ymin = 11.3; ymax = 11.7;
```

```
xmin = 40.40; xmax = 41.40;
ymin = 11.40; ymax =12.40;

opt.subset.lalo                    =[ymax xmin; ymin xmax]



%%%%%%% LOAD DATA %%%%%
nigrams=17;
filenames(1,:)='/media/Data/track_028/obs/geo_080109-080213.unw';
filenames(2,:)='/media/Data/track_028/obs/geo_080109-080423.unw';
filenames(3,:)='/media/Data/track_028/obs/geo_080109-080528.unw';
filenames(4,:)='/media/Data/track_028/obs/geo_080109-080702.unw';
filenames(5,:)='/media/Data/track_028/obs/geo_080109-080806.unw';
%filenames(6,:)='/media/Data/track_028/obs/geo_080109-080910.unw';
filenames(7,:)='/media/Data/track_028/obs/geo_080109-081015.unw';
%filenames(8,:)='/media/Data/track_028/obs/geo_080109-081119.unw';
filenames(9,:)='/media/Data/track_028/obs/geo_080109-081224.unw';
filenames(10,:)='/media/Data/track_028/obs/geo_080109-090128.unw';
filenames(11,:)='/media/Data/track_028/obs/geo_080109-090304.unw';
%filenames(12,:)='/media/Data/track_028/obs/geo_080109-090408.unw';
filenames(13,:)='/media/Data/track_028/obs/geo_080109-090513.unw';
%filenames(14,:)='/media/Data/track_028/obs/geo_080109-090617.unw';
filenames(14,:)='/media/Data/track_028/obs/geo_080109-090722.unw';
filenames(15,:)='/media/Data/track_028/obs/geo_080213-080423.unw';
filenames(16,:)='/media/Data/track_028/obs/geo_080423-080528.unw';
filenames(17,:)='/media/Data/track_028/obs/geo_080528-080702.unw';
filenames(6,:)='/media/Data/track_028/obs/geo_080702-080806.unw';
filenames(12,:)='/media/Data/track_028/obs/geo_080806-080910.unw';
filenames(8,:)='/media/Data/track_028/obs/geo_080910-081015.unw';
```

```
for n=1:nigrams
igramtemp=LoadData(filenames(n,:),opt);
igram(:,:,n)=igramtemp.data;
date1(n,:)=igramtemp.date1;
date2(n,:)=igramtemp.date2;

actualdate1=datenum(date1, 'yyyymmdd');
actualdate2=datenum(date2, 'yyyymmdd');
duration=actualdate2-actualdate1;
end
tot=sum(duration) %  the total duration of the inteferograms
totyr=tot/365.14 % the total year  the interferograms taken
```

Appendix D

```
% This Matlab script do traditional stacking
%referece all igrams to the same pixel

for i = 1:size(igram,3)
        %igrams(:,:,i) = igram(:,:,i) - igram(200,300,i);
        igrams(:,:,i) = igram(:,:,i) - igram(400,800,i);
        end

        % add igrams togather
        stac= igrams(:,:,1);

        for j=2:size(igram,3)
        stac=stac+igrams(:,:,j);
```

```
end

% changing radar look to cm
stac_cm= stac*(2.8/2/pi); % wavelength/4*pi
rate= stac_cm/totyr; %convert to rate
rate = rate*10; %mm/yr (same units as pirate)
```

Appendix E

SAR Satellites and their characteristics (INTERMAP, 2007)

Satellite or Mission	Launch Date	Orbit Repeat Cycle	Frequency Band	Polarization	max. Spatial Resolution (single-pol)	Swath Width (for max. Resolution)
ERS-2	21 April 1995	3 days / 35 days	C	VV	20 m	100 km
RADARSAT-1	4 November 1995	24 days	C	HH	9 m	45 km
ENVISAT	1 March 2002	35 days	C	dual-pol	28 m	100 km
ALOS/PALSAR	24 Jan. 2006	46 days	L	quad-pol	10m	40 - 70 km
SAR-Lupe	12 December 2006	< 1 day	X	single-pol	< 1 m in Spotlight mode	8 km
TerraSAR-X	March 2007	11 days	X	dual-pol	3 m (1 m Spotlight)	30 km
RADARSAT-2	March 2007	24 days	C	quad-pol	3 m	20 km
COSMO-SkyMed	May 2007	< 1 day	X	quad-pol	3 m (1 m Spotlight)	40 km
TecSAR	July 2007	36 days	X	quad-pol	3 m	n/a
RISAT	late 2007	19 days	C	dual-pol	3 m	30 km
TanDEM-X	March 2009	11 days	X	dual-pol	3 m	30 km
TerraSAR-L	2008	14 days	L	quad-pol	5 m	70 km
KOMPSAT-5	2009	tbd.	X	tbd.	tbd.	tbd.
MicroSAR	tbd.	tbd.	X	quad-pol	1 m	tbd.
AstroSAR	tbd.	tbd.	X	n/a	3 m	10 km
RADARSAT Constellation	tbd.	12 days	C	HH	5 m	20 km
SENTINEL-1	2011	12 days	C	dual-pol	5 m	80 km
MAPSAR	2011	37 days	L	quad-pol	4 m	20 km - 40 km
SAOCOM	tbd.	16 days	L	quad-pol	10 m	60 km
HJ-1-C	tbd.	2 - 4 days	S	single-pol	5 m	40 km

Appendix F

General plate motions on a global scale. Regional maps show far more complicated motion vectors. Length of arrows indicates rate of movement of that part of the plate. The map is from UNAVCO Plate Motion Calculator

http://sps.unavco.org/crustal_motion/dxdt/model/

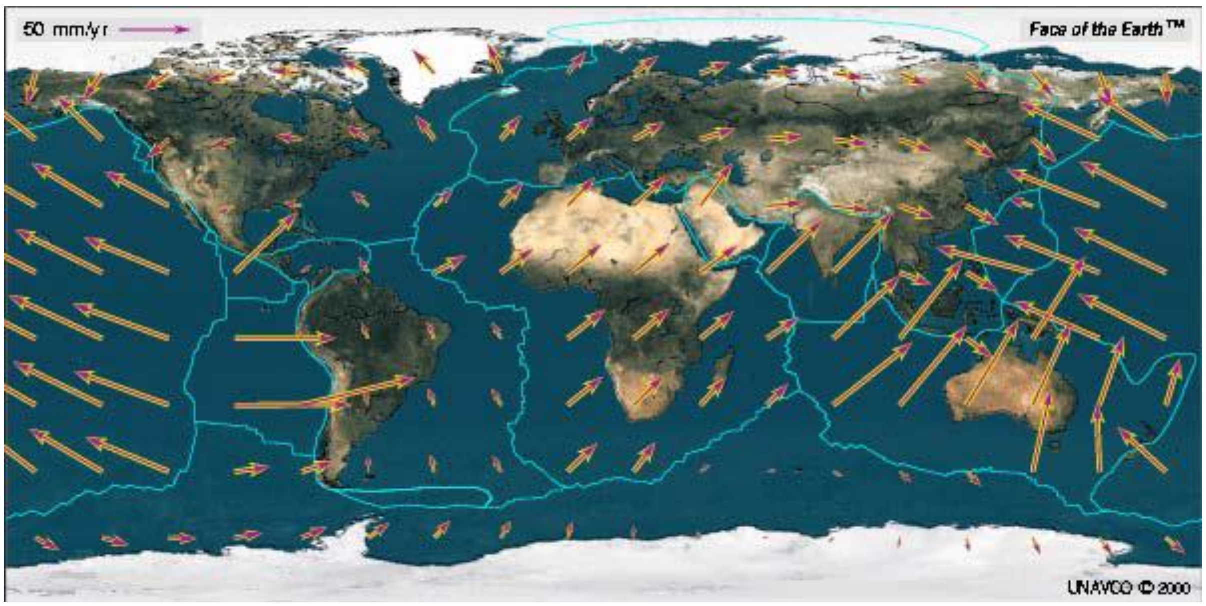

Declaration

This thesis is my original work and has not been presented for a degree in any other university, and that all source of material used for the thesis have been duly acknowledged.

SUBMITTED BY:-

Tesfaye Temtime Tessema ____________________ ________________________

Signature Date

CONFIRMATION:-

Dr.-Ing. Elias Lewi ____________________ ________________________

Advisor Signature Date